Chemical and physical properties of sodium ionic conductors for solid-state batteries

Marie Guin

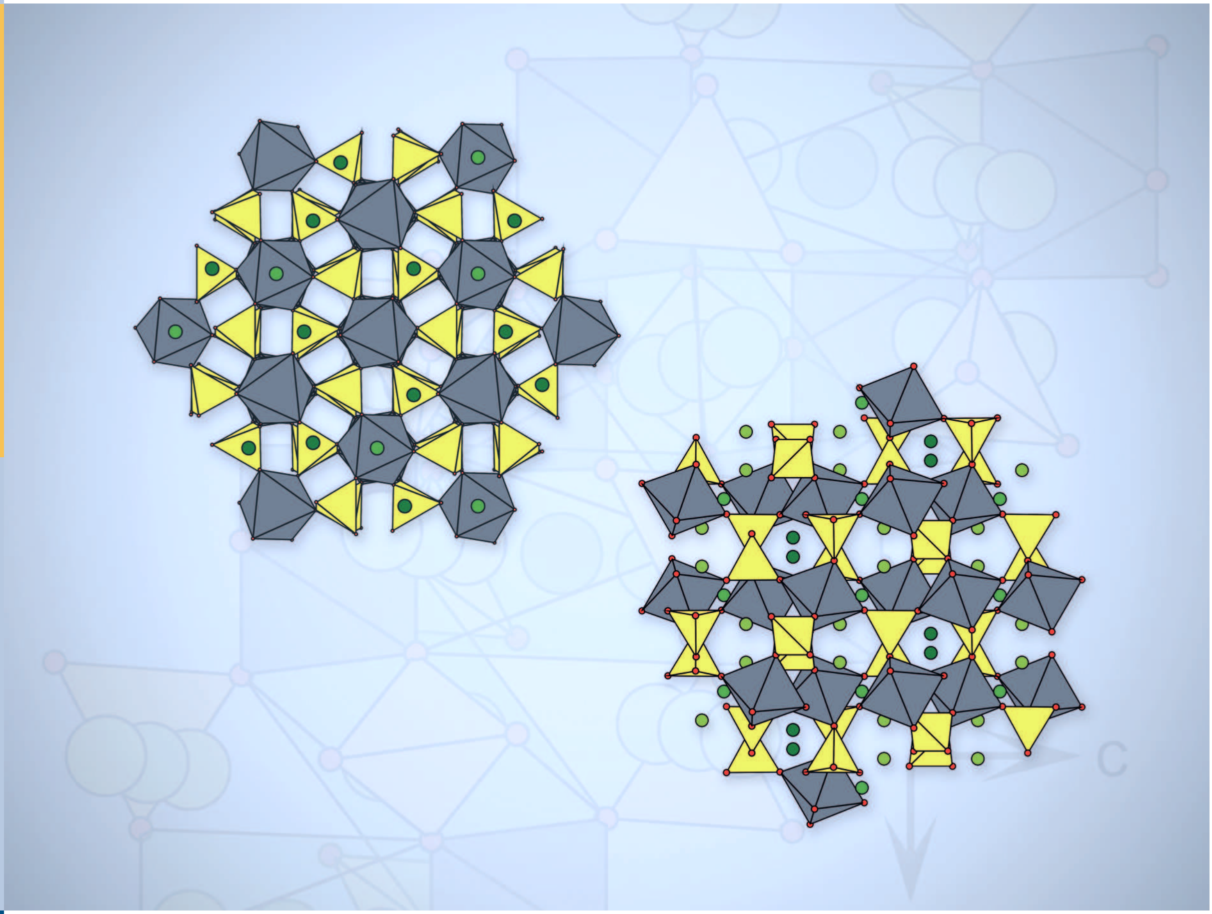

Energie & Umwelt /
Energy & Environment
Band / Volume 373
ISBN 978-3-95806-229-0

JÜLICH
FORSCHUNGSZENTRUM

Energie & Umwelt
Energy & Environment
373
Chemical and physical properties of sodium ionic conductors for solid-state batteries
Marie Guin

Mitglied der Helmholtz-Gemeinschaft

JÜLICH
FORSCHUNGSZENTRUM

Energie & Umwelt /
Energy & Environment
Band / Volume 373
ISBN 978-3-95806-229-0

JÜLICH
FORSCHUNGSZENTRUM

Schriften des Forschungszentrums Jülich
Reihe Energie & Umwelt / Energy & Environment Band / Volume 373

Forschungszentrum Jülich GmbH
Institute of Energy and Climate Research
Materials Synthesis and Processing (IEK-1)

Chemical and physical properties of sodium ionic conductors for solid-state batteries

Marie Guin

Schriften des Forschungszentrums Jülich
Reihe Energie & Umwelt / Energy & Environment Band / Volume 373

ISSN 1866-1793 ISBN 978-3-95806-229-0

Bibliographic information published by the Deutsche Nationalbibliothek.
The Deutsche Nationalbibliothek lists this publication in the Deutsche Nationalbibliografie; detailed bibliographic data are available in the Internet at http://dnb.d-nb.de.

Publisher and Distributor: Forschungszentrum Jülich GmbH
Zentralbibliothek
52425 Jülich
Tel: +49 2461 61-5368
Fax: +49 2461 61-6103
Email: zb-publikation@fz-juelich.de
www.fz-juelich.de/zb

Cover Design: Grafische Medien, Forschungszentrum Jülich GmbH

Printer: Grafische Medien, Forschungszentrum Jülich GmbH

Schriften des Forschungszentrums Jülich
Reihe Energie & Umwelt / Energy & Environment, Band / Volume 373

D 82 (Diss. RWTH Aachen University, 2017)

ISSN 1866-1793
ISBN 978-3-95806-229-0

Abstract

The electrochemical storage of electricity in batteries is one key solution to the future extensive use of renewable energy sources. Lithium ion batteries have received intense attention since they provide the largest energy density and output voltage. They have yet to be optimized in terms of capacity, safety and cost and the search for alternatives to lithium has already gained popularity in the past years because of the shortage of resources. One popular substitute is sodium since its chemical properties are similar to those of lithium and sodium is an abundant element.

Sodium technologies are not new but the commercial sodium-ion batteries operate at temperatures as high as 300 °C raising safety issues and discussion about the energy needed to heat the battery. Therefore, solid-state sodium batteries operating at room temperature present a safer alternative as they are leak proof and non-flammable. In addition, no supplementary heating equipment is needed to operate the battery.

The key in designing safe and efficient solid-state Na-ion batteries is the development of highly conductive solid electrolytes that also display high thermal and chemical stability. Amongst all possibilities, one class of ceramic electrolytes is of great interest: the so-called NASICON materials with general formula $AM(PO_4)_3$ (in this work, A = Na). They display very attractive compositional diversity and are likely to achieve high conductivity.

In this thesis, an extensive study of the composition, the crystal structure and the conductivity of approximately 110 Na-conducting NASICON materials was conducted to find guidelines for designing highly conductive NASICON type materials. For NASICON with aliovalent substitution, the electroneutrality is guaranteed by adapting the amount of Na per formula unit and an optimal Na concentration of 3.2-3.5 mol was identified. Furthermore, an optimal size for the M cations in the structure was highlighted. In addition, the substitution of P with Si proved to have a positive impact on the conductivity.

Using these guidelines, the solid solution $Na_{3+x}Sc_2(SiO_4)_x(PO_4)_{3-x}$ was investigated for the first time. Various compositions with $0 \leq x \leq 0.8$ were prepared by solid state reaction and their crystallographic and electrical properties were investigated. As a result, the high conductivity at room temperature of 8.3×10^{-4} S cm^{-1} was obtained for x = 0.4. In addition, the criteria for high conductivity concluded from the literature study were verified and completed with data of bulk conductivity for the solid solution. This systematic study of the substitution of P with Si provided better insights in the conduction pathway of the sodium ions in the NASICON structure.

Finally, thick, dense pellets of $Na_{3.4}Sc_2Si_{0.4}P_{2.6}O_{12}$ were used as solid electrolyte in different solid-state battery designs and for the first time, a solid-state Na battery based on inorganic materials was cycled at room temperature.

Kurzfassung

Elektrochemische Speicher sind von essenzieller Bedeutung für die zukünftige umfangreiche Nutzung erneuerbarer Energiequellen. Aufgrund ihrer hohen Energiedichte und Zellspannung wurden für diesen Anwendungsbereich bisher in erster Linie Lithium-Ionen-Batterien in Betracht gezogen. Diese müssen jedoch noch in Bezug auf Kapazität, Sicherheit und Kosten optimiert werden. Aufgrund der endlichen Reserven hat zudem die Suche nach Alternativen zu Lithium in den letzten Jahren an Bedeutung gewonnen. Natrium ist der bevorzugte Ersatz, da dieses Element ähnliche chemische Eigenschaften wie Lithium besitzt und auf große natürliche Vorkommen zurückgegriffen werden kann.

Der Einsatz von Natrium in Batterien ist grundsätzlich keine neue Entwicklung. Die bisherigen kommerziellen Natrium-Ionen-Batterien werden aber bei Temperaturen von etwa 300 ℃ betrieben, so dass die Frage nach deren Sicherheit aufkommt. Außerdem wird Energie benötigt, um die Batterie auf diese Temperaturen zu erwärmen. Festkörper-Natrium-Ionen-Batterien, die bei Raumtemperatur betrieben werden, stellen eine sicherere Alternative dar, da sie auslaufsicher und nicht brennbar sind. Darüber hinaus entfällt das Aufheizen auf die Betriebstemperatur, so dass die Festkörperbatterien sofort einsatzfähig sind.

Der wichtigste Aspekt für den Aufbau sicherer und effizienter Festkörper-Natrium-Ionen-Batterien ist die Entwicklung von hoch leitfähigen Festelektrolyten, die sowohl eine gute thermische als auch chemische Stabilität aufweisen. Unter allen Möglichkeiten ist eine Gruppe von keramischen Elektrolyten von großem Interesse: sogenannte NASICON Materialien mit der allgemeinen Formel AM(PO4)3 (in dieser Arbeit, A = Na). Diese zeigen eine sehr attraktive kompositorische Vielfalt und hohe Leitfähigkeiten.

In dieser Arbeit wurde eine umfassende Literaturstudie bezüglich der Zusammensetzung, der Kristallstruktur und der Leitfähigkeit von etwa 110 natriumleitenden NASICON Materialien durchgeführt. Hieraus konnten Richtlinien für die Entwicklung von NASICON Materialien mit hoher Leitfähigkeit abgeleitet werden. Bei NASICON mit aliovalenter Substitution wird die Elektroneutralität durch die Anpassung der Menge an Natrium pro Formeleinheit gewährleistet und für eine hohe Leitfähigkeit wurde eine optimale Natrium-Konzentration von 3,2-3,5 mol ermittelt. Parallel dazu wurde eine optimale Größe für die M-Kationen in der Struktur identifiziert. Darüber hinaus zeigte die Substitution von P durch Si eine positive Auswirkung auf die Leitfähigkeit.

Unter Anwendung dieser Richtlinien wurde $Na_{3+x}Sc_2(SiO_4)_x(PO_4)_{3-x}$ zum ersten Mal untersucht. Verschiedene Zusammensetzungen mit $0 \le x \le 0{,}8$ wurden durch Festkörperreaktion hergestellt und ihre kristallographischen und elektrischen Eigenschaften analysiert. Für x = 0,4 ergab sich hierbei eine maximale Leitfähigkeit von 8,3 x 10-4 S cm-1 bei Raumtemperatur. Darüber hinaus wurden die in der Literaturstudie herausgearbeiteten Kriterien für eine hohe Leitfähigkeit überprüft und mit Daten der Kornleitfähigkeit ergänzt. Diese systematische Untersuchung der Substitution von P durch Si vermittelte einen tieferen Einblick in den Leitungspfad der Natriumionen in der NASICON Struktur.

Abschließend wurden dichte Pellets von Na3.4Sc2Si0.4P2.6O12 als Festkörperelektrolyt in verschiedenen Festkörperbatterie-Designs eingesetzt und zum ersten Mal erfolgte die Zyklierung einer Festkörper-Natrium-Ionen-Batterie basierend auf anorganischen Materialien bei Raumtemperatur.

Table of content

List of Abbreviations

BSD	Back Scattering Detector
BSE	Back-Scattered Electrons
CTE	Coefficient of Thermal Expansion
CV	Cyclic Voltammetry or Cyclic Voltammogram
DFT	Density Functional Theory
DTA	Differential Thermal Analysis
DSC	Differential Scanning Calorimetry
EDX	Energy-dispersive X-ray spectroscopy
GIXD	Grazing Incident X-Ray Diffraction
HSE	Hybrid Solid Electrolyte
ICP-MS	Inductively Coupled Plasma Mass Spectrometry
ICP-OES	Inductively Coupled Plasma Optical Emission Spectrometry
IEK	Institut für Energie- und Klimaforschung (Institute for Energy and Climate Research)
KIT	Karlsruher Institut für Technologie (Karlsruhe Institute of Technology)
MAS-NMR	Magic Angle Spinning Nuclear Magnetic Resonance
MS	Mass Spectrometry
Na/S Battery	Sodium/Sulphur Battery
NEB	Nudged Elastic Band
OCV	Open Current Voltage
ORNL	Oak Ridge National Laboratory
PCE	Plastic Crystal Electrolyte
PVD	Physical Vapour Deposition
SE	Secondary Electrons
SEI	Solid Electrolyte Interphase
SEM	Scanning Electron Microscopy
S.H.E.	Standard Hydrogen Electrode
TG	Thermogravimetry
TOF	Time Of Flight
WDX	Wavelength-dispersive X-ray spectroscopy
XRD	X-Ray Diffraction
ZEA	Zentralinstitut für Engineering (Central Institute for Engineering)
ZEBRA Battery	Zero Emission Battery Research Activity

1. Introduction

The extensive use of fossil fuels in our society has raised environmental concerns, besides these resources are limited. For these reasons, renewable energy sources have gained interest in the last decades as an attractive alternative. The most popular examples are solar and wind energy because of the potential abundance and availability of the sources. However, both these technologies are intermittent energy sources, the energy supply cannot be delivered regularly and is therefore not adjustable to the demand [1]. New electrical energy storage is therefore fundamental, as it will allow energy to be stored during peak hours and released when it is needed.

Energy storage technologies already exist (pumped hydro storage, superconducting magnetic energy storage or compressed air energy storage) but their costs or their availability make them poor candidates for large scale applications [2]. Other promising systems are still under development like hydrogen storage with fuel cells, thermal energy storage or electrochemical storage with batteries. The latter provides stored chemical energy with the ability to convert it as electrical energy with high efficiency.

Amongst rechargeable batteries, the already commercialised Li-ion cells are very attractive since they give the largest energy density and output voltage. However the concerns of the resource availability of lithium, leading to an increasing of its price made the search for alternative battery technologies an important topic. That is why Na-based compounds have recently made a comeback motivated by the abundance and attractive price of sodium [3]. Of course, sodium is heavier and larger that lithium resulting in lower energy density, but since their intercalation processes are similar and the barriers of diffusion of Na-ions is competitive to the one of Li-ions, it seems reasonable to consider also Na-ion batteries as candidates. In addition, the requirements for a battery to have high capacity, high safety, long lifetime and low cost are addressed differently depending on the application (stationary systems, consumer electronics, electromobility) so that Na-technologies can be imagined for stationary applications where the energy density will not be the most critical parameter [4]. Nevertheless, to compete with Li technologies, commercially viable Na or Na-ion batteries have to be developed, and the search for new and optimized electrodes and electrolyte materials is a key step in this process.

Two types of Na batteries have already been commercialised: the sodium-sulphur (Na/S) and ZEBRA (Zero Emission Battery Research Activity) batteries based on Na/$NiCl_2$. Both cells operate at a temperature near to 300 ℃ so that sodium as negative electrode and the positive electrode in the case of Na/S batteries are molten. In laboratory scales, other Na battery technologies are under development, like sodium/air or sodium-ion batteries [5]. These types of batteries are mostly based on liquid electrolytes [3], which always raises the question of safety. As a matter of fact, liquid-containing batteries are more critical to seal and the leakage of possibly toxic or flammable electrolyte may occur. Batteries with only solid compounds (solid state electrodes and solid state electrolyte) present a safer alternative as they are leak-proof and non-flammable [4].

Solid state electrolytes for Na batteries are not new. β-alumina ($NaAl_{11}O_{17}$) was discovered nearly 80 years ago [6] and is in use commercially as the electrolyte in both Na/S and ZEBRA batteries. Though the high temperature operation improves the sodium conduction through the battery components and reduces the ohmic resistance, problems such as sealing, chemical stability issues of the electrodes and the electrolyte or thermal expansion mismatch of the different components also arise. For these reasons, the development of sodium battery technologies operating at lower temperature is sought after, even if for stationary applications like the back-up storage of renewable energy mentioned before the constraint of operation temperature can be regarded as less demanding than for other applications. That is why a lot of effort is put in developing Na-ion batteries that operate at lower temperatures, i.e. either at room temperature or just above the melting point of sodium (97.7 ℃). To achieve this purpose, amongst different topics of research, the development of other fast sodium-ion conductors than the well-known β-alumina have been investigated recently (manganese oxides [7, 8], layered oxides [9], NASICON materials [10], olivines [11], fluorophosphates [12-14]).

Amongst the possible candidates as solid state electrolytes for Na-ion batteries, the so-called NASICON materials [10] have focused an increasing attention during the recent years. The name NASICON (Na^+ superionic conductor) was used for the first time in 1976 by Hong et al. to describe the high conduction in $Na_3Zr_2Si_2PO_{12}$ [10] but today it is applied to describe all materials with similar crystal structure and the general composition $A_{1+2x+y+z}M^{(II)}_xM^{(III)}_yM^{(IV)}_{2-x-y}Si_zP_{3-z}O_{12}$, where A is usually a mono- or divalent cation (in this work, A = Na) and M are divalent, trivalent, tetravalent or even pentavalent cations; P can also be substituted with Si or As. NASICON materials are very attractive because of their compositional diversity leading to many possible applications, such as electrode materials or solid electrolytes in batteries (as tested in an all-NASICON battery by Lalère et al. [15]), Cl_2 and CO_2 sensors [16, 17], or photoluminescence devices [18]. Their stability and high ionic conductivity makes them attractive candidates as solid electrolytes for solid-state Na-ions batteries [19].

In this work, guidelines for designing highly conductive NASICON type materials were concluded from an extensive literature study [20]. More precisely, the amount of charge carriers per formula unit should be as high as 3 - 3.5 mol and the M cations should have an ionic radius close to the ionic radius of Zr, i.e. r_{Zr} = 0.72 Å [21]. In addition, it was observed that the substitution of P with Si has a positive impact on the conductivity as it was demonstrated by Hong on $Na_{1+x}Zr_2Si_xP_{3-x}O_{12}$ [10] and Vogel et al. on $Na_{1+x}Hf_2Si_xP_{3-x}O_{12}$ [22]. That is why the solid solution $Na_{3+x}Sc_2Si_xP_{3-x}O_{12}$ (abbreviated hereafter as $NSSiP_x$) was investigated.

In this thesis, the above mentioned literature review is first described in details as well as some background information about solid-state Na-ion batteries. The next chapter summarizes the materials and methods used with a special focus on understanding the analysis of the obtained data which are then described in following chapters. The fourth chapter presents the experimental study of the solid solution $NSSiP_x$ highlighting the following topics:

- the analysis of the crystal structure of the members of the solid solution
- the thermal behaviour of the materials
- the conductivity and activation energy for the sodium diffusion

Directly after the presentation of these results, a discussion chapter describes the correlations between crystallographic or compositional data with the conductivity data in order to gather a better understanding of the motion of the Na ions in these materials as well as the reasons for their high or low performance. The sixth chapter describes the use of one of these materials as solid electrolyte in different solid-state battery designs as a proof of concept and the results of the testing of these battery prototypes are discussed. To finish with, a summary and concluding remarks are given.

2. Sodium-ion batteries and related materials

2.1. Sodium over Lithium

Since among all possible energy storage technologies the Li-ion battery provides the largest energy density and output voltage, it has already taken over the portable electronic market and is the most investigated candidate for electromobility applications. One other advantage of Li technologies is the broad range of attractive materials possibly used as electrodes or electrolytes leading to many imaginable designs for Li-based energy storage systems. Nevertheless, Li is a limited resource found in remote or politically sensitive areas, so the increasing use and the upscaling of Li batteries raises concerns about their future price. The search for a cheap and abundant alternative to Li is therefore necessary [3, 5].

One possible candidate to solve these issues of price and scale is Na, an unlimited resource and therefore very cheap as shown in Table 2.1.

Table 2.1: Main characteristics of Na and Li materials [3].

Characteristics	Na	Li
Price (for carbonates)	0.07 - 0.37 € kg^{-1} (Purity 98.8 – 99.2 % min)	4.11 – 4.49 € kg^{-1} (Battery grade 99.9 %)
Specific capacity	1.16 A h g^{-1}	3.86 A h g^{-1}
Voltage vs. S.H.E.	- 2.7 V	- 3.0 V
Ionic radius	0.98 Å	0.69 Å
Melting Point	97.7 ℃	180.5 ℃

Of course, not only the price of Na-salts and Li-salts should be compared but the whole battery components have to be considered. Larcher and Tarascon mentioned a possible cost decrease of approximately 30 % for Na-technology compared to Li-technology because cheaper sodium-based electrolytes can be developed and cupper can be replaced by aluminium as current collector on the anode side. In addition, the use of Co- and Ni-free compounds would allow to lower the price of batteries even more [23]. Furthermore, the recycling of Li metal (as well as Co and Ni) will be compulsory not only to compensate the limited resources but also regarding the environmental impact of Li technologies. This difficult process increases the price of the Li battery over its entire lifetime. On the contrary, Na is easy to recover opening the way toward greener and more sustainable batteries in the future [23].

Since Na and Li have comparable intercalation processes, one can adapt the Li-ion battery knowledge to develop Na-ion batteries but it has to be kept in mind that the Na technologies will always give less energy density than the Li analogues because of the higher weight of Na. However, Na batteries could be developed for different applications than Li batteries, for example the storage of the fluctuating renewable energies and the release of energy into the grid. There, the weight requirements are less demanding [3].

As shown in Table 2.1, Na is not only heavier but also bigger than Li. Therefore, one would expect the motion and intercalation of the Na-ions in battery materials to be more difficult than for Li. On the one hand, this is true considering the intercalation into graphite often used as negative electrode in alkali-ion batteries. As a matter of fact, transfer of the electron from the alkali metals to graphite is easier for lower ionization potential and it increases from 3.893 eV to 5.390 eV from Cs to Li so that the intercalation of Li is the easiest. On the other hand, this assumption is false looking at the ionic motion inside cathode or electrolyte materials. As an example, the ionic conductivity of $Li_{1.5}Al_{0.5}Ti_{1.5}(PO_4)_3$ (LATP) of 1.3×10^{-3} S cm^{-1} [24] and $Na_3Zr_2Si_2PO_{12}$ (NZSiP) of 6.7×10^{-4} S cm^{-1} [10] are comparable. Both values are in the same range for materials having similar crystal structure and conduction paths for Li and Na. These examples prove that it is possible to find very high sodium-conductive materials to be used in Na-ion batteries even if the ionic radius of Na is bigger than that of Li.

The high ionic conductivity of Na in ceramic materials, its abundance and low price as well as its similar intercalation process to Li made the interest for developing Na-based energy storage systems grow in the last years after most of the battery research was focused on Li for two decades. Figure 2.1 shows the amount of publications containing the keyword “Na Battery” compared to the ones containing “Li Battery” from 1976 to 2015. At the very beginning, both technologies were investigated in parallel but starting in the 1990s, the research on Li battery started to grow exponentially while the Na battery research only regained popularity since 5 years.

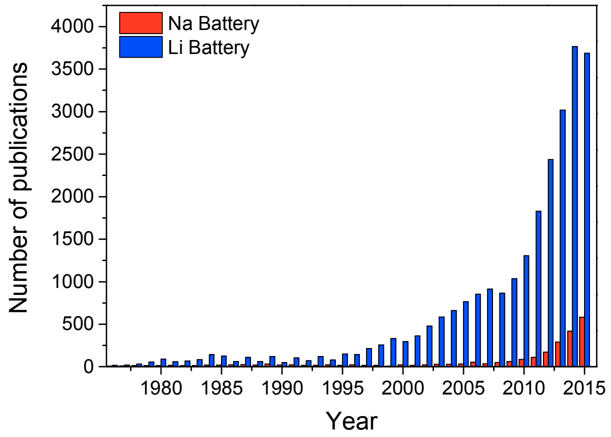

Figure 2.1: Number of publication containing the keyword “Na Battery” compared to “Li Battery” from 1976 to 2015 (source: Scopus).

2.2. Secondary sodium-ion batteries

2.2.1. Composition and operation

A secondary (rechargeable) sodium-ion battery (NIB), as any other battery, consists of a positive and a negative electrode separated by an electrolyte, a pure ionic conductor that can be a liquid, gel or solid. In the case of a liquid electrolyte, a separator membrane keeps physically both electrodes apart and prevents electrical short-circuiting. The sodium ions move from one electrode to the other through the electrolyte as electrons enter the external circuit. Figure 2.2 shows the basic working principle of the NIB with the example of a layered-cathode material and hard carbon anode. The functioning principle of the battery does not change with different cathode or anode materials.

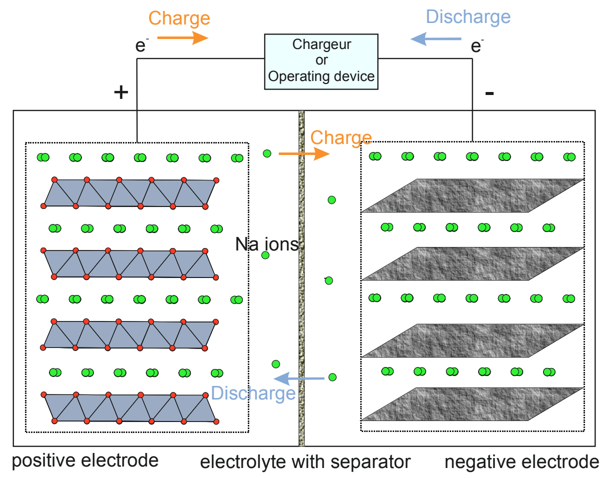

Figure 2.2: Operation principle of a typical sodium-ion battery.

During charging, the sodium ions are intercalated into the anode material whose working potential should ideally be lower than 1.0 V vs Na^+/Na. On discharge, the reversible reaction occurs: the sodium ions are intercalated in the cathode material with a working potential above 3.0 V vs. Na^+/Na and the electrons flow simultaneously out of the external circuit to provide the electrical power. This commuting of Na^+ ions between two electrodes is commonly referred to as rocking chair concept [4]. Different criteria have to be respected for the selection of the electrodes and electrolyte to make the functioning process possible as well as the battery competitive; they are summarized in Table 2.2.

Table 2.2: Summary of the criteria for battery materials [25, 26].

Electrolyte	Cheap, non-toxic, environmental-friendly Ease of fabrication/ compact design Electronic insulator High Na^+-ion conductor Thermodynamically stable in a wide temperature range Compatible with the cathode and anode materials High electrochemical window
Anode	Cheap, non-toxic, environmental-friendly Ease of fabrication/ compact design Highly electropositive High capacity and energy density Intercalation host for Na^+ (rapid intercalation of a lot of Na^+ with low structural/volume changes) Intercalation of Na^+ with low Gibbs-energy Electronic conductor
Cathode	Cheap, non-toxic, environmental-friendly Ease of fabrication/ compact design Contains an element easy to oxidise or reduce High capacity and energy density Intercalation host for Na^+ (rapid intercalation of a lot of Na^+ with low structural/volume changes Intercalation of Na^+ with high Gibbs-energy Electronic conductor Chemically stable High electrochemical window

One important criterion for the anode and the cathode material is the Gibbs-energy of the intercalation process of Na^+ because it is directly related to the voltage of the battery. As a matter of fact, the voltage is related to the work the cell can deliver on transferring electrons in the external circuit and to the free energy change on transferring the Na^+ ions [25, 27, 28]. The open circuit voltage V_{OC} is defined as in Equation 1.

$$V_{OC} = -\frac{\mu_{Na}^{Cat} - \mu_{Na}^{An}}{nF} \qquad \text{(Equation 1)}$$

where *F* is the Faraday constant (96485 C mol^{-1}), *n* is the number of electrons involved during the reaction and μ_{Na}^{Cat} and μ_{Na}^{An} the chemical potentials of Na in the cathode and the anode, respectively.

The chemical potential *μ* is defined by the variation of the free Gibbs-energy *G* with the concentration of the inserted ions *n*:

$$\mu = \frac{\delta G}{\delta n} \qquad \text{(Equation 2)}$$

Equation 1 and Equation 2 can be summarised as the voltage being a measure of the energy of the electrons that are involved in the chemical reactions during the operation of the battery.

Another important quantity to describe the battery is its capacity as it is related to the amount of charge it can store. The unit for the capacity is Ah which is defined as 1 A that is passed for one hour or 3600 C s.

The theoretical capacity of the cell is defined by the Faraday's law:

$$Q_{th} = \frac{1000 \times F \times n}{M \times 3600} \quad (\text{mAh g}^{-1}) \qquad \text{(Equation 3)}$$

where *n* is the number of moles of electrons transferred in the electrochemical reaction, *F* is the Faraday constant and *M* the molecular weight of the active material [27]. In other words, Equation 3 represents a relation between the number of electrons and the number of moles in an electrochemical reaction. With both the voltage and the capacity, one can describe the phenomena happening in the cell during charge and discharge. Other quantities are also used to characterise a battery and they are summarized in Table 2.3, where all the specific quantities per unit mass can also be calculated per unit volume.

Table 2.3: Definition of the basic concepts describing a battery [29].

Concept	Definition
Open circuit voltage	Abbreviation *OCV* or V_{OC} as described in Equation 1
Working voltage	$V = V_{OC} - IR\ (V)$ (Equation 4) where *I* is the working current and *R* the internal resistance of the cell
Specific charge and discharge capacity	Q_c or Q_d is based on the total amount of charge transferred $Q_c(or\ Q_d) = \frac{I \times t}{m}\ (\text{mAh g}^{-1})$ (Equation 5) where *I* is the current, *t* the time and *m* the mass of active material
Specific energy density	SED represents the amount of energy stored per unit mass $SED = V \times Q\ (Wh\ kg^{-1})$ (Equation 6) where *V* is the voltage, *Q* is the specific capacity (here the mass in *Q* is the weight of the cell)
Specific power density	*SPD* is the amount of power per unit mass $SPD = \frac{SED}{t}\ (W\ kg^{-1})$ (Equation 7)
Coulombic efficiency	*η* represents the ratio of the output of charge to the input of charge $\eta = \frac{Q_d}{Q_c} \times 100\ (\%)$ (Equation 8)

2.2.2. Commercially available sodium-ion batteries

Sodium/sulphur batteries were the first commercialised secondary Na batteries. They were attractive candidates because of the low cost of materials, high capacity and environmental friendliness of sulphur. In the typical Na/S cells, the negative electrode is molten sodium contained in a tube of solid electrolyte β’’-alumina, surrounded by molten sulphur as sketched in Figure 2.3 [30]. During the discharge of the cell, sodium ions pass through the β’’-alumina to the cathode, as electrons are discharged to the external circuit. The sodium ions react with sulphur to form polysulfides. The reverse reaction occurs during charging [31].

The cell operates at a temperature of about 300 ℃ to allow both the electrodes to be molten. At this temperature, the liquid compounds of the cell are highly corrosive, the containers and seals must resist these harsh conditions and a lot of research has been devoted to corrosion resistant materials or “low-temperature” sodium sulphur batteries working just below 100 ℃ so that the Na anode still stays molten [5].

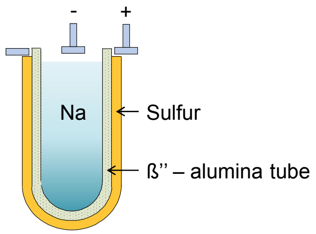

Figure 2.3: Schematic representation of the sodium sulphur cell.

Despite these high operating temperatures, the cell produced by NGK, Japan have been used since 2003 for load-levelling and emergency power applications in 174 locations in 6 countries around the world. Only one accident was reported to date, when a battery fire started in Japan in September 2011, but it was controlled quickly without further damages [5].

A similar type of battery was later commercialised: the sodium/nickel chloride battery or ZEBRA battery [32]. In this battery, the positive electrode consists of metal chloride. The electrolyte is also β’’-alumina but in this case, a liquid electrolyte (NaAlCl ($NaAlCl_4$) is added to the nickel chloride [33] for better interfacial contact and less corrosion. The anode is Na metal and iron is also incorporated to the cell to increase the power response [34-36]. Comparable to the Na/S battery, this cell also operates at a temperature between 270 and 350 ℃ to have molten electrodes. During the discharge, the sodium is oxidised and sodium ions are transported through the solid electrolyte to the $NiCl_2$ by the second electrolyte. There, NaCl and Ni are formed. One advantage of this battery over the Na/S cell is that the cathode is partially solid so that the cell is safer. In the case of the electrolyte failure, the liquid $NaAlCl_4$ reacts with sodium to sodium chloride and aluminium. Small cracks in β’’- alumina can be resealed by the reaction products. In addition, the battery can be assembled in a discharged state with NaCl, Al, Ni and Fe powder and the cell offers a higher voltage [5].

The main characteristics of both types of molten sodium batteries are summarised in Table 2.4. In both cases, the elevated operating temperature is of concern. The safety is an issue especially for the Na/S technology. For both types of batteries, the expensive heating requirements and temperature management difficulties motivate the search for alternative technologies working at low temperature. As an example a patent from the company Ceramatec reported on a molten sodium battery working between 100 and 170 ℃ [37].

At last, another type of Na-ion battery exists commercially; the company Williams Advanced Engineering has reported a pack design containing 48 cells of 3Ah from the company Faradion Limited. The batteries are based on liquid electrolyte using hard carbon anode produced by Faradion

Limited and polyanion cathode (layered oxide or pyrophosphate as it will be described in Chapter 2.2.4) [38]. The corporate website of the company reports as preliminary results similar efficiency and life cycle than Li-ion batteries but a higher safety [39].

Table 2.4: Summary of the main features of the high temperature sodium batteries [40].

Battery	Na/S	ZEBRA
Manufacturer	NGK insulators / TEPCO	FIAMM Sonick
Cell configuration	Na | β''-alumina | S	Na | β''-alumina | MCl_2 (M = Fe, Ni)
Cell OCV	2.08 – 1.78 V	2.58 V
Operating temperature	300 – 350 ℃	270 – 350 ℃
Theoretical capacity	377 Ah kg^{-1}	305 Ah kg^{-1}
Theoretical (practical) specific energy	760 (140 – 240) Wh kg^{-1}	788 (120) Wh kg^{-1}
Specific power	90 – 245 W kg^{-1}	130 – 160 W kg^{-1}
Life cycles	3500 – 5000	3500 – 5000
Efficiency	80 – 90 %	80 – 90 %
Applications	Stationary energy storage	Battery electric vehicles / Stationary energy storage
Advantages	High power High energy density High efficiency of charge / discharge Temperature stability Low-cost of raw materials	High voltage Better tolerance against overcharging Easy assembly Safe
Shortcomings	Preheating to the operation temperature Unsafe High operating temperature Molten sodium electrode Uses 10 – 14 % of its own capacity per day to maintain temperature when not in use	Preheating to the operating temperature High operating temperature Molten sodium electrode Uses 10 – 14 % of its own capacity per day to maintain temperature when not in use
Environmental impact	Only Na hazardous material No emissions during operation	Recovery of Ni No emissions during operation

2.2.3. Solid-state sodium-ion battery

Solid-state sodium-ion batteries present the solution to the safety issues caused by the use of liquid electrolyte or electrodes like in Na/S batteries but to date, no solid-state Na-ion battery exists commercially. Nevertheless, their feasibility has recently been proven on the laboratory scale. In the following, recent studies on solid state batteries using solid electrolytes described further in Chapter 2.2.4 are presented.

Already in 2014, Lalère et al. demonstrated the use of NASICON-type materials in a solid-state battery prepared by spark plasma sintering (SPS) and cycling at 200 ℃ [15]. The symmetric battery was composed of the same anode and cathode: a mixed electrode of the active material $Na_3V_2(PO_4)_3$ and with the solid electrolyte $Na_3Zr_2Si_2PO_{12}$. The co-sintering of both the electrodes and the electrolyte was carried out at 900 ℃. These conditions did not allow the electrolyte to reach a high density. Therefore the cell showed very high internal resistance and could not be operated at room temperature. At the operating temperature of 200 ℃, the battery worked at 1.8 V with 85 % of theoretical capacity.

More recently, several all solid-state batteries were prepared with the different solid electrolytes described in Chapter 2.2.4. Zhu et al. have reported the cycling of an all-organic solid-state battery with polymer electrodes and plastic crystal electrolyte (PCE) [41] with open circuit voltage at 2.4 V and a capacity of 160 mAh g^{-1} corresponding to 80 % of the theoretical capacity. Tanibata et al. used glass-ceramic as electrolyte in a $Na_{15}Sn_4$ | Na_3PS_4 | amorphous TiS_3 cell achieving 300 mAh g^{-1} capacity after 5 cycles [42]. Ni'mah et al. developed a $Na_{2/3}Co_{2/3}Mn_{1/3}$ | PEO-based electrolyte | Na cell demonstrating the suitability of their polymer nanocomposite electrolyte [43] and Kim et al. used an hybrid solid electrolyte (combination of ceramic, polymer and liquid electrolytes) in a flexible sodium battery with $NaFePO_4$ cathode [44].

For solid-state battery technologies, the challenge is to overcome the higher resistance of the cell compared to liquid electrolyte batteries by finding high conductive electrolyte and optimising the design of the cell to achieve a good contact between the electrodes and the electrolyte.

2.2.4. Materials for sodium-ion batteries

During the past 10 years, as NIB have gained popularity, a lot of efforts have been made to find suitable electrodes. Since the intercalation processes of Li^+ and Na^+ are similar, the materials used in Li-ion batteries first inspired the research on Na electrodes by simply replacing the charge carrier, but the size and polarisation differences between both cations make it necessary to look for materials adapted to the Na insertion. Especially the search for suitable anode materials is a major challenge since typical graphite anodes employed in Li batteries do not intercalate Na^+ ions.

Positive electrodes

In order to realise competitive Na-ion batteries, high-performance cathodes are necessary and the potential candidates belong to one of the three following categories:

- Layered sodium transition-metal oxides
- Polyanionic frameworks
- Prussian blue cathodes [32]

The layered cathode materials of the type AMO_2 (A = Na, M = Co, Mn, Fe, Ni) are of interest because of their high redox potential and energy densities. In addition, the compounds with low amount of Co and high amount of Fe and Mn are especially attractive since they are environmentally friendly and less expensive. The Na-based layered materials are divided into two main groups using the classification offered by Delmas et al. [45]: O3 type or P2 type as shown in Figure 2.4 where the O3-type material is $NaMnO_2$ [46] and the P2 type is $Na_{2/3}Mn_{1/2}Fe_{1/2}O_2$ [47].

In both O3- and P2-types, the sodium atoms are six-fold coordinated but they occupy octahedral sites and prismatic sites, respectively (Figure 2.5) giving to the structure its name O for octahedral and P prismatic coordination for the alkali ion. The number 3 and 2 in O3- and P2-type correspond to the number of MO_2 layers in an hexagonal cell [48].

Different substitutions on the M site with Ni, Li or Mg were considered to improve the capacity of the layered cathode material [49-51] and good battery performances as well as stable cycling could already be achieved [32]. Nevertheless, one important drawback of the layered cathode materials is their poor stability and their handling and storage implying working in argon-filled glove boxes could represent an obstacle to an up-scaled use of these materials.

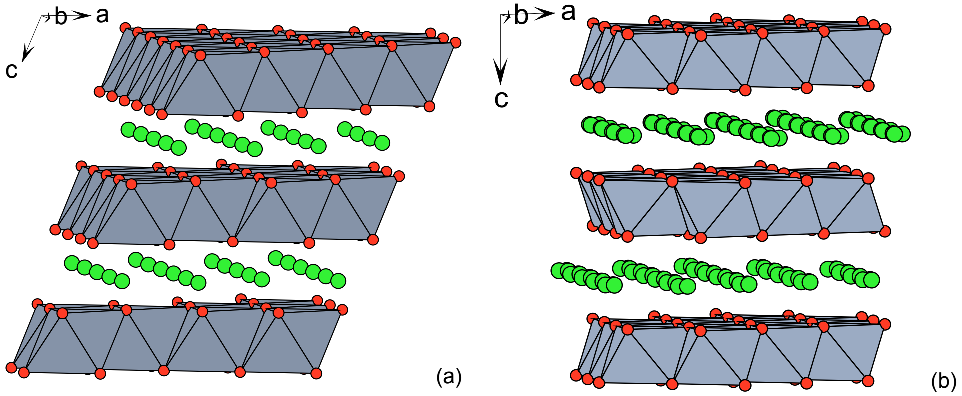

Figure 2.4: (a) Representation of O3-$NaMnO_2$ and (b) representation of P2-$Na_{2/3}Mn_{1/2}Fe_{1/2}O_2$, the grey polyhedral represents MO_6 (M = Mn, Fe) and the sodium atoms are depicted in green.

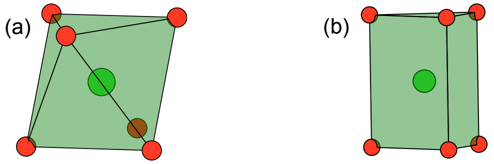

Figure 2.5: Na coordination in (a) the O3-type and (b) the P2-type layered oxide.

A plate-type oxide cathode was also investigated in this work: NaV_3O_8 [52]. This cathode material is of interest because of the presence of vanadium which exists in a wide range of oxidation states. Previously, NaV_3O_8 was considered as a cathode for Li-ion batteries [53] but in recent studies it has been used in Na batteries [52, 54]. The structure is composed of layers of VO_4 and VO_6 polyhedra separated by sodium ions in octahedral sites. As an example, Figure 2.6 shows the structure of the similar $Na_{1.2}V_3O_8$ [55].

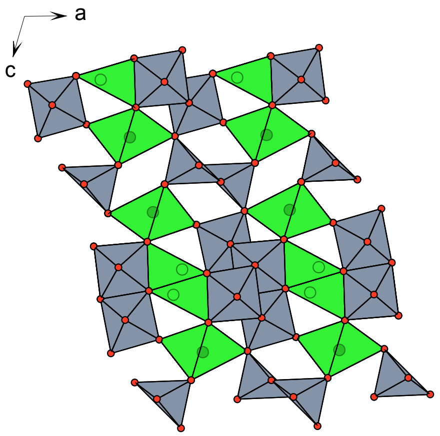

Figure 2.6: Representation of $Na_{1.2}V_3O_8$ [55] along the *b* direction, the grey polyhedra represent VO_4 and VO_6 and the sodium atoms are depicted in green (dark green and light green for the Na(1) and Na(2) Wyckoff positions, respectively).

In this material, two Na channels are observed, one along the *b* axis and one in the *a-c* plane as seen in Figure 2.6. In the first one, the conduction happens from one Na(1) Wyckoff position to the next Na(1) and from one Na(2) Wyckoff position to the next Na(2) corresponding to hopping distances of 3.6 Å. The other pathway can be described as the successive hopping: Na(1)-Na(2)-Na(2)-Na(1)-Na(1). This corresponds to the following jump distances: 3.9 Å - 2.3 Å - 3.9 Å - 4.6 Å. This distance study indicates that the first pathway is the most probable for the Na conduction as it was proposed by Schindler et al. [55] using bond valence theory.

The category described as polyanionic frameworks contains the phosphate materials, fluorophosphates, sulfates and the new nitrido- and carbonophosphates [56, 57]. They all have polyanionic 3D - framework of XO_4 or XO_3 (X = P, S) combined with MO_6 octahedra (M = metal). These materials offer several advantages as high Na^+ conductivity or computational flexibility allowing a tuneable operating voltage. In addition, they have high thermal stability as well as oxidative stability against high voltages [32].

From this category of cathode materials, $NaFePO_4$ was first investigated because of its promising olivine-type Li-analogue but $NaFePO_4$ crystallises in the maricite structure which does not provide high ionic conductivity [58]. Pyrophosphate-type electrodes $Na_2MP_2O_7$ (M = Fe, Mn, Co) were also investigated as analogues to $Li_2MP_2O_7$ compounds, and show reasonable electrochemical activities [59-61].

The more promising NASICON-type materials were thoroughly studied since the 1980's, first as solid electrolytes but later also as cathode material like $Na_3V_2(PO_4)_3$ [62, 63] or anode material like $Na_3Ti_2(PO_4)_3$ [64]. Their structure and properties will be described later in Chapter 2.3. $Na_3V_2(PO_4)_3$ is a promising cathode but its drawback is its low electronic conductivity which can be improved by processing nanoparticles of $Na_3V_2(PO_4)_3$ coated with carbon [65]. Fluorophosphate materials like $Na_3V_2(PO_4)_2F_3$ [66] or Na_2FePO_4F [67] are also attractive candidates since the voltage of the redox couple is increased from the introduction of highly electronegative fluorine atoms in the covalent polyanionic framework.

Even if they possess high moisture sensitivity which makes their processing more difficult, the sulfate and fluorosulfate materials have been developed in the recent years. The most promising sulfate cathode to date is the alluaudite $Na_2Fe_2(SO_4)_3$ showing a high potential at 3.8 V versus Na as well as fast kinetics [68]. The absence of Co in the material is also of great interest.

The last family of cathode materials for Na-ion batteries is the so-called Prussian Blue Analogues, with their general formula $Na_{2-x}M[M'(CN)_6]_y \cdot zH_2O$ (M = transition metal). They have similar structures like perovskites but show a much smaller polarisation and are therefore also potential candidates under current investigations [69].

Negative electrodes

As mentioned above, graphite cannot be used as negative electrode for Na-ion batteries. Sodium metal would be a straight forward alternative but because of safety issues and the presence of an unstable passivation layer with most common liquid electrolytes, recent studies focused on searching for alternatives [26].

As the cathode materials, the possible anodes for Na-ion batteries can be divided into 3 groups:

- Carbons
- Low potential transition-metal oxides and phosphates
- Metals and alloys [32]

Since graphite is not suitable for the too large Na ions, hard carbon (disordered carbon) is the alternative and is the most studied anode for Na-ion batteries especially because of its attractive price and low weight. Its good cyclability and efficiency were demonstrated in a cell where O3-$NaMn_{0.5}Ni_{0.5}O_2$ was used as cathode material [70].

Phosphate-type anodes belonging to the already mentionned NASICON materials are another alternative. $NaTi_2(PO_4)_3$ [71] or $Na_3Ti_2(PO_4)_3$ [64] are 2 examples of attractive candidates as negative electrodes. In addition, oxide-type anodes are investigated. Finding anode materials with suitable low voltage and high electronic conductivity is a challenge in this class of materials. However, at least one example: $Na_{0.66}Li_{0.22}Ti_{0.78}O_2$, seems to be promising as shown by Wang et al. [72].

The last family of anode materials are the metals alloying with sodium which show high energy density and low redox potential. The volume differences between the sodiated and desodiated anodes can be important so that some metals such as Pb and Bi cannot be considered. For the same reason, the use of Sn is very challenging [32]. Other metals are more promising: both Sb and amorphous P show a large reversible capacity [73, 74] and present encouraging results in the search for suitable negative electrodes for Na-ion batteries. In this work, PVD deposited Mo_3Sb_7 [75] and Cu_2Sb [76] will be further investigated. In both cases, Sb alloys with Na while Mo and Cu are considered as inactive elements that can provide more stability to the structure as well as better electronic conductivity [75, 76].

Figure 2.7 summarises the development of the above mentioned positive and negative electrode materials for Na-ion batteries with a special focus from 2010 to 2013, where the interest on Na materials started rising in the scientific community. Their potential is plotted against their theoretical capacity.

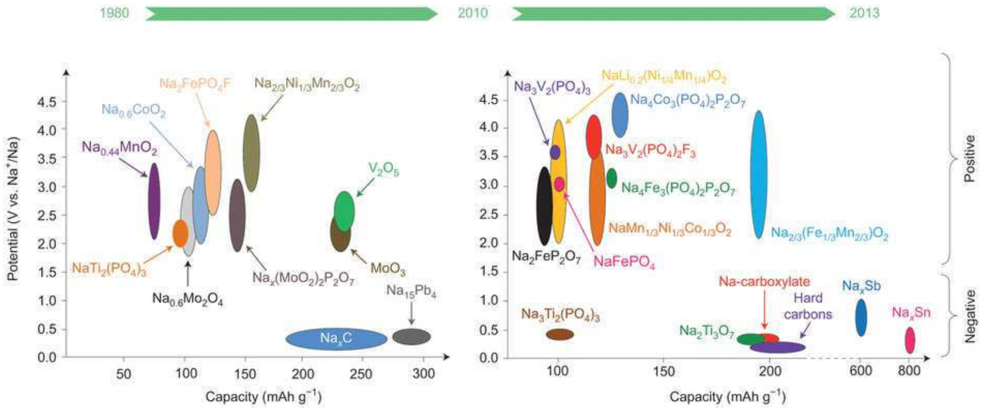

Figure 2.7: Voltage versus capacity for reported positive and negative electrode materials with plausible application in Na-ion cells within the past three decades (1980–2010; left) and as studied during the past three years (2010–2013; right). Reprinted by permission from Macmillan Publishers Ltd: Nature chemistry [23], copyright (2015)

Electrolytes

The effort in searching for suitable electrolytes in Na-ion batteries is high, as finding new liquids or solid materials with high ionic conductivity is still a challenge. As important as the conductivity is their stability against both the cathode and the anode material. The development of an electrolyte can hardly be completely independent from the electrodes.

For liquid electrolytes, the solid electrolyte interphase (SEI) which is a passivation layer at the electrode ensures the chemical compatibility. At room temperature, the possible liquid electrolytes can be aqueous, non-aqueous or ionic liquids. In the first and second case the electrolyte is a sodium salt dissolved in water or an organic solvent, in the third case it consists of an organic salt doped with the sodium salt equivalent ($R^+_{1-x}Na^+_xX^-$) [32].

The safety issues caused by the use of organic liquid electrolytes as well as their low stability against higher voltages and low thermal operation window make solid electrolytes an attractive alternative.

Nevertheless, the drawbacks of lower conductivity and contact with the electrodes need to be addressed in order to design competitive solid-state Na-ion batteries.

Different materials are possible candidates for solid electrolytes and all were already tested in different designs of all-solid-state NIBs (Chapter 2.2.3). The electrolyte of interest to date can be divided into the following categories:

- plastic crystal electrolytes (PCE) [41]
- polymer electrolytes
- glass electrolytes [77]
- ceramic electrolytes as β-alumina ($NaAl_{11}O_{17}$) discovered nearly 80 years ago [6] or the already mentioned NASICON-type materials

The PCE consists of a solid solvent doped with Na-containing salts. In the study of Zhu et al., the most conducting PCE is a succinonitrile solid solvent ($N \equiv C - CH_2 - CH_2 - C \equiv N$) with 5 mol% of $NaPF_6$ [41]. Very recently, the conductivity of polymer electrolytes was improved by preparing nanocomposite polymers: a PEO-based electrolyte with $NaClO_4$ and nano-sized TiO_2 [43].

Efforts have also been made in designing hybrid solid electrolytes (HSE) combining the advantages of the different family of materials: Kim et al. have introduced a ceramic-based HSE where NASICON $Na_3Zr_2Si_2PO_{12}$ and PVdF-HFP (Poly(vinylidene fluoride-co-hexafluoropropylene)) polymer were mixed and soaked in an ether-based liquid electrolyte [44]. Batteries built with this electrolyte contain a flammable liquid. The amount of liquid electrolyte is reduced but the safety issue is higher than for solid-state batteries.

Figure 2.8 shows the Arrhenius plot of these different types of electrolytes and the aim of conductivity at room temperature of 10^{-2} S cm^{-1} of liquid electrolytes [78].

Even if the different types of materials all show very high ionic conductivity, the ionic conductivity of a liquid electrolyte is still not reached by solid electrolytes. Nevertheless, the other advantages of stability and safety make the development of solid-state batteries important and the search for higher conductivity in solid materials necessary. In addition, depending on the application, all the described types of electrolyte show advantages. For example, the polymer and HSE allow the fabrication of flexible batteries which could be applied for portable applications.

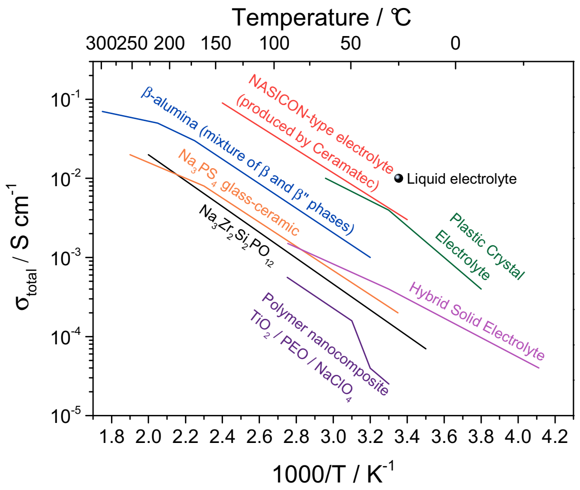

Figure 2.8: Arrhenius plot of the total conductivity of sintered polycrystalline β-alumina [79], sintered polycrystalline NASICON material from the company Ceramatec [80], sintered polycrystalline. $Na_3Zr_2Si_2PO_{12}$ [81], Na_3PS_4 glass-ceramic [77], polymer nanocomposite electrolyte [43], PCE [41] and hybrid solid electrolyte [44].

The ceramic electrolytes are very promising candidates since very high ionic conductivities can be achieved and they are competitive with the other electrolytes. Among them, β/ β''-alumina is already commercially used as the electrolyte in molten-sodium batteries [30, 33] and experienced a very long history of research. The commonly cited high conductivity of the β"-alumina of 0.1 S cm^{-1} at room temperature is a value obtained for a single crystals [82]. On an industrial scale, the β/β"-alumina samples are polycrystalline and their total conductivity including both the conductivity of the bulk (similar to the one of single crystals) and the unavoidable low conductivity of the grain boundaries is at maximum 1 - 2 × 10^{-3} S cm^{-1} at room temperature [83].

In addition, in β/β"-aluminas, the Na-ions migrate in the *a-b* plane and no conductivity can happen in the *c*-direction since it is blocked by the AlO_4 and AlO_6 polyhedra [40, 83, 84] as represented in Figure 2.9.

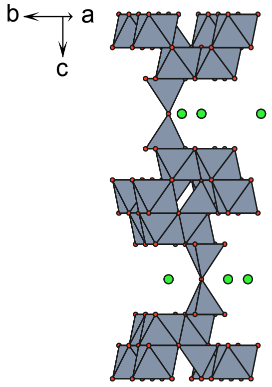

Figure 2.9: Conduction planes in the crystal structure of β-alumina [6] observed along (4 1 0). The grey polyhedra are AlO_6 and AlO_4 while the Na atoms are represented in green.

Several disadvantages as the 2-D diffusion of Na in β/β"-aluminas, the high processing temperature around 1600 ℃ [84] leading to high processing costs, the fragility at high operating temperature (around 300℃ for molten-sodium batteries) risking fracture and cell failure [85, 86] make the search for alternative ceramic electrolytes necessary.

2.3. NASICON materials

The following review on NASICON materials is described in less details in [20].

2.3.1. Definition and compositional diversity

NASICON materials were mentioned for the first time in the reports of Hong and Goodenough from 1976 on the synthesis and characterisation of $Na_{1+x}Zr_2Si_xP_{3-x}O_{12}$ ($0 \leq x \leq 3$) [10, 87]. This meanwhile popular abbreviation is used for phosphates with the generic formula AMP_3O_{12}. In this family of compositions a wide variation of substitutions have been reported and are reviewed in [19].

The A-site can be occupied by:

- monovalent cations: Li^+, Na^+, K^+, Rb^+, Cs^+, H^+, H_3O^+, NH^{4+}, Cu^+, Ag^+,
- divalent cations: Mg^{2+}, Ca^{2+}, Sr^{2+}, Ba^{2+}, Cu^{2+}, Pb^{2+},Cd^{2+}, Mn^{2+}, Co^{2+}, Ni^{2+}, Zn^{2+},

- trivalent cations: Al^{3+}, Y^{3+}, La^{3+}-Lu^{3+},
- tetravalent cations: Ge^{4+}, Zr^{4+}, Hf^{4+}
- or it can also be vacant in the case that the M-site is occupied by pentavalent cations.

In this work, A = Na.

The M site can be occupied by:

- divalent cations: Cd^{2+}, Mn^{2+}, Co^{2+}, Ni^{2+}, Zn^{2+},
- trivalent cations: Al^{3+}, Ga^{3+}, In^{3+}, Sc^{3+}, Ti^{3+}, V^{3+}, Cr^{3+}, Fe^{3+}, Y^{3+}, La^{3+}-Lu^{3+},
- tetravalent cations: Si^{4+}, Ge^{4+}, Sn^{4+}, Ti^{4+}, Zr^{4+}, Hf^{4+}, V^{4+}, Nb^{4+}, Mo^{4+}, and
- pentavalent cations: V^{5+}, Nb^{5+}, Ta^{5+}, Sb^{5+}, As^{5+}

In addition, phosphorus has been partially substituted by Si, Ge or As.

The amount of charge carriers, i.e. the element on the A-site is adapted to balance the charge suitably to the M cations and the substitution of P with aliovalent elements. In the following, only compositions with the extended general formula $Na_{1+2w+x-y+z}M^{(II)}_{w}M^{(III)}_{x}M^{(V)}_{y}M^{(IV)}_{2-w-x-y}(SiO_4)_z(PO_4)_{3-z}$ are considered.

2.3.2. Structure and Conduction Pathway

The NASICON structure consists of a three-dimensional framework of corner-sharing MO_6 octahedra and PO_4 tetrahedra. Contrary to the common opinion, not all NASICON materials have the same crystal structure. Depending on their composition, sodium- or lithium-based NASICON materials are most commonly either rhombohedral or monoclinic. Some triclinic NASICON materials have also been reported as the low-temperature phase of $LiZr_2(PO_4)_3$ [88] or $LiSn_2(PO_4)_3$ [89] but they will not be further considered here. The first described NASICON, $Na_{1+x}Zr_2Si_xP_{3-x}O_{12}$ ($0 \le x \le 3$), has a rhombohedral structure ($R\bar{3}c$) except for $1.8 \le x \le 2.2$. In this interval, the material undergoes a monoclinic distortion ($C2/c$). Both structures are represented in the *a*-*b* plane in Figure 2.10.

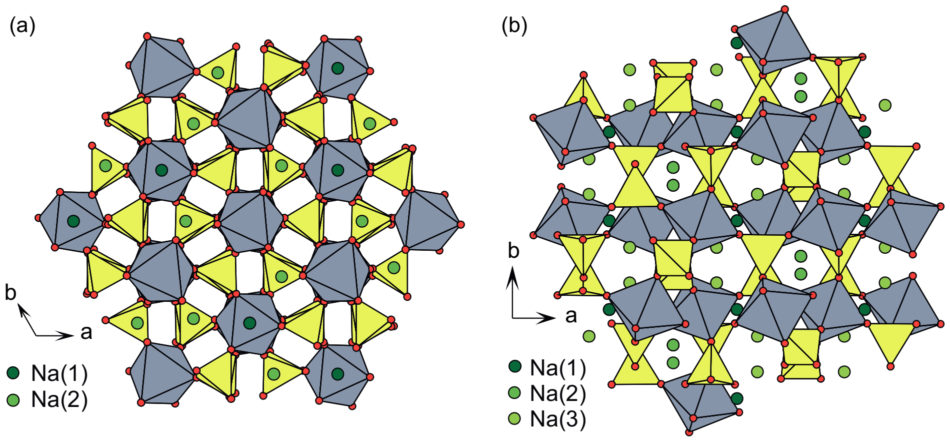

Figure 2.10: Projection in the *a*-*b* plane of (a) the rhombohedral $R\bar{3}c$ structure of $Na_3Sc_2(PO_4)_3$ [90] and (b) the monoclinic C2/c structure of $Na_3Zr_2(SiO_4)_2(PO_4)$ [10]. The Zr/ScO_6 octahedra are represented in grey and the P/SiO_4 tetrahedra in yellow.

In the rhombohedral NASICON structure, the Na^+ ions occupy two different sites when there is more than one Na atom per formula unit. The Na(1) sites are sixfold coordinated to the oxygen ions of three (Si,P)O_4 tetrahedra above and below (Na(1) coordinate (0,0,0)) as shown in Figure 2.11(a), the Na(2) sites are sixfold coordinated to oxygen ions of five $(Si,P)O_4$ tetrahedra since 2 oxygen atoms belong to the same $(Si,P)O_4$ (Na(2) coordinate (x,y,0.25)) as highlighted in Figure 2.11(b).

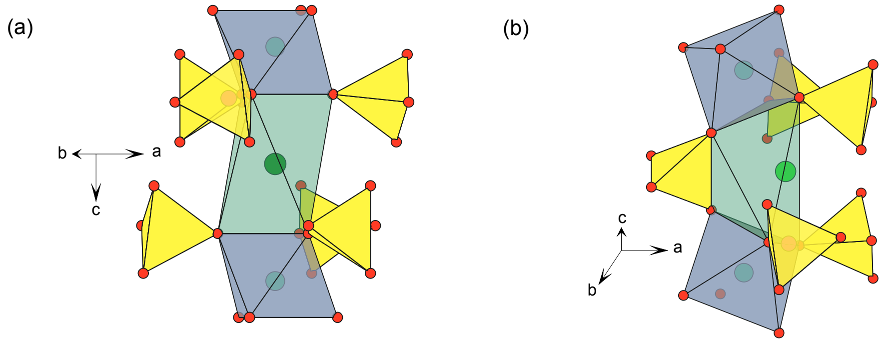

Figure 2.11: Representation of the coordination of (a) the Na(1) site, view along (1 2 0) and (b) the Na(2) site view along $(0\ \bar{1}\ 5)$ in the rhombohedral NASICON structure. The atomic positons were taken from $Na_3Sc_2(PO_4)_3$ [90]. The ScO_6 octahedra are represented in grey and the PO_4 tetrahedra in yellow.

This site occupancy was also confirmed recently for Li^+ ions in the isostructural $Li_{1+x}Al_xTi_{2-x}P_3O_{12}$ [91]. For NASICON materials with only one Na per formula unit, only the Na(1) position is occupied. A third Wyckoff position for the Na atoms is sometimes introduced in the structure as a displacement of the Na(2) position [92]. The Na^+ ions jump from one position to the next through oxygen triangles T1 and T2, the bottlenecks for the Na^+ conduction which will be discussed in detail more in Chapter 2.3.5. The conduction pathway is shown in Figure 2.12 in the rhombohedral structure of $Na_3Sc_2(PO_4)_3$ [90].

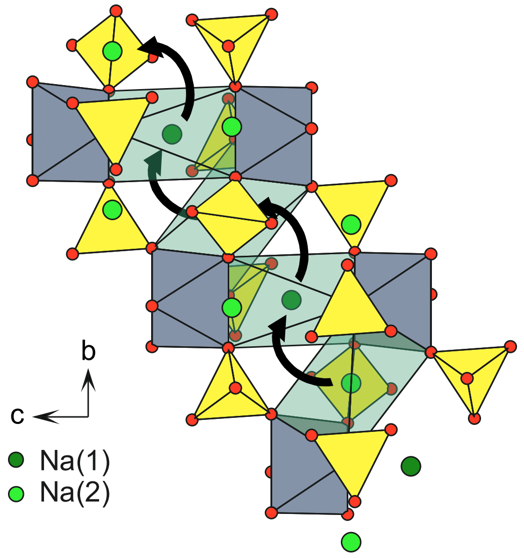

Figure 2.12: Representation of the conduction pathway in the *b-c* plane in the rhombohedral $Na_3Sc_2(PO_4)_3$ [90]. The ScO_6 octahedra are represented in grey and the PO_4 tetrahedra in yellow.

For monoclinic NASICON materials, there are three Wyckoff positions for the sodium. The Na(1) and Na(2) positions are comparable to the ones in the rhombohedral NASICON. The Na(3) sites are sixfold coordinated to the oxygen ions of three MO_6 octahedra and 2 P/SiO_4 tetrahedra (Figure 2.13).

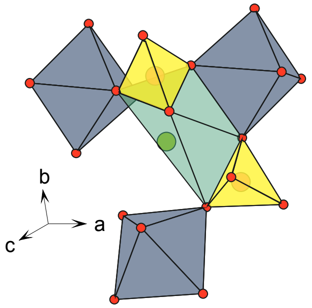

Figure 2.13: Representation of the coordination of the Na(3) site view along (1 1 2) in the monoclinic C2/c structure of $Na_3Zr_2(SiO_4)_2(PO_4)$ [10]. The ScO_6 octahedra are represented in grey and the PO_4 tetrahedra in yellow.

The conduction occurs by jumping from the Na(1) to the Na(2) or Na(3) sites through oxygen triangles as described later. The first pathway Na(1)-Na(2)-Na(1) is similar to the case of the rhombohedral NASICON in Figure 2.12. The pathway Na(1)-Na(3)-Na(1)-Na(3) is represented in Figure 2.14 for $Na_3Zr_2Si_2PO_{12}$ [10]. Along this pathway, the alternate hopping Na(3)-Na(1)-Na(3) corresponds to 2 different hopping distances, 3.52 Å and 3.85 Å for $Na_3Zr_2Si_2PO_{12}$ as seen in Figure 2.14.

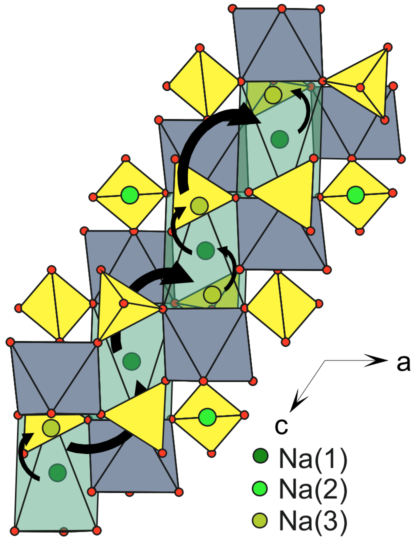

Figure 2.14: Representation of the pathway Na(3)-Na(1)-Na(3) in the *a*-*c*-plane in the monoclinic $Na_3Zr_2Si_2PO_{12}$ [10] The ZrO_6 octahedra are represented in grey and the PO_4 tetrahedra in yellow.

In both rhombohedral and monoclinic NASICON materials, the hopping distance for the Na ions ranges from approximately 2.5 to 4 Å depending on the composition of the material. Table **2.5** lists the hopping distances for all the above described pathways in rhombohedral $Na_3Sc_2(PO_4)_3$ and monoclinic $Na_3Zr_2Si_2PO_{12}$.

Table 2.5: Interatomic distances between the Wyckoff positions for the Na ions along the pathways in the rhombohedral $Na_3Sc_2(PO_4)_3$ and the monoclinic $Na_3Zr_2Si_2PO_{12}$.

	Path Na(1)-Na(2)-Na(1)-Na(2)	**Path Na(1)-Na(3)-Na(1)-Na(3)**
$Na_3Sc_2(PO_4)$ [90]	3.40 Å - 3.40 Å - 3.40 Å -3.40 Å	/
$Na_3Zr_2Si_2PO_{12}$ [10]	3.71 Å - 3.71 Å - 3.71 Å - 3.71 Å	3.52 Å - 3.85 Å - 3.85 Å – 3.52 Å

2.3.3. Ionic conductivity

The conductivity of the original NASICON material $Na_3Zr_2Si_2PO_{12}$ is 6.7×10^{-4} S cm^{-1} at room temperature and 0.2 S cm^{-1} at 300 ℃ [10]. These values are often used as a reference since they are still some of the best values achieved to date. Nevertheless, depending on the composition, the ionic conductivity of a material with a NASICON structure can vary by several orders of magnitude, for example, the lowest conductivity reported is 6×10^{-13} S cm^{-1} for $NaGe_{0.5}Ti_{1.5}(PO_4)_3$ [93, 94] which is 10 orders of magnitude lower than 5×10^{-3} S cm^{-1} for $Na_{2.96}Nb_{0.04}Zr_{1.96}Si_2PO_{12}$ [95].

To understand this large variation of conductivity values for materials with similar structures, it is crucial to identify the parameters influencing the conductivity. For that, approximately 110 different materials with the general formula $Na_{1+2w+x-y+z}M^{(II)}{}_wM^{(III)}{}_xM^{(V)}{}_yM^{(IV)}{}_{2-w-x-y}(SiO_4)_z(PO_4)_{3-z}$ containing different cations $M^{(II)}$, $M^{(III)}$, $M^{(IV)}$ and $M^{(V)}$ and different values of w, x, y and z were compared [10, 22, 87, 93, 95-117]. Their conductivities at 300 ℃ and at room temperature are summarized in Annex 1 to Annex 4. Some conductivity values have been extrapolated down to room temperature using the Arrhenius law:

$$\sigma_T \, T = A \, e^{\frac{-E_a}{kT}} \qquad \text{(Equation 9)}$$

In this equation, σ_T is the conductivity at the absolute temperature T, E_a is the activation energy composed of a barrier energy ΔH_b for charge migration and a relaxation energy ΔH_r of the local lattice environment, A is a pre-exponential constant containing the number of charge carriers, jump distance and attempt frequency [118, 119], and k is the Boltzmann constant. The value of the pre-exponential factor of the Arrhenius law, A, is also listed in Annex 1 to Annex 4. Those NASICON materials for which the activation energy has not been calculated are not included in these tables because their conductivity at room temperature could not be extrapolated. For those NASICON materials which show a phase transition, the activation energy and pre-exponential factor differed at low temperature (LT) and high temperature (HT). Typically, the transition from the low-temperature phase to the high-temperature phase occurs around 400 ℃ ± 200 ℃ and depends on the composition.

Figure 2.15 represents the Arrhenius plot of the total conductivity of polycrystalline NASICON materials with the highest conductivities compared to polycrystalline β-alumina as well as to liquid electrolyte (10^{-2} S cm^{-1} at room temperature for the Na^+ ions [78]). For the solid electrolytes shown here the conductivity at room temperature varies between 5×10^{-4} and 5×10^{-3} S cm^{-1}. In Figure 2.15, the Arrhenius curve was only plotted from 200 to 300 ℃ for $Na_{3.3}Sc_{0.3}Zr_{1.7}Si_2PO_{12}$ because no data at room temperature were available. The changes in slope correspond to phase transitions.

It is evident that the advantage of the NASICON-type materials over β-alumina is not only their cheaper processing but also their potentially higher conductivity values. Nevertheless, the best ionic conductivity values for NASICON materials are still about one order of magnitude lower than for liquid electrolytes so that their use in solid state batteries can only be achieved by finding higher conductive components or allowing a processing as thin film to compensate the lower conductivity.

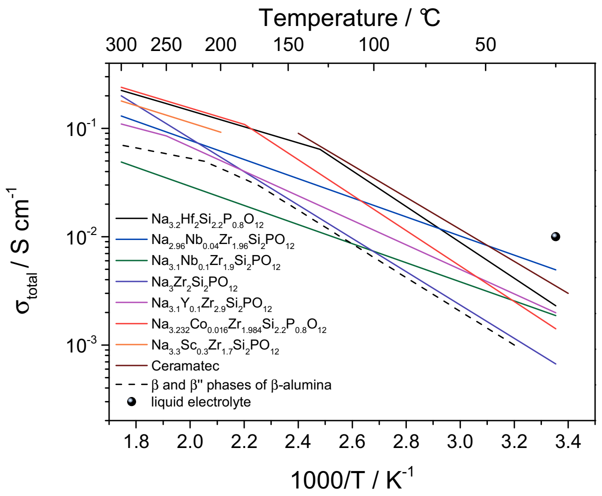

Figure 2.15: Arrhenius plot of the total conductivity of sintered polycrystalline β-alumina [79], sintered polycrystalline NASICON material from the company Ceramatec [80] and 7 of the best NASICON-type Na ionic conductors [10, 22, 95, 96, 108].

2.3.4. Correlation between composition and ionic conductivity

For the following study, it is important to keep in mind that all the gathered data were measured on polycrystalline samples and their microstructure and particularly the porosity have a significant impact on the conductivity. This influence on the data, however, could not be considered because in most the publications this information was missing. Overall, the missing correction for porosity is leading to a larger scatter of the compiled data.

Depending on the nature of the M cations and on the substitution of phosphorus by silicon, two main parameters distinguish the different NASICON materials. On the one hand, the Na content and hence the different amount of charge carriers according to the valence of M and the presence of Si to balance the charges and on the other hand the size of the unit cell and accordingly, the lattice size and hence the steric (but also electrostatic) barriers along the conduction paths in relation to the size of M and the presence of Si which has a bigger ionic radius that P when four fold coordinated (when fourfold coordinated 0.26 Å and 0.17 Å, respectively [21]). Both impacts influence the conductivity of the compounds.

Na content

In the Arrhenius expression (Equation 9), the pre-exponential factor can be written more explicitly:

$$A = N \times e^2 \times d^2 \times k^{-1} \times \gamma \times C(1-C) \times \omega_0 \times e^{\frac{\Delta S}{k}} \qquad \text{(Equation 10)}$$

In this equation, *e* is the electronic charge, *d* is the hopping distance, *γ* is a geometrical factor that may include a correlation factor, *C* is the concentration of mobile ions on *N* equivalent lattice sites per unit volume, *ω₀* is the vibrational frequency of the mobile ions in their lattice sites and *ΔS* is the entropy of the hopping process [120]. The conductivity is directly related to the total amount of charge carriers in the materials, indicating that an increase of Na per formula unit balancing aliovalent substitution in the NASICON materials will increase the conductivity. Figure 2.16 shows the evolution of the conductivity at room temperature of the NASICON materials listed in Annex 1 to Annex 4 as a function of the amount of Na per formula unit.

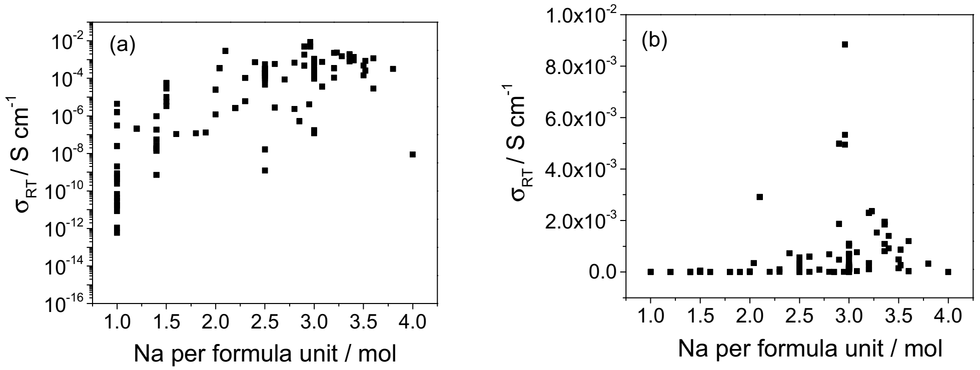

Figure 2.16: Conductivity at room temperature, $\sigma_{RT,}$ as a function of the amount of Na^+ in $Na_{1+2w+x-y+z}M^{(II)}_wM^{(III)}_xM^{(V)}_yM^{(IV)}_{2-w-x-y}(SiO_4)_z(PO_4)_{3-z}$ with (a) a logarithmic scale for the conductivity and (b) a linear one.

In Figure 2.16, the largest scatter of conductivity appears for compositions with one Na per formula unit, i.e. $NaM^{(IV)}_2(PO_4)_3$. Since the conductivity changes by about 7 orders of magnitude, this can be interpreted as a significant impact of the $M^{(IV)}$ cations influencing the bond strength and local coordination sphere of the sodium ions. However, it also can be interpreted as experimental uncertainty of the sodium content, because a very small change of charge carriers can cause a huge variation in conductivity. With higher sodium concentrations this scatter is reduced and a clear trend is visible towards higher conductivity for Na concentration up to 3-3.5 mol Na per formula unit. For a higher Na concentration in the NASICON materials, leading simultaneously to a lower amount of vacancies at the Na position, the conductivity decreases. It is essential that some Na vacancies are present in the structure to allow the motion of Na ions, otherwise the hopping from one Na position to the next is not possible since the ionic transport does not happen via interstitial sites. In the studied NASICON materials, the maximum occupancy for all the Na positions is 4 per unit cell. The highest conductivity values are obtained for NASICON materials when the ratio between occupied and vacant Na sites is 75:25 to 88:12.

Size of M cation

In order to have a comparison parameter of all the NASICON materials, an effective mean ionic radius of the cations $M^{(II)}$, $M^{(III)}$, $M^{(IV)}$ and $M^{(V)}$, r_{eff}, was defined as a geometrical parameter. For the general formula $Na_{1+2w+x-y+z}M^{(II)}_wM^{(III)}_xM^{(V)}_yM^{(IV)}_{2-w-x-y}(SiO_4)_z(PO_4)_{3-z}$, r_{eff} was calculated using the equation:

$$r_{eff} = (r_{M^{(II)}} \times w + r_{M^{(III)}} \times x + r_{M^{(V)}} \times y + r_{M^{(IV)}} \times (2-w-x-y))/2 \qquad \text{(Equation 11)}$$

In this equation, all ionic radii were taken from ref. [21]. Figure 2.17 shows the dependance of conductivity at room temperature on r_{eff}. A large scatter of the data points is observed on the logarithmic scale. Nevertheless, a maximum in conductivity is observed at about 0.72 Å and a lot of compositions have been investigated in this region. Considering a deviation of only 0.05 Å from this ideal r_{eff}, the ionic conductivity drops by one order of magnitude.

Indeed, both the Na concentration and the size of the M cations determine the properties of a NASICON material and only when both parameters are simultaneously at the optimum value, the conductivity will be high. Therefore two main results can be derived from Figure 2.16 and Figure 2.17:

- For values of r_{eff} far from 0.72 ± 0.1 Å (i.e. the ionic radius of Zr [21]), the ionic conductivity decreases exponentially.

- As the number of charge carriers increases, so does the conductivity, too, until a maximum concentration is reached, corresponding either to the optimal-filled occupancy of the Na sites or a structural change resulting in a steric barrier.

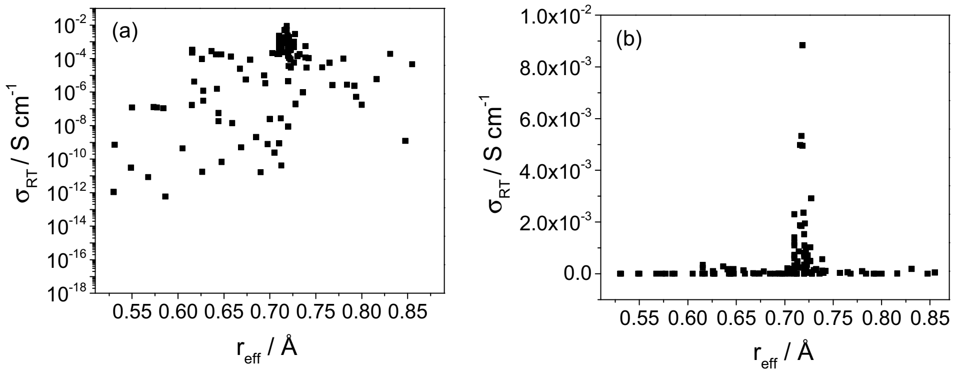

Figure 2.17: Conductivity at room temperature, $\sigma_{RT,}$ as a function of the effective ionic radius r_{eff} in $Na_{1+2w+x-y+z}M^{(II)}_{w}M^{(III)}_{x}M^{(V)}_{y}M^{(IV)}_{2-w-x-y}(SiO_4)_z(PO_4)_{3-z}$ with (a) a logarithmic scale for the conductivity and (b) a linear one.

As r_{eff} is an arithmetic average, it is important to look at the difference in ionic radii between the M cations in the same compound. It might be expected that compositions with cations of a similar size have a higher conductivity than those which contain cations of very different sizes due to the different Coulombic and steric interactions along the conduction pathway. Figure 2.18 shows the conductivity at room temperature as a function of the difference between the ionic radii of M and M' ($\Delta r_{M-M'}$) in $Na_{1+2w+x-y+z}M^{(II)}_{w}M^{(III)}_{x}M^{(V)}_{y}M^{(IV)}_{2-w-x-y}(SiO_4)_z(PO_4)_{3-z}$.No particular dependence is evident, indicating that the difference between the ionic radii of the M cations is not important, and only the arithmetic average of their ionic radii must be close to 0.72 Å.

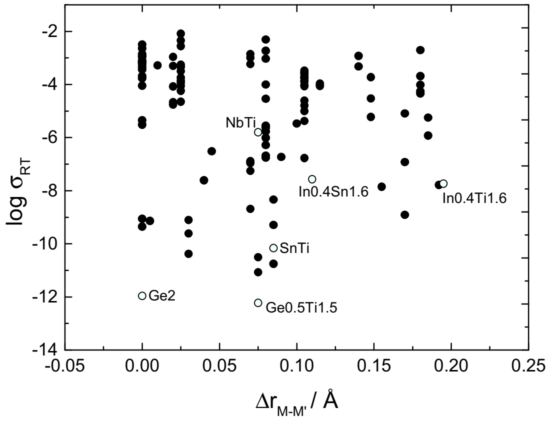

Figure 2.18: Influence of the difference of ionic radius between M and M' ($\Delta r_{M-M'}$) on the conductivity of $Na_{1+2w+x-y+z}M^{(II)}_{w}M^{(III)}_{x}M^{(V)}_{y}M^{(IV)}_{2-w-x-y}(SiO_4)_z(PO_4)_{3-z.}$ Selected data points refer to $NaGe_2(PO_4)_3$ (Ge2), $NaSnTi(PO_4)_3$ (SnTi), $Na_{1.4}Ti_{1.6}In_{0.4}(PO_4)_3$ (In0.4Ti1.6), $Na_{1.4}Sn_{1.6}In_{0.4}(PO_4)_3$ (In0.4Sn1.6), $NaGe_{0.5}Ti_{1.5}(PO_4)_3$ (Ge0.5Ti1.5) and $NaNbTi(PO_4)_3$ (NbTi). Reprinted from [20], Copyright (2014), with permission from Elsevier.

Two examples shown in Figure 2.18 are $NaGe_2(PO_4)_3$ and $NaSnTi(PO_4)_3$. Both materials have very similar conductivities at room temperature (1.1 x 10^{-12} S cm^{-1} [93] and 6.9 x 10^{-11} S cm^{-1} [115], respectively), although in the first case M = M' = Ge, and in the second case M = Sn, M' = Ti with Δr_{Sn-Ti} = 0.085 Å. Two further examples are $Na_{1.4}In_{0.4}Ti_{1.6}(PO_4)_3$ with a conductivity at room temperature of 1.9 x 10^{-8} S cm^{-1} and $Na_{1.4}In_{0.4}Sn_{1.6}(PO_4)_3$ with a conductivity of 2.7 x 10^{-8} S cm^{-1} [97]. The sodium content is the same in both cases, as is the conductivity. However, the differences between M and M' for the two compounds are different (Δr_{In-Ti} = 0.195 Å, Δr_{In-Sn} = 0.11 Å). For equal $\Delta r_{M-M'}$, like in the case of $NaNbTi(PO_4)_3$ (Δr_{Nb-Ti} = 0.075 Å) and $NaGe_{0.5}Ti_{1.5}(PO_4)_3$ ((Δr_{Ge-Ti} = 0.075 Å), different conductivities are observed (1.6 x 10^{-6} S cm^{-1} [113] and 5.9 x 10^{-13} S cm^{-1} [93, 94], respectively), which confirms the importance of the arithmetic average of the ionic radii of the M cations (r_{eff} = 0.64 Å and r_{eff} = 0.59 Å for $NaNbTi(PO_4)_3$ and $NaGe_{0.5}Ti_{1.5}(PO_4)_3$, respectively) but not their difference.

2.3.5. Bottleneck for the Na conduction

As described in Chapter 2.3.2, the importance of the size of the bottleneck in the conduction pathway of the Na^+ ions was already emphasized by Hong for the first NASICON in 1976 [10]. In the NASICON structure, it consists of two triangles of oxygen atoms which have a common MO_6 octahedral edge. The two triangle vertices are separated by a PO_4 tetrahedral edge. The positions Na(1) and Na(2) are located above and below the bottleneck, as shown in Figure 2.19.

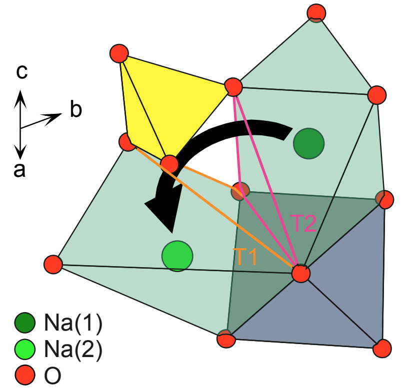

Figure 2.19: Representation of the Na(1)-Na(2) hopping through the triangles of oxygen T1 and T2 for $Na_3Sc_2(PO_4)_3$ [90] along $(2\,\bar{1}\,4)$. The ScO_6 octahedron is represented in grey and the PO_4 tetrahedron in yellow.

Losilla et al. [97] tried to find a direct correlation between the activation energy and the areas T1 and T2 through which the Na^+ ions have to move. For the rhombohedral materials $Na_{1.4}In_{0.4}M_{1.6}(PO_4)_3$ (M = Ti, Sn, Hf, Zr) such a correlation was found between the area T1 (the smaller triangle) and E_a.

As an effort to extend this observation, the area of the triangle T1 was calculated for about 30 NASICON materials for which the complete refined crystal structure is available [10, 22, 87, 90, 93, 96-102, 106, 107, 111-116, 121-133]. Data for only 2 monoclinic NASICON could be found, the others are rhombohedral. The influence of this bottleneck on the conductivity at room temperature and on the activation energy is shown in Figure 2.20.

The hypothesis of Losilla et al. is confirmed on a more general basis and wider scale: the activation energy decreases and accordingly the conductivity increases with increasing area T1, i.e. with wider ionic pathway. The results of the linear regressions are:

$\log \sigma_{RT} = 4.9 \times T1 - 31.2; R^2 = 0.41$ (Equation 12)
$E_a = -0.4 \times T1 + 2.5; R^2 = 0.59$ (Equation 13)

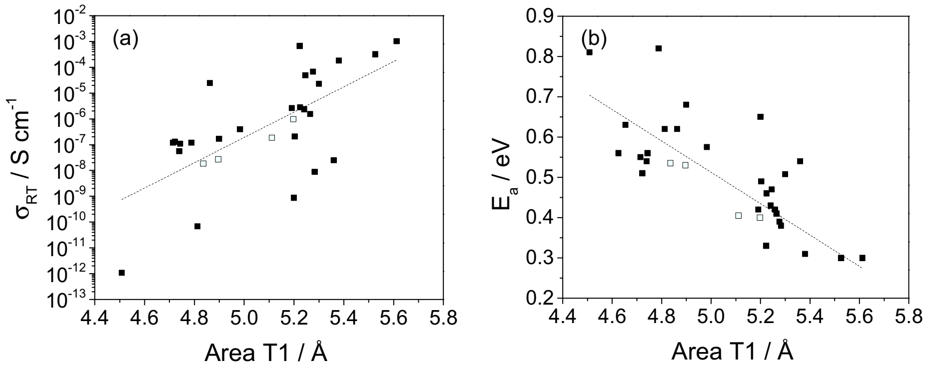

Figure 2.20: Dependence of the triangle area T1 on (a) the conductivity and (b) activation energy at room temperature for 30 NASICON materials [10, 22, 87, 90, 93, 96-102, 106, 107, 111-116, 121-133]. The open symbols represents the materials of the study of Losilla et al. [100]. The lines are the result of the linear regressions Equation 12 and Equation 13.

It is interesting to note that the compositions with the lowest E_a, the highest conductivity and largest area T1 are those with partial substitution of P with Si. This observation was made by Hong in $Na_{1+x}Zr_2Si_xP_{3-x}O_{12}$ [10] or by Vogel et al. in $Na_{1+x}Hf_2Si_xP_{3-x}O_{12}$ [22]. In both cases, the introduction of Si in NASICON materials induces a loss of symmetry, i.e. a transition from rhombohedral to monoclinic crystal structure where the sodium ions are more mobile. Unfortunately, very few refined structures are found for Si-containing NASICONs to deeply understand the impact of silicate groups in the sodium conduction.

2.3.6. Scandium-based NASICON

Since the best conductive NASICON materials should contain 3-3.5 mol of sodium per formula unit, the complete substitution of Zr with a trivalent cation is interesting and such NASICON materials were already studied in the past by Winand et al. [98] as listed in Table 2.6.

The difference of conductivities are due to the ionic radii of the $M^{(III)}$ cations. The ionic radius of Sc, r_{sc} = 0.745 Å [21], is the closest to the ionic radius of Zr and the substitution of Zr with Sc already arose interest as it was studied by Subramanian et al. [96] in 1985.

Table 2.6: Conductivity at room temperature and at 300 ℃ of $Na_3M^{(III)}_2(PO_4)_3$ NASICON materials.

$Na_3M^{(III)}_2(PO_4)_3$	σ_{RT} / S cm^{-1}	$\sigma_{300℃}$ / S cm^{-1}
$Na_3Cr_2(PO_4)_3$	1.7×10^{-7}	7.0×10^{-3}
$Na_3Fe_2(PO_4)_3$	8.2×10^{-6}	9.0×10^{-3}
$Na_3In_2(PO_4)_3$	1.8×10^{-7}	9.0×10^{-4}
$Na_3Sc_2(PO_4)_3$	2.3×10^{-5}	5.1×10^{-2}

Figure 2.21 shows the members of the solid solution $Na_{1+x+z}Sc_xZr_{2-x}Si_zP_{3-z}O_{12}$ that were investigated to date.

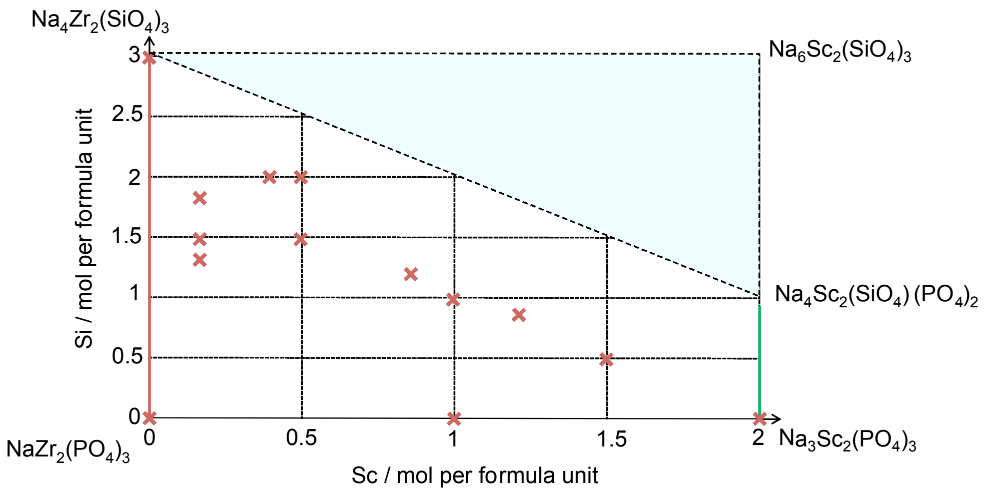

Figure 2.21: Materials of the solid solution $Na_{1+x+z}Sc_xZr_{2-x}Si_zP_{3-z}O_{12}$ formerly investigated (marked in red) [10, 96, 98]. The green line represents the solid solution investigated in this thesis.

As mentioned above, the substitution of Si in NASICON materials has a positive impact on the conductivity, therefore, the still unknown solid solution $Na_{3+z}Sc_2Si_zP_{3-z}O_{12}$ (abbreviated hereafter as $NSSiP_x$) should give high conductivity. Furthermore, the impact of introducing Si substitution in a NASICON structure still needs to be studied more systematically.

3. Materials and methods

3.1. Preparation of samples

3.1.1. Polycrystalline samples

All compositions were synthesized by conventional solid state reaction. A stoichiometric homogenised mixture of $NH_4H_2PO_4$ (Merck KGaA, 99 %), Sc_2O_3 (Projector GmbH, 99.5 %), Na_2CO_3 (Alfa Aesar GmbH & Co KG, 99.5 %), and SiO_2 (Alfa Aesar GmbH & Co KG, 99.8 %) was heated with 300 K h^{-1} to 900 ℃ for 4 h. After grinding, the powder was annealed for 20 h. The annealing temperature depended on the composition and was between 1280 ℃ and 1350℃ [96, 98, 99, 126]. The obtained powder was milled in ethanol with ZrO_2 milling balls (mixture of balls with diameter of 3 and 5 mm) with a weight ratio of powder : ethanol : milling balls = 1:2:3. After drying, the powder was uniaxially pressed with a pressure of approximately 100 MPa into pellets (13 mm in diameter, approximately 2-5 mm height) and sintered in air at the annealing temperature of the powder for 10 h with 300 K h^{-1} heating rate and 180 K h^{-1} cooling rate. The final samples all had a density of 91-96 %.

3.1.2. Single crystals

$ScPO_4$ is a needed reactant for the synthesis of single crystals of scandium-based NASICON. It was prepared via solid state reaction from a stoichiometric amount of Sc_2O_3 (Projector GmbH, 99.5 %) and $NH_4H_2PO_4$ (Merck KGaA, 99 %). The homogenised mixture was heated up with 300 K h^{-1} to 900 ℃ for 3 h. After grinding, the powder was annealed at 1200 ℃ for 20 h. The obtained powder was ball milled in ethanol and dried.

Single crystals of $Na_3Sc_2(PO_4)_3$ were synthesized using the flux method as described by Søtofte et al. [134]. A ratio 1:6 of the above mentioned $ScPO_4$ and $Na_4P_2O_7$ (Sigma-Aldrich, 95 %) was heated in a Pt crucible at 1100 ℃ for 5h in air, then cooled down to 900 ℃ at 3K h^{-1} before the furnace was free-cooled to room temperature. The single crystals were extracted from the molten mass with hot water.

Several attempts were made to synthesize $Na_{3.4}Sc_2Si_{0.4}P_{2.6}O_{12}$ using the above mentioned method with an addition of a stoichiometric amount of Na_2SiO_3 (Sigma-Aldrich, 95 %) as silicon source. A melting of $NSSiP_x$ powder was also carried out. No incorporation of Si in the crystals could be achieved in these ways.

3.1.3. Preparation of batteries with bulk mixed cathode

$Na_3V_2(PO_4)_3$ (abbreviated NVP hereafter) was synthesized by conventional solid state reaction [65]. A stoichiometric amount of V_2O_3 (Sigma-Aldrich, 99.99 %) and NaH_2PO_4 (VWR, 95%) were mixed and milled in a planetary ball mill for 5 h at 150 rpm. The powder was then annealed at 750 ℃ for 10 h in argon and rinsed with water afterwards.

A mixed cathode slurry was prepared: a weight ratio 10:43:47 of carbon black (Sigma-Aldrich), $NSSiP_{0.4}$ and NVP was mixed with 6% α-terpineol in ethylene carbonate solution (Sigma-Aldrich, 98.5 % and 98 %, respectively) and grinded with a roller mill. The slurry was hand-brushed on nearly dense $NSSiP_{0.4}$ pellets (92 %) and after drying, the pellets were sintered at 900 ℃ in Ar. The mass of the active material was 0.948 mg.

Na metal foil (Sigma-Aldrich, 99.95 %) was used as the anode material and the battery was sealed in a Swagelok cell for electrochemical testing.

3.1.4. Preparation of batteries with thin film electrode

The following cathode and anode materials were deposited as thin films using RF magnetron sputtering in Ar plasma on $NSSiP_{0.4}$ pellets (density 91-95 %) at Oak Ridge National Laboratory (ORNL) in the Materials Science and Technology Division under the kind supervision of Dr. G.M. Veith.

The advantages of working with thin film cathodes are a very low self-discharge rate and a high cycle life at deep discharge. In addition, materials with lower conductivity can be applied since it will be compensated by the thinness of the film and additives like carbon black or binders are therefore not needed. In addition, a better contact between the solid electrolyte and the cathode can be achieved by physical vapour deposition methods (PVD) as it will be described bellow in this chapter.

Nevertheless, since the mass of active material will be lower than for bulk cathodes, the specific energy is expected to be lower [135].

RF magnetron sputtering in Ar plasma

In the electrode sputtering process argon is ionised by an electric field generating a plasma. The Ar^+ ions within the plasma are accelerated towards the target composed of the electrode material. The molecules at the surface of the target evaporate and a stream of evaporated material passes through the chamber and deposits onto the substrate, in our case the $NSSiP_{0.4}$ pellet. For the sputtering of ceramic materials with low electronic conductivity or even insulators, an alternative current with radio frequency (RF) is applied. This technique is combined with a magnetron sputtering system in which a magnetic field allows the electrons in the plasma to stay near the target surface, increasing the plasma density [135].

Thin films deposited this way often show a crystallographic preferred orientation (also called texture) on the one hand due to the preferential growth of the sputtered material and on the other hand to the substrate and ion bombardment properties [136]. The preferred orientation of the thin film cathode leads to anisotropic film properties and this feature is especially important if the conduction of sodium in the thin film is anisotropic.

NaV_3O_8 cathode

The target for the NaV_3O_8 was prepared[1] by solid state reaction as described by D. Nguyen et al. [52]. The thin film deposition was carried out onto the $NSSiP_{0.4}$ pellets using RF magnetron sputtering in Ar plasma. The deposition conditions were 80 W power, 2.66 Pa pressure and 5 cm target-substrate distance resulting in a deposition rate of 2.4 nm min^{-1}. After 3 to 5 h deposition, the thin film was annealed at 400 ℃ between 1 to 12 h. Depending on the deposition time, the thickness of the NVO thin films varied between 425 and 691 nm, the mass of the active material between 0.14 and 0.22 mg.

---

[1] Courtesy of K. Browning, Materials Science and Technology Division, Oak Ridge National Laboratory

Cu_2Sb anode

The Cu_2Sb target and thin films were prepared using the parameters optimised by L. Baggetto et al. [76]: 30 W power, 2 Pa pressure and 5 cm target-substrate distance resulting in a deposition rate of 8.4 nm min^{-1}. The deposition lasted 1 h resulting in a 504 nm thick film with 0.39 mg active material.

Mo_3Sb_7 anode

The Mo_3Sb_7 target and thin films were prepared and deposited as desribed by L. Baggetto et al. [75] with the same parameters as for the Cu_2Sb anode resulting in a deposition rate of 8.1 nm min^{-1}. The deposition time was 1 h resulting in a 486 nm thick film with approximately 0.36 mg of active material (depending on the diameter of the pellet).

All the cathode and anode materials were tested against Na metal foil (Sigma-Aldrich, 99.95 %) in a Swagelok cell after sputtering a layer of Au on the cathode as current collector.

Other batteries were built combining the different cathode and anode materials described above. The self-standing batteries were sealed in a pouch bag in an Ar-filled glove box after sputtering Au on the cathode as a current collector. Copper stripes were used to connect the battery; a C-clamp was used to improve the contact between the copper stripes and the battery as seen in Figure 3.1(b), this procedure is usually used for the preliminary testing of battery materials.

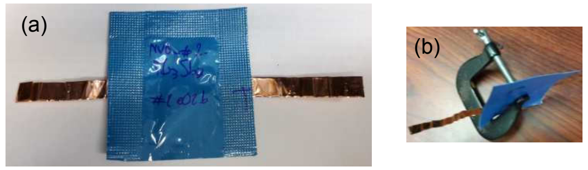

Figure 3.1: (a) Picture of a pouch bag containing a solid-state battery and (b) C-clamp improving the contact of the battery with the copper stripes.

3.2. Crystal structure determination

3.2.1. Group-subgroup relations between monoclinic and rhombohedral space groups

Na-containing NASICON materials crystallise mainly in a rhombohedral modification, but can experience a monoclinic distortion under some circumstances like different synthesis methods or certain compositions like the well-discussed example of the substitution of P with Si in the NASICON structure [10]. This distortion corresponds to a rotation of the PO_4 tetrahedra inducing a loss of symmetry. Therefore, the symmetry operations of the monoclinic phase are a subgroup of the rhombohedral group of operations.

A space group comprises the set of all symmetry operations of a 3-dimensional crystal lattice. A crystal lattice is characterised by its periodicity as the unit cell of the crystal can be indefinitely repeated using the symmetry operations of the space group to get the position of the atoms in the next unit cell. These operations can be reflections, translation or rotations. Space group $C2/c$ is a subgroup of $R\bar{3}c$ because all its symmetry operations are found in $R\bar{3}c$ [137]. This is summarised with the equation:

$R\bar{3}c - t3 \rightarrow C2/c$ (Equation 14)

where $t3$ is the space group of symmetry operations that $C2/c$ and $R\bar{3}c$ do not have in common. Table 3.1 lists the symmetry operations of both space groups. A direct comparison is difficult because the definition of the unit cell can vary. In the case of the $R\bar{3}c$ space group, the unit cell is rhombohedrally centered and the axis are commonly chosen hexagonal but another description is possible with rhombohedral axis. For the single-face centered monoclinic cell, the principal axis for the description of the symmetry operations can be the *b* or the *c* axis. In Table 3.1, the principal axis is the *b* axis.

Table 3.1: List of symmetry operations in both the rhombohedral and monoclinic modification of the NASICON structure [137].

	$R\bar{3}c$	
(1)	1	x, y, z
(2)	3^+ (rotation axis)	0, 0, z
(3)	3^- (rotation axis)	0, 0, z
(4)	2 (rotation axis)	x, x, 1/4
(5)	2 (rotation axis)	x, 0, 1/4
(6)	2 (rotation axis)	0, y, 1/4
(7)	$\bar{1}$(center of symmetry)	0, 0, 0
(8)	$\bar{3}^+$ (inversion axis)	0, 0, z; 0, 0, 0
(9)	$\bar{3}^-$ (inversion axis)	0, 0, z; 0, 0, 0
(10)	c (glide plane)	x, -x, z
(11)	c (glide plane)	x, 2x, z
(12)	c (glide plane)	2x, x, z

	$C2/c$	
(1)	1	x,y,z
(2)	2 (rotation axis)	0, y, 1/4
(3)	$\bar{1}$(center of symmetry)	0, 0, 0
(4)	c (glide plane)	x, 0, z

Even if a direct comparison is not possible in Table 3.1, it evidences the existence of more symmetry operations in the rhombohedral structure.

If one point is described in the $R\bar{3}c$ space group with its coordinates (x, y, z), the following transformation matrix *P* can be used to find the coordinates (x', y', z') of this point in the equivalent $C2/c$ space group.

$$P = \begin{pmatrix} 1 & 1 & -1/3 & -1/2 \\ -1 & 1 & 1/3 & 0 \\ 0 & 0 & 1/3 & 0 \end{pmatrix}$$

In the *P* matrix, the last column is the translation of the origin. The transformation matrix is useful to get comparable data between the rhombohedral and monoclinic NASICON unit cell. All transformed data are obtained with this matrix using the programmes and database on the Bilbao Crystallographic Server [138-140].

3.2.2. X-ray diffraction

In materials with a crystalline structure, X-rays are scattered by ordered features coherently "in-phase" in certain directions meeting the criteria for constructive interference. The conditions required for constructive interference are determined by Braggs' law.

$$n\lambda = 2d_{hkl}\sin(\theta) \qquad \text{(Equation 15)}$$

In this equation, *n* is an integer, *θ* the angle of incidence with the lattice plane and d_{hkl} the distance between lattice planes. Any set of lattice planes can be indexed by an integer triple hkl, the so-called Miller indices. They represent the points of intersections of the plane with the unit cell edges.

Where the scattered waves interfere constructively, they remain in phase since the path length of each wave is equal to an integer multiple of the wavelength. A diffraction pattern is obtained by measuring the intensity of scattered waves as a function of scattering angle (with the help of a moving X-ray detector). Very strong intensities known as Bragg peaks are obtained in the diffraction pattern when scattered waves satisfy the Bragg condition [141].

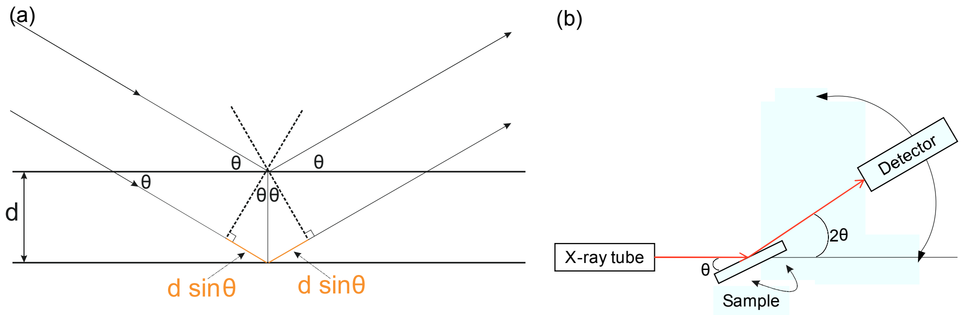

Figure 3.2: Bragg diffraction (a) [142] and schematic setting of an X-ray diffractometer (b).

For a given (hkl) reflection, there is an algebraic link between the unit cells of the analysed material and the interplanar spacing d_{hkl}, for example for a rhombohedral and a monoclinic cell [143]:

$$\frac{1}{{d_{hkl}}^2} = \frac{4}{3a^2} \times (h^2 + k^2 + l^2) + \frac{l^2}{c^2} \qquad \text{(Equation 16)}$$

for a rhombohedral unit cell where $a = b \neq c$ and $\alpha = \beta = 90$ ° and $\gamma = 120$ °

$$\frac{1}{{d_{hkl}}^2} = \frac{h^2}{a^2 sin^2\beta} + \frac{k^2}{b^2} + \frac{l^2}{c^2 sin^2\beta} - \frac{2hl cos\beta}{ac\ sin^2\beta} \times (1 - cos^2\beta)^{-1} \qquad \text{(Equation 17)}$$

for a monoclinic unit cell where $a \neq b \neq c$ and $\alpha = \gamma = 90$ ° $\neq \beta$

From Equation 16 and Equation 17, it is clear that the determination of the *d*-values of all the reflections are easily calculated knowing the space group and the lattice parameters of the studied cell. The reverse is not a simple process since the dimension pattern is one dimensional (compared to the 3-dimensional information about the unit cell) and because other parameters have influence on the powder pattern like the preferred orientation or the overlapping of reflections.

Nevertheless, the complex algorithms necessary to derive the unit cell parameters and the correct space group from a diffraction pattern have been developed and they are used during the data analysis in the Jana programme [144].

The phase purity of the different synthetized powders or sintered pellets was controlled by X-ray diffraction (XRD). The X-ray analyses were carried out with the diffractometer D4 ENDEAVOR from the company Bruker. A standard measurement programme was used, the parameters of this programme were the range of diffraction angle 2θ from 10° to 80°, increment of 0,02° for 2 θ and 0,75 second of measurement time per step. The data were analysed with the programme package X'Pert HighScore (PANalytical B.V., version 3.0.5).

High-temperature data were obtained[2] using a STOE STADI P diffractometer with curved Ge 111 monochromator and Mo $K_{\alpha 1}$ radiation and a Mythen 1K strip detector (50µm strip pitch DECTRIS") combined with the Stoe capillary furnaces. The measurement was performed from 25℃ to 600℃ with an exposure time of 20 s per temperature and a 2θ step of 0.49°.

---

[2] Courtesy of M. Yavuz and M. Knapp, Institute of Applied Material (IAM-ESS), Karlsruhe Institute of Technology

For the thin film cathodes prepared by PVD deposition, grazing incident XRD (GIXD) was used. It is an XRD technique to get information of quasi 2-dimensional surfaces in contrast to normal XRD which would penetrate too deep into the sample and give only the pattern of the substrate [145].

The GIXD data were collected using a PAN'analytical MPD Pro X-ray instrument[3]. The grazing incidence angle of the X-ray beam was 1.5 °. The measurement was carried out for 2θ between 5 and 100 °, with a 0.0167 ° increment for 2 θ and 100 second 100 s measurement time per step.

3.2.3. Rietveld method

In this work, the lattice parameters, atomic positions and site occupancies of the materials were determined using the Rietveld method in the Jana programme [144] with the full-matrix least-square against F_{hkl}^2 [146] described below. For the refinement, the XRD patterns were gathered with the same diffractometer as for the standard measurements but another measurement programme was used with following parameters: 10 ° ≤ 2θ ≤ 140 ° with 0.01° increment for 2 θ and 2 second measurement time per step.

The XRD patterns can be described as the combination of a smooth curve consisting of Gaussian peaks (sometimes overlapping or superimposed) on top of a smooth background and the Rietveld refinement consists of a complex curve fitting problem [147].

In the late 1960's, H.M. Rietveld [148, 149] realised that a neutron powder diffraction pattern can be simulated using a mathematical expression representing the observed intensity at every step, 10 years later his observations were further used with XRD diffraction patterns [150]. The calculated intensity $Y_{c,i}$ at a step i is defined as:

$$Y_{c,i} = s \times \sum_{hkl} L_{hkl} \times |F_{hkl}|^2 \times \varphi(2\theta_i - 2\theta_{hkl}) \times P_{hkl} \times A + Y_{b,i} \qquad \text{(Equation 18)}$$

In this equation, the second intensity term $Y_{b,i}$ is the intensity of the background, whereas the first term represents the contribution of every Bragg reflections and in each contribution both the crystal structure (atomic coordinates, thermal displacement and site occupancies) and the diffraction experiment (unit cell, peak profile broadening, etc.) are described with:

- s, the overall scale factor
- L_{hkl}, containing the Lorentz and polarisation factors as well as a multiplicity factor
- F_{hkl}, the structure factor for the (hkl)th Bragg reflection
- $\varphi(2\theta_i\text{-}2\theta_{hkl})$, a profile function were $2\theta_i$ is the diffraction angle corrected for the 2θ zero error
- P_{hkl}, a preferred orientation function
- A, the absorption factor depending on the instrument geometry [146, 147]

The structure factor gives information about the atoms in the structure since it is defined as:

$$F_{hkl} = \sum_{j} N_j \times f_j \times e^{(2\pi i(hx_j + ky_j + lz_j))} \times e^{\left(-\frac{8\pi^2\overline{U^2}\sin^2\theta}{\lambda}\right)} \qquad \text{(Equation 19)}$$

where:

- f_j is the atomic scattering factor
- (x_j, y_j, z_j) are the coordinate of the j^{th} atom
- U^2 is the root-mean-square thermal displacement parameter of the j^{th} atom from its average position. For atoms with low mobility in the structure, U is refined with one value and is defined

---

[3] Courtesy of J.K. Keum, Oak Ridge National Laboratory

as isotropic thermal displacement (U_{iso}), for mobiles ions, six values are needed (U_{xy} for x and y = 1,2 and 3) leading to “elongated” atoms in one space direction.

- N_j is the actual site occupancy divided by the site multiplicity.

The fitting of the observed pattern with the calculated one is obtained by a least-square minimisation of:

$$M = \sum_i w_i \times (Y_{o,i} - Y_{c,i})^2 \qquad \text{(Equation 20)}$$

where $Y_{o,i}$ is the observed intensity at a point *i* and $wi = \frac{1}{Y_{o,i}}$ [147].

This leads to a set of equations involving derivatives of the intensity at all points *i* with respect to all adjustable parameters described in Equation 18 and Equation 19. When these parameters are adjusted to minimise *M*, the entire calculated pattern “fits” the entire observed pattern.

Nevertheless, one has to be careful that the model used is adequate, this means on a mathematical level if a global minimum for *M* or a local minimum was found. For that, different indicators are introduced to describe the quality of the fitting. The most relevant mathematical figures of merit are R_p (the R-pattern) and R_{wp} (R-weighted pattern).

$$R_p = \frac{\sum_i |Y_{o,i} - Y_{c,i}|}{\sum_i Y_{o,i}} \qquad \text{(Equation 21)}$$

$$R_{wp} = \left\{\frac{\sum_i w_i \times (Y_{o,i} - Y_{c,i})^2}{\sum_i w_i \times {Y_{o,i}}^2}\right\}^{1/2} \qquad \text{(Equation 22)}$$

A third parameter, the goodness of fit (GOF) is helpful and it can be defined differently depending on the software used to carry out the refinement. With the Jana programme used in this work [144], it is defined as:

$$GOF = \frac{\sum_i w_i \times (Y_{o,i} - Y_{c,i})^2}{N - P} \qquad \text{(Equation 23)}$$

where *N* is the number of data points and *P* the number of parameters. A too small value of GOF often indicates too many refined parameters compared to the quality of the data, whereas a too high GOF could indicate an inadequate model or a false minimum.

3.2.4. Neutron scattering

The room temperature powder XRD data used for the Rietveld refinement does not always allow a precise determination of the position and occupancy of the low-weight atoms in the structure or very mobile ions, like the sodium ions in these investigations. In addition, the occupancy of Si and P could not be refined by XRD but only fixed according to the stoichiometry because of their close electronic density leading to the same atomic scattering factor (see Equation 19). On the contrary, with neutron scattering data, all atoms can be well distinguished from each other because of their different nuclear scattering lengths (Table 3.2).

Table 3.2: Nuclear scattering lengths of the atoms present in NSSiP$_{0.4}$.

Nucleus	Neutron length / fm
Na	3.630
O	5.803
P	5.130
Sc	12.290
Si	4.149

That is why, in order to get a better insight into crystallographic parameters and especially the Na positions, neutron diffraction data at lower temperature were gathered for a NSSiP$_{0.4}$ sample. They were obtained from ORNL[4] at 100 K and 300 K on the time-of-flight (TOF) diffractometer POWGEN at the Spallation Neutron Source. For each temperature one set of data was collected in the range of TOF from 9716 µs to 140000 µs (corresponds to *d*-spacing between 0.3 and 6.2 Å) with the wavelength of 1.333 Å.

Neutron scattering is a signal-limited technique because of the low interaction of the neutrons with the samples and with inherent low intensity of the signal. Nevertheless, it allows the determination of the atomic arrangement in a material and is therefore of great use for probing the structure of materials.

In a powder diffractometer at a pulsed neutron source, a pulsed beam of neutrons with a wide spectrum of energies hits the sample and the scattered neutrons are measured via detectors located at different scattering angles, and their time of flight (the time they need to arrive at the detector) is recorded. The time of flight is proportional to the wavelength of the neutron so that the *d*-spacing can be deduced using the Bragg's law (Equation 15) [151].

The obtained pattern (neutron intensity against time of flight or against *d*-spacing) can be refined using the above described Rietveld method.

For the Rietveld refinements the Jana programme was used. The background was fitted by manually set points using a polynomial interpolation and the peak profiles were modelled using pseudo–Voigt functions with back-to-back exponentials.

3.2.5. Vibrational spectroscopy[5]

Raman spectroscopy is a technique used for structural and chemical characterisation. A sample material is illuminated with monochromatic light (usually generated by a laser) and a small portion of light is inelastically scattered as it emerges at either longer or shorter wavelength than the incident light; this scattering is known as the Raman effect discovered in 1928 by Sir C.V. Raman [152]. The Raman scattering is a weak phenomenon giving very low intensities compared to the Rayleigh scattering which is the scatter that emerges with the same energy and wavelength than the incident light.

In a solid, atoms vibrate at frequencies of 10^{12} to 10^{13} Hz. These vibrations are directly related to the atomic structure of the sample. For a vibrational frequency ν_1, a laser emitting photons of light of frequency ν_0 will have the Raman lines of frequency $\nu_0 \pm \nu_1$ in its scattered beam. Indeed, the photons induce transitions in the sample and gain or lose energy by the collective vibration of the atoms. All peaks in the Raman spectrum represent a vibrational transition but not all transitions are visible. To be Raman active, the involved nuclear motion must produce a change in polarisability. Nevertheless, a Raman spectrum can be used to identify inorganic solids as they give characteristic vibrational spectra or to provide structural information [153]. The Raman active vibrations are dependent on the polarisation and direction of the incident light and Raman scattered light. The setup of the Raman experiments using polarisation filters allows the recording of Raman spectra under different configurations to obtain more information simplifying the indexing of the Raman bands. In this work, the different datasets were obtained as follows (according to the abbreviated Porto notation) [154, 155]:

- XX: meaning that both the incident light and the Raman scattered light were polarized parallel to the a axis

---

[4] Courtesy of C.M.N. Kumar, Neutron Scattering Science Division, Oak Ridge National Laboratory

[5] Courtesy of M. Giarola and G. Mariotto, University of Verona

- XY: meaning that the incident light and the Raman scattered light are polarized parallel to the a and b axis, respectively, they are perpendicular to one another.
- 45° XX and XY: for measurements on single crystals , the c direction could be parallel to a crystal face or oriented at 45 °.

The drawback of the method has always been the low intensity of the Raman scattering but it has been improved in parallel with the development of lasers and also with modalities like surface enhanced Raman, coherent Raman or resonance Raman so that the low intensity of the technique is not a problem anymore [156].

Raman spectra for polycrystalline samples of $NSSiP_x$ with x = 0, 0.2, 0.4 and 0.5 were recorded in quasi-backscattering geometry under excitation of the 514.5 nm line of a mixed Ar-Kr ion gas laser. The scattered radiation was dispersed by a triple-monochromator (Horiba-Jobin Yvon, model T64000) equipped with holographic gratings (1800 lines mm^{-1}) and coupled to a nitrogen cooled CCD detector (1024 x 256 pixels). The maximum laser power was 10 mW at the sample surface. A long-working distance objective (Olympus, with a magnification 80X) was used to focus the laser beam onto the sample surface.

In addition, Raman measurements were made on NSP single crystals with the same spectrometer. Proper orientation of a single micro-crystal, preliminarily mounted on top of a glass capillary, was achieved by means of a homemade micro-manipulator, with 6 degrees of freedom using a high angular-resolution goniometer, operated under direct optical inspection of a colour camera interfaced to the microscope objective.

For a polarisation analysis of the Raman scattering from a single crystal, spectra in different symmetry configurations have to be recorded by matching the polarisation setting (parallel or crossed) with proper orientation of the single crystal which can be achieved after aligning the *c*-axis either along or perpendicular to the direction of the electric field of the incident laser light. Accordingly to Porto's notation [155], the scattering configurations are indicated as $\overline{k_\iota}(\overline{E_\iota},\overline{E_s})\overline{k_s}$, where k_i and k_s are the propagation directions, while E_i and E_s are the polarisation directions of the incident and scattered light, respectively. In this way either parallel or crossed polarised spectra were carried out depending on the alignment of the analyser plate with respect to the polariser plate $(\overline{E_\iota}, \parallel \overline{E_s})$ or $(\overline{E_\iota} \perp \overline{E_s})$, abbreviated as XX or XY, respectively (see above).

3.3. Electrochemical characterisation

3.3.1. Impedance spectroscopy

In recent decades, impedance spectroscopy has gained an increasing role in electrochemistry and materials science since it allows the investigation of many properties of electrochemical systems. For almost any kind of solid or liquid material, ionic-conducting, semi-conducting, mixed-conducting or dielectric, the dynamics of bound and mobile charge in the bulk and interfaces can be studied so that information about microstructure, chemical composition, reaction parameters, corrosion rates, surface porosity, coating integrity, mass transfer, electrode or interface characteristics can be gathered [157-159].

Using dense pellets with gold electrodes sputtered on the surfaces, the ionic conductivity at room temperature and down to -30 ℃ was determined from impedance spectroscopy data measured with a multi-potentiostat VMP-300 from Bio-Logic SAS, France. The used frequency range was 1 Hz – 7 MHz at intervals of 20 points per decade with an amplitude of 50 mV.

The ionic conductivity at high temperature (30-400 ℃) was measured in Ar (ProGasMix from NorECs) with the Alpha-A high performance modular measurement system (Novocontrol Technologies). The frequency range used was 1 Hz – 20 MHz at intervals of 20 points per decade with an amplitude of 50 mV.

During the impedance measurement, a sinusoidal signal U_t with small amplitude U_0 is applied to the system electrode/sample/electrode:

$$U_t = U_0 \sin(\omega t) = U_0 \, e^{j\omega t} \qquad \text{(Equation 24)}$$

ω is the angular frequency :

$$\omega = 2\pi f \qquad \text{(Equation 25)}$$

where *f* is the AC signal frequency.

U_0 should be small enough to get a pseudo-linear response of the system. In this case as well as for linear systems, the current response to U_t is also a sinusoid at the same frequency but with a phase shift ϕ.

$$I_t = I_0 \sin(\omega t + \phi) = I_0 \, e^{j(\omega t + \phi)} \qquad \text{(Equation 26)}$$

where I_0 is the amplitude of the current response.

For pure resistive systems, the frequency-dependent phase shift ϕ is zero [157]. According to Ohm's law, the impedance can be calculated according to:

$$Z(\omega) = \frac{U_t}{I_t} = \frac{U_0 \, e^{j\omega t}}{I_0 \, e^{j(\omega t + \phi)}} = |Z| e^{-j\varphi} = Z' - jZ'' \qquad \text{(Equation 27)}$$

where *Z'* and *Z"* are the real and imaginary components of the complex impedance [157]. The impedance measurement is performed in a defined frequency range at discrete frequency values. For each frequency, the magnitude |*Z*| and phase ϕ are measured and *Z'* and *Z"* are extrapolated and plotted against each other in the impedance spectra as a function of frequency.

The impedance spectrum represents the imaginary (capacitive) against real (resistive) impedances. In such graphs, semi-circles representing different polarisation processes occurring in the system electrode/sample/electrode are observed. Each semi-circle (or each polarisation process) can be analysed as a combination of capacitive and resistive properties. Therefore the spectra can be simulated and fitted with an equivalent circuit composed of capacitors and resistors. Other processes like diffusion, dielectric relaxation of charge carriers, ferroelectric properties, double layer and adsorption properties of interface between electrode and sample can be simulated in the equivalent circuit but they will not be needed in this work. In the software used to analyse the impedance spectra, Zview®, a non-ideal capacitance, called constant-phase-element (*CPE*), can be used to simulate the non-perfect capacitance of an electrode/sample interface and the impedance of the *CPE* is calculated according to:

$$Z_{CPE} = \frac{1}{C_{CPE} \, (j\omega)^n} \qquad \text{(Equation 28)}$$

where ω is the frequency, *n* is an exponent usually between 1 and 0.5 [160] and C_{CPE} is related to the capacitance C according to :

$$C = R^{\frac{1-n}{n}} \times C_{CPE}{}^{\frac{1}{n}} \text{ [161]} \qquad \text{(Equation 29)}$$

When n → 1, then $C_{CPE} \rightarrow C$ and an ideal capacitor is observed. A diminishing n displays a non-ideal system and n = 0.5 corresponds to a pure diffusion process.

Figure 3.3 depicts typical impedance spectra representing known processes and the equivalent circuit elements used to describe them.

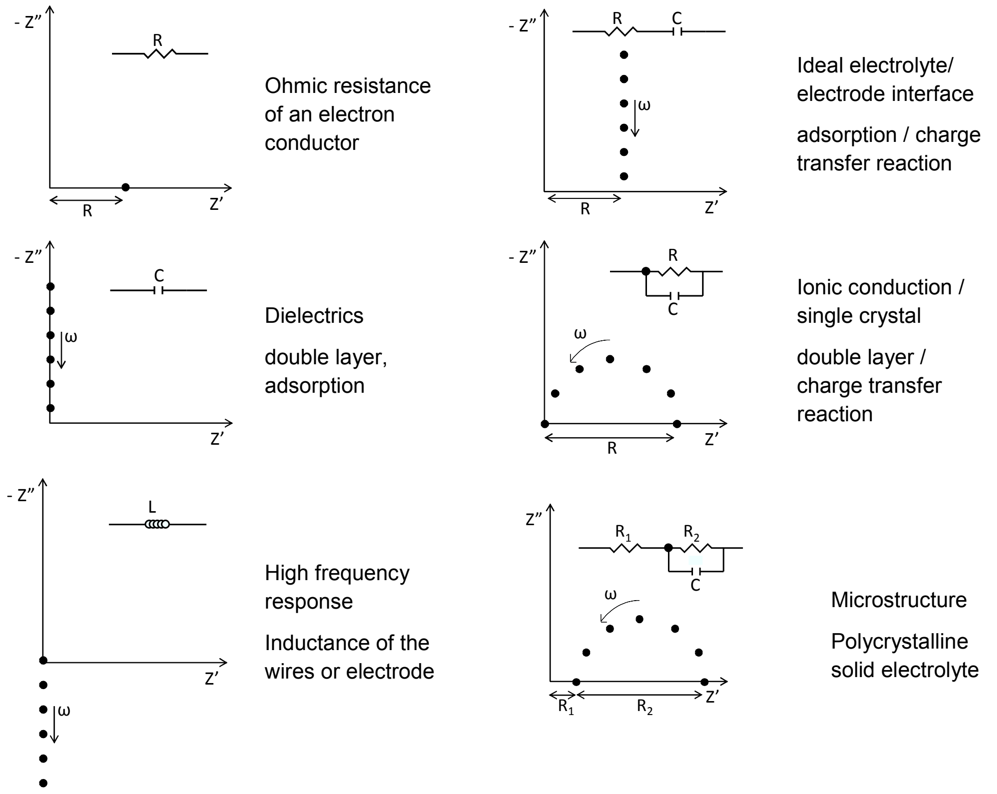

Figure 3.3: Representation of circuit elements in the complex plane plot [162].

Figure 3.4 shows an ideal impedance spectrum for a polycrystalline solid electrolyte sample with blocking electrodes (electrodes where the ionic motion does not occur). In this case, 2 semi-circles are obtained at high frequency values and a vertical tail at low frequencies. These three common elements can be attributed to the 3 processes happening in the ionic conductor: the bulk capacitance and resistance (C_1 and R_1), grain boundary capacitance and resistance (C_2 and R_2) and the capacitance of the sample/electrode interface (C_3) where the ions are blocked at the electrodes.

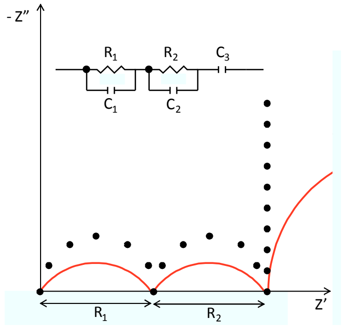

Figure 3.4: example of an ideal impedance spectrum from a polycrystalline ionic conductor compared to a typical measured impedance spectrum (red curve).

For a non-ideal impedance spectrum shown in Figure 3.4, the semi-circles appear flattened because $n < 1$ in Equation 28. Diffusion processes as well as contact issues often spoil the capacitance of both the bulk and the grain boundary conductivity. In addition, in a real impedance measurement, the blocking electrode observed at low frequency values is not a straight vertical line but another semi-circle significantly larger than at high frequency values. A resistance can be used to simulate this last semi-circle representing the ionic transport to the blocking electrode giving therefore such high values. In addition, contact problems and diffusion phenomenon affect the low frequency signal as well.

The interpretation of the model remains often controversial but Table 3.3 presents possible capacitance values and their interpretation to help distinguish the different processes.

Table 3.3: Capacitance values and their possible related phenomena [163].

Capacitance / F	Phenomenon responsible
10^{-12}	Bulk
10^{-11}	Minor, second phase
10^{-11} - 10^{-8}	Grain boundary
10^{-10} - 10^{-9}	Bulk ferroelectric
10^{-9} - 10^{-7}	Surface layer
10^{-7} - 10^{-5}	Sample/electrode interface
10^{-4}	Electrochemical reactions

For a process *x*, identified with the capacitance values described in Table 3.3, the conductivity of the process is obtained from the value of resistance in the equivalent circuit according to the expression:

$$\sigma_x = \frac{l}{A \times R_x} \quad \text{(Equation 30)}$$

where *l* is the thickness of the measured pellet and *A* the area of the electrode. Often, no distinction can be made between different processes, or the different processes cannot be attributed so that only the total conductivity of the sample is expressed as:

$$\sigma_{TOTAL} = \frac{l}{A \times \sum_x R_x} \quad \text{(Equation 31)}$$

The activation energy of the ionic conductivity of a material is also obtained from impedance data at different temperatures using the Arrhenius law (Equation 9).

3.3.2. Cyclic voltammetry

Cyclic voltammetry (CV) is a popular potentiodynamic electrochemical characterisation technique used in battery research. It gives information about the redox potential, phase transition and electron transfer kinetics that occur during the electrochemical reaction [164, 165]. In a CV experiment, the electrode potential is varied linearly with a given scan rate (in mV s^{-1}) in a defined potential range in both forward and reverse direction. The starting potential value is usually chosen before any oxidation takes place and the final value is set just after the oxidation of the redox species but before any other reaction may occur, e.g. the decomposition of the liquid electrolyte. During the scan, the current is plotted against the applied potential. In this voltammogram, the peak position observed during both forward and reverse direction corresponds to the reaction of the redox couple that occurs during the sodium insertion/extraction. As a matter of fact, for a reversible redox process where *n* electrons are exchanged as described in Equation 32, the Nernst equation shows that the potential is directly linked to the concentration of the redox species:

$$Ox + ne^- \leftrightarrow Red \quad \text{(Equation 32)}$$

$$E = E_R - (2.303)\frac{RT}{nF} \times \log\frac{[Red]}{[Ox]} = E_R - \frac{0.059}{n} \times \log\frac{[Red]}{[Ox]} \ (at\ 298\ K) \quad \text{(Equation 33)}$$

E is the applied potential, E_R is the standard redox potential of the redox couple, *[Red]* and *[Ox]* are the concentrations of the reduced and oxidized species, respectively, *R* is the gas constant, *T* the temperature, *F* the Faraday constant and *n* is defined in Equation 32, is the amount of electrons exchanged during the redox reaction [164].

A typical cyclic voltammogram of a reversible one-electron redox couple is shown in Figure 3.5. An anodic peak is observed at $E = E_p^a$ (with height i_p^a) where an oxidation is taking place and then drops because the concentration of the reducing species is diminishing. During the return scan, the reversed process occurs showing a cathodic peak (with height i_p^c) at $E = E_p^c$ typical for the reduction. For a perfectly reversible reaction, the height of the anodic and cathodic peaks should be equivalent and the separation of the oxidation and reduction peaks should be 59/n mV. Nevertheless, not only the reversibility of the redox reaction influences the potential difference between the redox peaks, a high cell resistance will also increase the potential difference between both anodic and cathodic peaks.

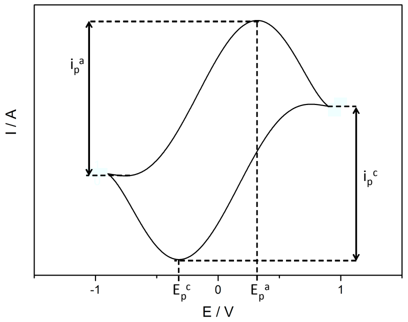

Figure 3.5: Typical cyclic voltammogram of a reversible single electron redox couple.

The response of the system applying different scan rates also gives valuable information about the kinetics of the reaction. For a perfectly reversible system, the peak current is proportional to the square root of the scan rate as described in the following equation:

$$i_p^a = i_p^c = (2.69 \times 10^5) \times n^{3/2} \times A \times D^{1/2} \times v^{\frac{1}{2}} \times C \qquad \text{(Equation 34)}$$

where *A* is the area of the working electrode, *D* is the diffusion coefficient of the electroactive species, *v* is the scan rate and *C* the concentration of the electroactive species [164]. In Equation 34, the first term corresponds to $0.446 \times F \times \sqrt{\frac{F}{RT}} = 269000$, where *F* is the Faraday constant, *T* the temperature and *R* the gas constant.

The reversibility of the system can therefore be tested by recording voltammograms at different scan rates. The position of the redox peaks of a reversible system is independent of the scan rate; a potential shift happens if the electrochemical reaction kinetics is not fast enough or for irreversible processes. For a totally irreversible reaction, the potential difference between the redox peaks is dependent on the scan rate. For quasi-reversible processes the redox peaks are smaller and are further apart than for the perfectly reversible model, the distance between the peaks are changing with changing scan rate.

3.3.3. Galvanostatic cycling

During a galvanostatic cycling experiment, the battery is charged and discharged with a constant current within a defined potential window while the variation of potential is recorded. The results of the galvanostatic cycling are plotted as the variation of the potential as a function of the capacity defined in Equation 5. For this experiment, the parameter C-rate is introduced. It corresponds to the theoretical current value that allows the cell to charge (or discharge) in 1 hour and is therefore directly linked to the applied current of the galvanostatic cycling experiment and the theoretical capacity of the battery as it was defined in Equation 3.

$$i = Q_{th} \times C\text{-}rate \times m \qquad \text{(Equation 35)}$$

where *m* is the mass of active material.

Equation 35 means that a battery charged with a C-rate of 2C will be charged in 30 min and a charging with a C-rate of 0.5C (or C/2) will last 2 hours. The use of C-rate to describe the charging and discharging current of the experiment allows the comparison of the performance of different batteries.

The electrochemical performance of the batteries with NSSiP$_{0.4}$ solid-state electrolyte were analysed by means of both cyclic voltammetry and galvanostatic cycling. A VMP-300 Multipotentiostat (BioLogic Science Instruments, France) and a battery tester MACCOR 4000 Series (MACCOR, Inc, Tulsa Oklahoma, USA) were used for both methods. Compared to the BioLogic potentiostat, the MACCOR was designed amongst other things for testing protocols that require extremely rapid voltage measurements and it has a voltage resolution of 153 µV (compared to 1 µV for the BioLogic) [166]. The BioLogic was therefore used for precise testing of half cells and the MACCOR for long-term cycling.

3.4. Other characterisation techniques

3.4.1. ICP-OES

The stoichiometry of the materials was controlled by inductively coupled plasma optical emission spectroscopy (ICP-OES).

ICP-OES measurements were carried using the Thermo Scientific iCAP7600 spectrometer with optical scale and CID semi-conductor detector, axial und radial reflection, and wavelengths between 166 nm and 847 nm[6]. 10 g of powder were mixed to 0.25 g lithium borate in a platinum crucible and heated for 0.5 h at 1000 °C. The liquefied material was dissolved in 30 mL HCl (5 %) and filled to 50 mL volume.

The weight percent of each element in the analysed sample is obtained from the measurement and if the sample contains no impurity phases as controlled via XRD, the stoichiometry of the material can be deduced. For NSSiP$_x$, the semi-quantitative results were normalised to 2 mol Sc/formula unit. The amount of oxygen per formula unit was not determined experimentally but calculated to compensate the charges.

3.4.2. Scanning electron microscopy

Scanning electron microscopy (SEM) is an imaging technique in which a sample is scanned with a focused beam of electrons. They interact with the atoms at or near the surface of the sample producing various signals giving information about the composition, the topography or electrical conductivity. In this work, both of the following signals were used [167]:

- The secondary electrons (SE) give information about the surface topography and the morphology of the sample. The SE yield is directly related to the angle between beam and sample surface so that the topography of the sample can instinctively be recognised. In

---

[6] Courtesy of V. Nischwitz, Central Institute for Engineering, Electronics and Analytics, ZEA-3, Forschungszentrum Jülich GmbH

addition, an “edge effect” can be observed when more SE escape from the edges of the sample that appear brighter.

- The back-scattered electrons (BSE) give information about the composition. As a matter of fact the brightness in a BSE image of a sample containing different phases is a function of the mean atomic number $\bar{Z}$ of the phase composition. In some cases, the $\bar{Z}$ values of 2 phases are so similar that no difference can be made in the BSE image. In this case, a difference of morphology observed with SE image can be of great help to distinguish different phases.

The SEM pictures were taken with a Zeiss Ultra 55 and a Zeiss Supra 50 VP[7] (Carl Zeiss NTS GmbH, German). The electronic conductivity of the samples was enhanced by sputter deposition of a thin platinum layer prior to the analysis.

3.4.3. Energy-dispersive and wavelength-dispersive X-ray spectroscopy

An additional feature is available for a lot of scanning electron microscopes allowing the analysis of the composition of a sample. When the sample in the SEM is bombarded with high-energy electrons, characteristic X-rays of the present elements are generated. By detecting a spectrum of the emitted X-rays in EDX (energy dispersive X-ray) or the intensity of a specific wavelength in WDX (wavelength dispersive X-ray), the elements in the sample can be identified. This analysis is qualitative but a quantitative analysis is possible [153], especially for WDX when a standard material is available for calibration.

For the EDX and WDX analysis, a calibration for each element was made with the standards listed in Table 3.4.

Table 3.4: Standards used for the calibration of the elements in NSP.

Element	Standard
O	Al_2O_3 15 kV
Na	NaCl 15 kV
P	GaP 15 kV
Sc	Sc 15 kV

The EDX analysis[8] was carried out with an AZtec (Oxford Instruments, UK) attached to a Zeiss Supra 50 VP SEM (Zeiss Microscopy GmbH, Germany). The combined WDX/EDX analyses were carried out with an INCA Wave / INCA Energy (Oxford Instruments, UK).

3.4.4. Nuclear magnetic resonance

Nuclear magnetic resonance (NMR) spectra permit the identification of individual types of nuclei in a complex molecule because the magnetic interactions are sensitive to the local environment. A detailed analysis of molecules at an atomic level is obtained [168]. Magic Angle Spinning-NMR (MAS-NMR) is the technique to obtain high resolution NMR data on solid samples. As a matter of fact, for liquids, the rapid tumbling of molecules leads to an averaging of their interactions, whereas in solids, chemical

---

[7] Courtesy of D. Sebold, Material Synthesis and processing (IEK-1) and D. Grüner, Microstructure and properties of materials (IEK-2), Forschungszentrum Jülich GmbH

[8] Courtesy of H. Wessel, Microstructure and properties of materials (IEK-2), Forschungszentrum Jülich GmbH

shifts and dipolar coupling dominate generating a wide broadening of the peaks. The sample is rotated around an axis at the magic angle $\theta_m = 54.74$ ° in order to get rid of this broadening of the peaks [169].

The MAS-NMR measurements were carried out at with a Bruker Avance 300 Spectrometer. The samples were put in ZrO_2 rotors and rotated at 30 kHz; the pulse programme was a rotation-synchronized Hahn-Echo Sequence. The reference materials used for the calibration of the different elements are summarized in Table 3.5.

Table 3.5: List of the reference materials used for the MAS-NMR measurements.

Element	**Reference**
Na	1 M NaCl in H_2O
P	85% H_3PO_4
Sc	1M $ScCl_3$ in H_2O
Si	$Si(CH_3)_4$

3.4.5. Relaxation NMR

The diffusion of atoms or ions in solids can be studied by measuring the spin-lattice relaxation rate T_1^{-1} of corresponding nuclei. T_1^{-1} is sensitive to the changes in magnetic dipolar fields and electric field gradients around the nuclei induced by the movement of atoms or ions [170].

At a given frequency ω_0, the relaxation rate depends only on the temperature. It first increases with increasing temperature before reaching a maximum for $T = T_{max}$, then decreases with increasing temperature according to:

$$\begin{aligned} T_1^{-1}(\omega_0,T) &\approx e^{\frac{E_{a(high\,T)}}{k_bT}}, \text{ if } T \gg T_{max}(\omega_0) \\ T_1^{-1}(\omega_0,T) &\approx \omega_0^{-\beta} e^{\frac{E_{a(low\,T)}}{k_bT}}, \text{ if } T \ll T_{max}(\omega_0) \end{aligned} \qquad \text{(Equation 36)}$$

Where β is a parameter that links the activation energy at low temperature $E_{a(low\ T)}$ and at high temperature $E_{a(high\ T)}$.

For one nucleus, in our case ^{23}Na, the plot of T_1^{-1} against the inverse of the temperature gives the activation energy of the sodium conductivity in the bulk material [171][9].

3.4.6. Thermal Analyses[10]

DTA/TG and DSC/TG

Differential thermal analysis / thermogravimetry (DTA/TG) and differential scanning calorimetry / thermogravimetry (DSC/TG) measurements were carried out with the calorimeter STA449 F1 Jupiter coupled to the mass spectrometer QMS 403C Aëolos from the company Netzsch. In both cases, two methods are applied simultaneously to one sample: TG with DTA or TG with DSC.

During a TG experiment, the changes in weight are measured in dependence on temperature and give information about the thermal stability, the purity and the presence of humidity in a sample.

---

[9] All NMR measurements were carried out by Dr. M. Kaus and Dr. S. Indris, Institute of Applied Material (IAM-ESS), Karlsruhe Institute of Technology

[10] All the thermal analyses were carried out at Material Synthesis and processing (IEK-1), Forschungszentrum Jülich GmbH by M.T. Gerhards and S. Pristat.

The DTA experiment records the temperature differences between the sample and a reference while they undergo identical thermal cycles; a DTA curve is therefore a plot of the differential temperature against temperature (or time) and the peaks orientation depends on the observed phenomenon either as exothermic (downwards peak) or endothermic (upwards peak). For example, the following phenomenon can be observed:

- Crystal structure change, phase transition (exo- or endothermic)
- Crystallisation (exothermic)
- Melting (endothermic)
- Solid state reaction (exo- or endothermic)
- Oxidation or reduction (exothermic / endothermic)

The DSC experiment records the quantity of heat that is absorbed or released by a substance undergoing a physical or a chemical change during a thermal cycle. There again, the orientation of the peak indicates an exothermic (crystallisation, decomposition) or endothermic (glass transition, melting, evaporation) phenomenon [172]. In this experiment, the height of the peaks is directly influenced by the heating rate. A mass spectrometer is coupled to the DSC/TG in order to get information about the nature of the species released from the sample during the heating.

Dilatometry

The dilatometry experiments were carried out with a Dilatometer 402C and 402E from Netzsch. During the measurement, a sample is heated and its length change is recorded.

The dilatometer was used on sintered samples to measure the dimensional changes as function of temperature to determine the coefficient of thermal expansion (*CTE*). In a temperature range ΔT, a sample with a reference length L_0 will have a length change ΔL and its *CTE* is calculated according to:

$$CTE = \frac{\Delta L}{L_0 \Delta T} \quad \text{(Equation 37)}$$

From the dilatometer measurement, a plot of $\frac{\Delta L}{L_0}$ against the temperature is obtained and the CTE can be calculated from the slope of the linear data.

Dilatometry experiments were also carried out on hand-pressed powder to get knowledge on the sintering behavior, since during sintering the shrinkage of the sample that is recorded during the dilatometry experiment is associated with the grain size and morphology changes [173]. During the sintering experiment, the sample is heated up to a given temperature and the temperature is hold for a given time. $\frac{\Delta L}{L_0}$ is plotted against the temperature or against the time during the isothermal period of the thermal programme.

3.5. Theoretical investigation

The activation energy of the sodium diffusion in $Na_{3.5}Sc_2Si_{0.5}P_{2.5}O_{12}$ was also obtained using computational calculations[11].

Density functional theory

Density functional theory (DFT) is a method commonly used in computational materials science to calculate the electronic structure and related properties of many body systems. The theory basically

---

[11] Courtesy of K. Bhat, Quantum Theory of Materials (PGI-1/IAS-1),Forschungszentrum Jülich GmbH

describes the properties of a system as a function of the ground state charge density of an interacting system. The theory was put forth in the seminal paper by Hohenberg and Kohn [174] and was followed by the formalism of Kohn and Sham [175] which is the method that is widely used today. DFT provides a highly efficient and accurate method of calculating electronic structures for various kinds of systems. The predictive power of DFT in combination with the continuous growth in high performance computing systems gives a platform for calculating transport properties of materials for use in solid-state batteries.

Nudged Elastic Band Method

In order to investigate the diffusion in solids, the central problem is to calculate the minimum energy pathway for ionic transport. The point with the highest energy along this path is the saddle point, which defines the migration barrier for the transport. The ionic conductivity is exponentially dependent on the migration barrier via the Arrhenius equation (Equation 9). The Nudged Elastic Band (NEB) [176] is a chain of states method which converts the saddle point problem into a minimisation problem, and defines a procedure to calculate the migration barrier. In this work, a variation of the NEB method, called the climbing image NEB (cI-NEB) [177] was used.

Computational Details

For the current work, DFT was implemented in the *ab-initio* electronic structure code VASP [178-182] and for the NEB calculations the implementation of the Henkelman group at UT Austin [177] was used. More computational details are given in [183].

To shorten the calculation time, the rhombohedral cell described with hexagonal axis and containing 6 formula units per unit cell was transformed in its equivalent cell with rhombohedral axis containing only 2 formula units per unit cell [184]. With the simplified unit cell, it is easier to identify the ground state for $NSSiP_{0.5}$. Using the lowest energy structure, the lattice parameters were optimised and are summarized in

Table **3.6**.

Table 3.6: lattice parameters of the ground state of $NSSiP_{0.5}$ described with hexagonal and rhombohedral axis

Rhombohedral axis	$a = b = c$ = 9.05 Å and $\alpha = \beta = \gamma$ = 60.52°
Hexagonal axis	$a = b$ = 9.06 Å and c = 22.18 Å

4. Results part 1: Study of the scandium-based solid solution

In this chapter, the solid solution NSSiP$_x$ is systematically studied for $0 \leq x \leq 0.8$. Its composition and crystal structure are first investigated, followed by a description of the thermal behavior of the compounds. The results of conductivity and activation energy for the Na hopping are then described.

4.1. Composition

Before the sintering of the powder, ICP-OES measurements were carried out on the NSSiP$_x$ samples to control their stoichiometry. The results are summarized in Table 4.1.

Table 4.1: ICP-OES results for the NSSiP$_x$ solid solution.

Desired composition	Na / mol	P / mol	Sc / mol	Si / mol
$Na_{3.1}Sc_2P_{2.9}Si_{0.1}O_{12}$	2.8 ± 0.2	2.93 ± 0.15	2 ± 0.09	0.109 ± 0.007
$Na_{3.2}Sc_2P_{2.8}Si_{0.2}O_{12}$	2.99 ± 0.05	2.90 ± 0.05	2 ± 0.03	0.219 ± 0.005
$Na_{3.3}Sc_2P_{2.7}Si_{0.3}O_{12}$	3.02 ± 0.07	2.71 ± 0.06	2 ± 0.03	0.291 ± 0.006
$Na_{3.4}Sc_2P_{2.6}Si_{0.4}O_{12}$	3.04 ± 0.06	2.58 ± 0.04	2 ± 0.01	0.388 ± 0.008
$Na_{3.5}Sc_2P_{2.5}Si_{0.5}O_{12}$	3.01 ± 0.08	2.46 ± 0.04	2 ± 0.01	0.49 ± 0.01
$Na_{3.6}Sc_2P_{2.4}Si_{0.6}O_{12}$	3.07 ± 0.08	2.43 ± 0.04	2 ± 0.03	0.60 ± 0.01
$Na_{3.8}Sc_2P_{2.2}Si_{0.8}O_{12}$	3.28 ± 0.08	2.16 ± 0.03	2 ± 0.01	0.80 ± 0.02

The ICP-OES results show that the substitution of P with Si was successful with a good precision. However, the Na concentration is lower than expected for every composition. A significant loss of Na occurs during the synthesis of the powder. To quantify mass loss, a DTA/TG measurement was carried out up to 1500 ℃ and is shown in Figure 4. 1.

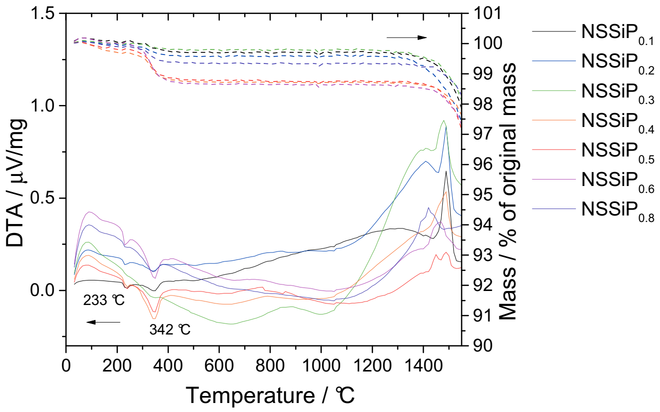

Figure 4.1: DTA/TG measurements of NSSiP$_x$.

The TG curves show a weight loss around 1300 °C that can be explained by the sodium evaporation from the material. As a reminder 1300 °C is also the annealing temperature of the material. The sodium is lost from the structure during the heat treatment of sample preparation. In Figure 4.1, a weight loss is also observed around 300°C, which represents the evaporation of crystal water contained in the material during the storage in ambient air. The influence of the storage of the NSSiP$_x$ samples in ambient conditions will be discussed further in Chapter 4.4.4.

To prevent this sodium deficiency in the composition, NSSiP$_x$ was synthesized with an excess of Na source. In accordance with the ICP-OES results, 10 % Na_2CO_3 was added for $0.1 \leq x \leq 0.4$ and 15 % for $0.5 \leq x \leq 0.8$. The phase purity of these new samples was controlled by XRD. The results are summarized in Figure 4.2.

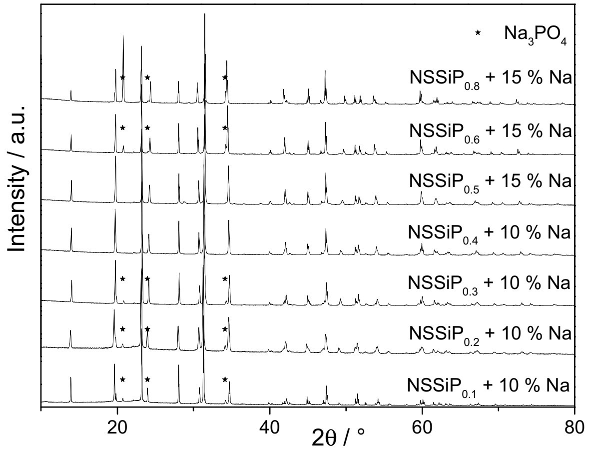

Figure 4.2: XRD Pattern of NSSiP$_x$ with excess of Na.

The presence of a Na_3PO_4 impurity is hard to be avoided when introducing an excess of sodium source during the powder preparation. The stoichiometry of the NSSiP$_x$ compounds was controlled by ICP-OES but cannot be precisely analysed because of the presence of the Na_3PO_4 impurities. Only for the pure phase materials: NSSiP$_{0.4}$ synthesised with 10 % and NSSiP$_{0.5}$ with 15 % of excess of the sodium source can the stoichiometry be calculated from the ICP-OES results. The obtained compositions are summarized in Table 4.2.

For both materials, the amount of Si and P corresponds to the expected concentration with a good precision. On the contrary, the Na concentration is higher than expected so that the desired composition was not achieved.

Table 4.2: Stoichiometry determined with ICP-OES of two samples with Na excess. The experimental errors are given in brackets.

Sample	Stoichiometry determined via ICP-OES
NSSiP$_{0.4}$ + 10 % Na	$Na_{3.51(0.06)}Sc_2Si_{0.37(0.01)}P_{2.55(0.03)}O_{11.87}$
NSSiP$_{0.5}$ + 15 % Na	$Na_{3.89(0.09)}Sc_2Si_{0.47(0.02)}P_{2.46(0.06)}O_{12.04}$

The Na evaporation is hard to quantify or to predict precisely. In addition, the use of larger amount of Na source during the solid state reaction often leads to the presence of secondary Na-rich phases. That is why, except if mentioned otherwise, the materials studied in the following were prepared with a stoichiometric amount of sodium source and a deficiency of sodium of approximately 10 % of Na after annealing can be expected. The influence of the Na concentration on the conductivity of the materials will be discussed in Chapter 4.4.2.

4.2. Crystal structure

4.2.1. XRD results

The following results are partially described in [185]. For $x \geq 0.1$, $NSSiP_x$ crystallises with rhombohedral structure at room temperature (Figure 4.3a). $NSSiP_{0.05}$ is a mixture of rhombohedral and monoclinic phase as shown in Figure 4.3b, in which the XRD patterns of the samples $NSSiP_{0.05}$ and $NSSiP_{0.1}$ are enlarged between $18° < 2\theta < 30°$. The appearance of three reflections at $2\theta = 19.5°$ and two reflections at $2\theta = 28°$ are characteristic for the presence of the monoclinic phase in the powder [186].

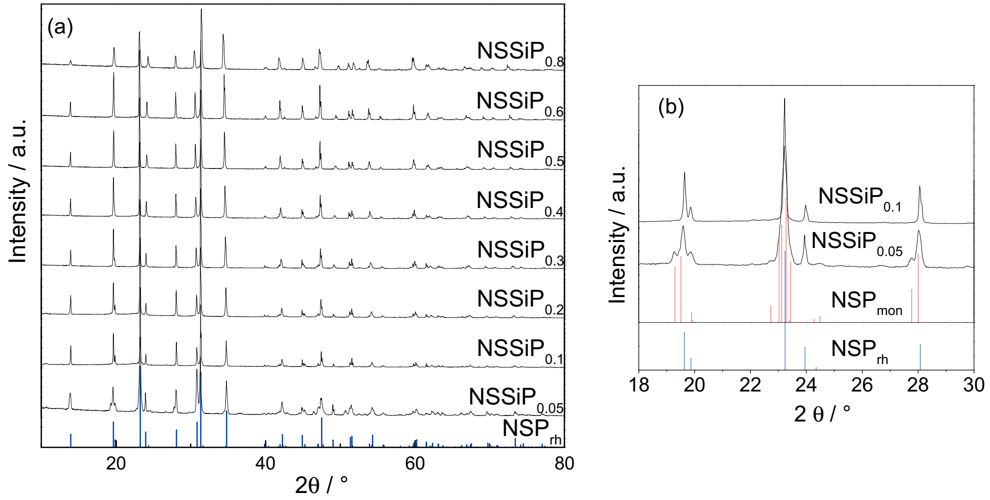

Figure 4.3: (a) XRD patterns of $NSSiP_x$ for $0.05 \leq x \leq 0.8$. (b) Detail of the XRD patterns of $NSSiP_{0.05}$ and $NSSiP_{0.1}$ between $2\theta = 18°$ and 30° and comparison with the XRD patterns of rhombohedral and monoclinic $Na_3Sc_2(PO_4)_3$ [186] (NSP_{rh} and NSP_{mon}, respectively).

The lattice parameters, atomic positions and site occupancies were determined using the Rietveld method. For the batches of single phase powders used for the refinement, the stoichiometry was controlled with ICP-OES and the Na contents were used as total occupancy for the Na positions. The stoichiometry used for the refinement is summarized in Table 4.3 for each composition

Table 4.3: Stoichiometry of the $NSSiP_x$ compounds used for the refinement of the structure.

Compound	Refined stoichiometry
$NSSiP_{0.1}$	$Na_{2.90}Sc_2Si_{0.1}P_{2.9}O_{11.9}$
$NSSiP_{0.2}$	$Na_{2.99}Sc_2Si_{0.2}P_{2.8}O_{11.9}$
$NSSiP_{0.3}$	$Na_{3.02}Sc_2Si_{0.3}P_{2.7}O_{11.9}$
$NSSiP_{0.4}$	$Na_{3.12}Sc_2Si_{0.4}P_{2.6}O_{11.9}$
$NSSiP_{0.5}$	$Na_{3.34}Sc_2Si_{0.5}P_{2.5}O_{11.9}$
$NSSiP_{0.6}$	$Na_{3.40}Sc_2Si_{0.6}P_{2.4}O_{11.9}$
$NSSiP_{0.8}$	$Na_{3.51}Sc_2Si_{0.8}P_{2.2}O_{11.9}$

The starting parameters of the crystal structure refinement were taken from the rhombohedral high-temperature structure of $Na_3Sc_2(PO_4)_3$ described by Collin et al. [186] and the Pseudo-Voigt profile function was used. The profile function could be improved by introducing a secondary phase of the monoclinic low temperature structure of $Na_3Sc_2(PO_4)_3$ [186] allowing the R_p value to diminish from approximately 4.4 % to 3.6 %. Nevertheless, the amount of secondary monoclinic phase was then refined and for all the compositions it was less than 2 % which is under the detection limit of the XRD considering the background. The Rietveld refinement was therefore carried out without the presence of the monoclinic phase, keeping it in mind to explain the small deviations.

All atomic positions, lattice parameters and thermal displacement parameters could then be refined for Sc, P/Si and O. Full site occupancy was fixed for the Sc and O positions and the site occupancy of P/Si was fixed in accordance with the stoichiometry.

After refining the framework atoms, the occupancy of the atomic positions Na(1) and (Na(2) (*6b* and *18e*, respectively) was refined but the obtained Na concentration in the structure model was lower than the Na content determined by ICP-OES. Trying to fix the occupancy at higher values resulted in thermal displacement parameters with negative electron density for at least one of the Na positions. That is why a third Wyckoff position for Na was introduced in analogy to the structure refinements of $Na_{3.35}Zr_2Si_{2.35}P_{0.65}O_{12}$ [92]. This new Na position corresponds to a displacement of the Na(2) position due to the high mobility of the Na ions in the materials at room temperature. The R_p value then decreased from 12-10 % to 7-5 % depending on the composition. No other possible Na position could be found.

The ratio of the occupancy of the Na(1), Na(2) and Na(3) positions was fixed as a starting value similar to $Na_{3.35}Zr_2Si_{2.35}P_{0.65}O_{12}$ [92] but adapted to the stoichiometry determined by ICP-OES. The thermal parameters were refined with fixed occupancy and showed negative values for at least one of the Na positions. The occupancy and thermal parameters were then alternatively constrained until positive values for all the parameters were obtained. All atomic positions and thermal displacement parameters were then refined with fixed occupancy and the R_p value decreased from approximately 7-5 % to 5-4 %. The results of the refinement are summarized in Table 4.4 and Table 4.5. As an example, the refinement pattern of $NSSiP_{0.4}$ is shown in Figure 4.4.

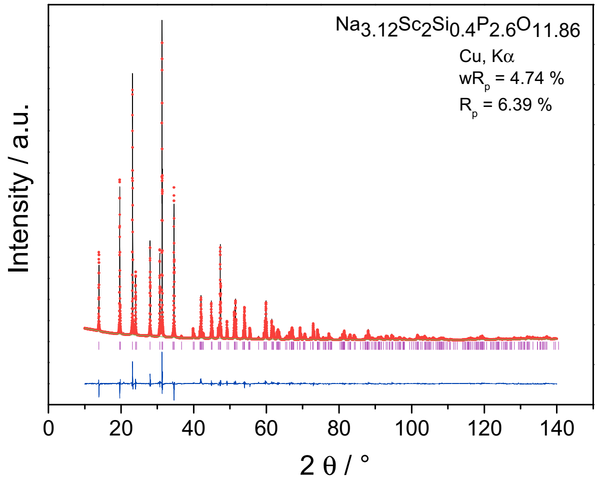

Figure 4.4: XRD powder pattern and Rietveld refinement pattern for $NSSiP_{0.4}$. The calculated data are drawn as red dots, the observed data as a black line and the difference between them is plotted in blue at the bottom. Pink vertical markers below the diffraction patterns indicate the positions of the Bragg reflections.

Table 4.4: Crystallographic and structural data of the NSSiP$_x$ compounds (standard deviations are in brackets).

Compound	NSSiP$_{0.1}$	NSSiP$_{0.2}$	NSSiP$_{0.3}$	NSSiP$_{0.4}$	NSSiP$_{0.5}$	NSSiP$_{0.6}$	NSSiP$_{0.8}$
Formula weight [g·mol^{-1}]	438.1	441.3	441.2	443.2	448.9	449.7	450.9
Crystal system	rhombohedral						
Space group, *Z*	$R\bar{3}c$, 6						
a [Å]	8.93926(3)	8.95795(4)	8.96890(4)	8.98000(2)	8.99614(4)	9.00460(3)	9.03343(2)
c [Å]	22.2735(1)	22.2601 (2)	22.2388(2)	22.2212(1)	22.1528(2)	22.1261(1)	21.9901(1)
V [Å^3]	1541.42(1)	1546.96 (1)	1549.29 (1)	1551.85 (1)	1552.65 (1)	1553.69 (1)	1554.05 (1)
$r_{c.}$ [g·cm^{-3}]	2.8317	2.8422	2.8373	2.8454	2.8806	2.8838	2.8908
Temperature of data collection [K]	298.5						
2θ range [°]	10.00 – 139.99						
Absorption coefficient, *μ* [mm^{-1}]	17.718						
Refinement method	full matrix least square against F²						
Data points / number of parameters	13000 / 23	13000 / 23	13000 / 23	13000 / 23	13000 / 23	13000 / 23	13000 / 23
R$_p$ / R$_{wp}$ / GOF (all data)[a]	6.82 / 9.24 / 4.67	5.84 / 8.54 / 4.28	5.33 / 7.76 / 3.05	4.74 / 6.39 / 3.23	5.14 / 7.15 / 2.81	4.23 / 6.01 / 3.11	4.94 / 6.72 / 3.39

[a] $R_p = \Sigma |y_o - y_c| / \Sigma y_o$, $R_{wp} = \Sigma [w(y_o - y_c)^2 / \Sigma w y_o^2]^{1/2}$, $GOF = (R_{wp}/R_{exp})^2$ with $R_{exp} = [(N-P)/ \Sigma w y_o^2]^{1/2}$, $w = 1/\sigma^2$

The differences in intensity between the observed and calculated pattern are due to the difficulty to refine the positions and occupancy of the highly mobile Na-ions at room temperature. Furthermore, the observed secondary monoclinic phase was not refined also leading to more differences between the refined and observed data. Nevertheless, since all data were refined using the same method, trends can be deduced from this study.

With increasing Si content, the hexagonal lattice parameters *a* and *c* decreases and increases, respectively (Figure 4.5a). Accordingly, the cell volume increases with the substitution and a plateau is reached at around x = 0.6, as presented in Figure 4.5b.

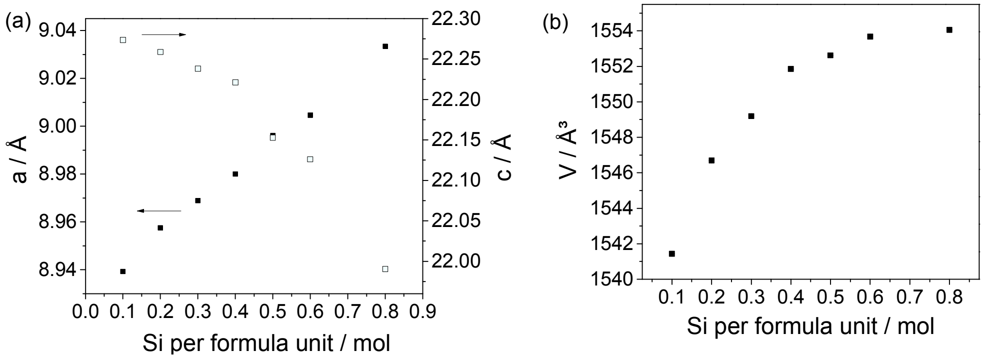

Figure 4.5: (a) Lattice parameters and (b) cell volume as a function of x in NSSiP$_x$.

Table 4.5: Positional and isotropic displacement parameter [$10^4 \cdot pm^2$] of NSSiP$_x$ with $0.1 \leq x \leq 0.8$ (standard deviations are in brackets).

Atom	Wyckoff position	Occupancy	x	y	z	U_{iso}
NSSiP$_{0.1}$						
Sc	*12c*	1	0	0	0.14909(5)	0.0098(2)
P / Si	*18e*	0.9667 / 0.0333	0.2936(2)	0	0.25	0.0097(4)
O1	*36f*	1	0.1858(3)	-0.0247(3)	0.19403(9)	0.0261(8)
O2	*36f*	1	0.1920(2)	0.1697(2)	0.08660(9)	0.0221(6)
Na1	*6b*	0.4	0	0	0	0.036(3)
Na2	*18e*	0.6167	0.6359(4)	0	0.25	0.029(1)
Na3	*36f*	0.1	0.974(2)	0.726(2)	0.9579(5)	0.019(4)
NSSiP$_{0.2}$						
Sc	*12c*	1	0	0	0.14894(5)	0.00094(2)
P / Si	*18e*	0.9333 / 0.0667	0.2954(2)	0	0.25	0.0177(4)
O1	*36f*	1	0.1827(3)	-0.0265(3)	0.19410(9)	0.0310(8)
O2	*36f*	1	0.1920(2)	0.1749(2)	0.08672(9)	0.0174(6)
Na1	*6b*	0.47	0	0	0	0.019(2)
Na2	*18e*	0.58	0.6369(5)	0	0.25	0.018(1)
Na3	*36f*	0.13	0.972(1)	0.713(1)	0.9435(4)	0.007(2)
NSSiP$_{0.3}$						
Sc	*12c*	1	0	0	0.14882(5)	0.0127(3)
P / Si	*18e*	0.9 / 0.1	0.2951(2)	0	0.25	0.0211(4)
O1	*36f*	1	0.1825(3)	-0.0262(3)	0.19383(9)	0.0275(8)
O2	*36f*	1	0.1914(2)	0.1753(2)	0.0865(1)	0.0227(6)
Na1	*6b*	0.51	0	0	0	0.021(2)
Na2	*18e*	0.5267	0.6394(5)	0	0.25	0.014(1)
Na3	*36f*	0.155	0.972(1)	0.703(1)	0.9409(4)	0.006(2)
NSSiP$_{0.4}$						
Sc	*12c*	1	0	0	0.14889(3)	0.0099(2)
P / Si	*18e*	0.8667 / 0.1333	0.2956(1)	0	0.25	0.0161(2)
O1	*36f*	1	0.1846(2)	-0.0252(2)	0.19441(6)	0.0272(5)
O2	*36f*	1	0.1905(2)	0.1728(2)	0.08634(6)	0.0158(4)
Na1	*6b*	0.52	0	0	0	0.022(1)
Na2	*18e*	0.5567	0.6389(3)	0	0.25	0.0138(7)
Na3	*36f*	0.155	0.9724(9)	0.7076(8)	0.9431(2)	0.016(2)
NSSiP$_{0.5}$						
Sc	*12c*	1	0	0	0.14834(5)	0.0109(2)
P / Si	*18e*	0.8333 / 0.1667	0.2953(1)	0	0.25	0.0166(3)
O1	*36f*	1	0.1847(3)	-0.0227(3)	0.19347(9)	0.0251(7)
O2	*36f*	1	0.1919(2)	0.1716(2)	0.0873(1)	0.0180(5)
Na1	*6b*	0.64	0	0	0	0.021(2)
Na2	*18e*	0.61	0.6416(5)	0	0.25	0.016(1)
Na3	*36f*	0.145	0.982(1)	0.705(1)	0.9407(4)	0.007(2)
NSSiP$_{0.6}$						
Sc	*12c*	1	0	0	0.14831(4)	0.0108(2)
P / Si	*18e*	0.8 / 0.2	0.2942(1)	0	0.25	0.0165(3)
O1	*36f*	1	0.1898(2)	-0.0201(2)	0.19320(8)	0.0221(6)
O2	*36f*	1	0.1900(2)	0.1712(2)	0.08645(9)	0.0192(4)
Na1	*6b*	0.7	0	0	0	0.026(1)
Na2	*18e*	0.62	0.6423(3)	0	0.25	0.0110(8)
Na3	*36f*	0.14	0.983(1)	0.697(1)	0.9449(3)	0.01(2)
NSSiP$_{0.8}$						
Sc	*12c*	1	0	0	0.14823(3)	0.0098(2)
P / Si	*18e*	0.7333 / 0.2667	0.2978(1)	0	0.25	0.0129(2)
O1	*36f*	1	0.1872(2)	-0.0192(3)	0.19312(7)	0.0287(6)
O2	*36f*	1	0.1889(2)	0.1710(2)	0.08536(7)	0.0109(4)
Na1	*6b*	0.72	0	0	0	0.0090(8)
Na2	*18e*	0.67	0.6422(4)	0	0.25	0.0202(9)
Na3	*36f*	0.13	0.947(1)	0.699(1)	0.9351(4)	0.016(3)

The volumes of the ScO_6 octahedra and of the $(P,Si)O_4$ tetrahedra were calculated using the refined data from Table 4.4 and Table 4.5 and the trend is shown in Figure 4.6. An increase in the volume of $(P,Si)O_4$ tetrahedra was observed with the substitution of P with Si. This result agrees with the ionic radius of P and Si in fourfold coordination, i.e. 0.17 Å and 0.26 Å, respectively [21]. In parallel, the volume of the ScO_6 octahedra decreases with the substitution.

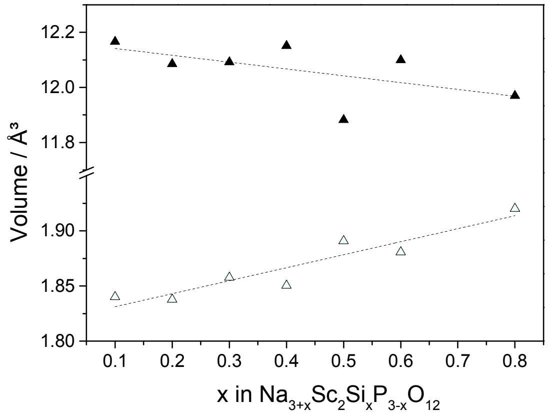

Figure 4.6: Evolution of the volume of the ScO_6 octahedra (filled symbols) and $(P,Si)O_4$ tetrahedra (open symbols) with x in $NSSiP_x$.

4.2.2. Neutron scattering results

Neutron scattering data were only gathered for $NSSiP_{0.4}$ but allowed a better insight into the Na positions thanks to measurements at 100 K in which the mobility of the Na ions is reduced. Another batch of $NSSiP_{0.4}$ powder was used for the neutron scattering measurement as for the XRD measurement and it was annealed at 1200 ℃ prior to the collection of data to remove all presence of water or CO_2. An ICP-OES analysis of this batch of powder lead to the following stoichiometry: $Na_{3.52(0.03)}Sc_2Si_{0.441(0.003)}P_{2.72(0.02)}O_{12.45}$. Almost no Na evaporation was observed for this batch and the achieved Na concentration is close to the expected one. This result highlights once again the fact that the control of the Na concentration is delicate. For this batch of powder a different annealing furnace was used leading to differences in the composition.

The profile fitting was carried out using the refined structure obtained from the XRD pattern of $NSSiP_{0.4}$ but a satisfactory result was only obtained by adding the secondary monoclinic phase. For this batch of powder, the volume fractions of monoclinic / rhombohedral phases were around 60 : 40 vol. % at 300 K and 50 : 50 vol.% at 100 K with an uncertainty of 10 vol.%. This result was confirmed by XRD analysis of this powder where also 65 vol. % of monoclinic phase was obtained at room temperature.

Since the monoclinic and rhombohedral phases are very similar and only small rotation of the polyhedra induces the loss of symmetry, it is not surprising that the additional annealing step of the sample could lead to the formation of the monoclinic phase. In addition, the ordering of Na atoms and vacancies on the Na sites in the structure were discussed to be criteria for the stabilisation at room temperature of different crystal structures of $Na_3Sc_2(PO_4)_3$ single crystals [90]. The difference in Na concentration in the powders analysed via XRD and neutron diffraction could therefore explain the difference in ratios of monoclinic to rhombohedral phases and this result will be discussed further in Chapter 5.4.

The structure of the monoclinic phase was not fitted to the NSP data available in the literature but was determined by its relation to the rhombohedral phase using the transformation matrix P described in Chapter 3.2.1.

Refinements at both temperatures revealed that Si is only present in the rhombohedral phase. Since the ratio of monoclinic to rhombohderal phase is 50:50 and no additional phases are present, we used a constraint for P/Si mixing considering the nominal composition resulting to 0.8 mol of Si per formula unit and 2.2 mol of P accordingly. The Na site occupation factors were then refined leading to an almost charge-balanced formula. The Na content was fixed during the final cycle of the refinement to assure the electro-neutrality. The refinement of all positional, occupation, and thermal displacement parameters leads to the formula $Na_3Sc_2P_3O_{12}$ for the monoclinic phase and $Na_{3.8}Sc_2Si_{0.8}P_{2.2}O_{12}$ for the rhombohedral phase. These results are in accordance with the Na concentration measured with ICP-OES.

At 100 K, the Na(1) and Na(2) positions were refined with anisotropic displacement parameters showing an elongated Na(2) position which is associated with its high mobility. At this temperature no additional position for the Na was found but at 300 K, the third Wyckoff position for Na was introduced as a displacement of the Na(2) position similar to the XRD data. With higher temperature, the mobility of the Na- ions increases making a representation only with elongated Na atoms impossible, the new position is then needed. The Na(2) and Na(3) atomic positions were then refined with isotropic displacement parameters. The results of the refinement are summarized in Table 4.6, Table 4.8 and Table 4.9.

Table 4.6: Crystallographic and structural data of both phases in the $NSSiP_{0.4}$ sample determined from neutron diffraction patterns. The values at 300 K are shown in black, those at 100K in blue.

Phase	$Na_{3.8}Sc_2Si_{0.8}P_{2.2}O_{12}$	$Na_3Sc_2P_3O_{12}$
Formula weight / g·mol^{-1}	459.9	443.8
Crystal system	rhombohedral	monoclinic
Space group, *Z*	$R\overline{3}c$, 6	C2/c, 4
a / Å	8.9884 8.9836	15.5412 15.5489
b / Å		8.9783 8.9819
c / Å	21.9922 22.2313	9.0330 9.0674
β / °		125.14 124.73
V / Å^3	1538.7 1553.8	1030.7 1040.7
$r_{c.}$ / g·cm^{-3}	2.9779 2.9489	2.8600 2.8325
TOF range / µs	9716 - 140000	
Refinement method	full matrix least square against F²	
Data points / number of parameters	2861 / 78 2861 / 77	
R_p / R_{wp} / GOF (all data)[a]	6.20 / 4.07 / 4.76 5.95 / 3.71 / 4.34	

Using the matrix P mentioned in Chapter 3.2.1 for the transformation from rhombohedral to monoclinic phase, one can calculate the equivalent monoclinic lattice parameters of the rhombohedral phase. For the structures at 300 K, the monoclinic secondary phase has very similar lattice parameters as seen in Table 4.7. In addition, the framework of the two structures is also very similar; the atomic positions differ less than 0.3 Å (for the Na positions), the main difference is the splitting of the Wyckoff positions for P and Na atoms due to lowering the symmetry from $R\overline{3}c$ to $C2/c$.

Table 4.7: Refined lattice parameters of the monoclinic secondary phase compared to the rhombohedral phase calculated as its monoclinic equivalent for NSSiP$_{0.4}$ at 300 K. The lattice parameters of refined pure phase NSP and from Collin et al. [90] are reminded as comparison.

	a / Å	b / Å	c / Å	β / °
Monoclinic secondary phase	15.549	8.982	9.067	124.73
Rhombohedral phase (monoclinic equivalent)	15.566	8.987	9.046	125.00
Lattice parameters refined by Collin et al. [90]	15.404	9.103	8.919	123.53
Lattice parameters refined in this work	15.428	9.091	8.953	123.56

Even if no Si was detected in the monoclinic phase, its lattice parameters are higher than the ones of the pure phase NSP reminded in Table 4.7 probably explaining the high conductivity of the materials despite the presence of two phases, as it will be discussed further in Chapter 5.4.

The refined patterns at 300 K and 100 K are shown in Figure 4.7.

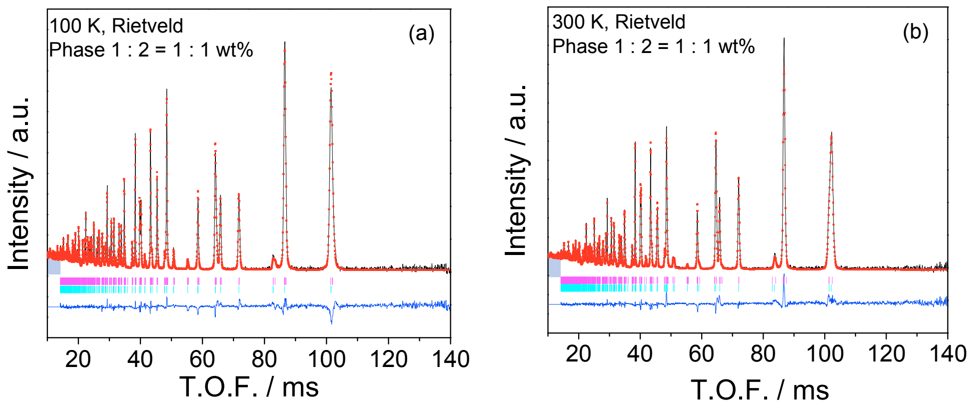

Figure 4.7: Time-of-flight powder neutron Rietveld refinement patterns for NSSP$_{0.4}$ (a) at 100 K and (b) at 300 K. The calculated data are drawn as red dots, the observed data as a black line and the difference between them is plotted in blue at the bottom. Pink and blue vertical markers below the diffraction patterns indicate the positions of the Bragg reflections of the rhombohedral and monoclinic phases, respectively.

4.2.1. Raman spectroscopy results

The different vibration modes of the samples are analysed with Raman spectroscopy. The vibrational spectra of rhombohedral and monoclinic $Na_3Sc_2(PO_4)_3$ were analysed by Collin et al. [186], giving good comparison to understand the results on the NSSiP$_x$ materials presented in Figure 4.8.

The Raman spectra present 3 regions:

- Around 1050 cm^{-1} corresponding to the valence vibration of the P-O bonds (ν_1 and ν_3 vibration).
- Between 700 and 400 cm^{-1} corresponding to the deformation vibration of the O-P-O angles (ν_2 and ν_4 vibration).
- The low wavenumber region corresponding to the external and lattice vibrations including Sc^{3+} and Na^{+} in their octahedral positions [187, 188].

Table 4.8: Positional and isotropic displacement parameter [Å^2] of the rhombohedral phase in NSSiP$_{0.4}$ (standard deviations are in brackets). The values at 300 K are shown in black, at 100K in blue.

Atom	Wyckoff position	Occupancy	x	y	z	U_{iso}
Rhombohedral $Na_{3.8}Sc_2Si_{0.8}P_{2.2}O_{12}$						
Sc	*12c*	1	0	0	0.1480(3)	0.0037(10)
		1	0	0	0.1482(4)	
P / Si	*18e*	0.733 / 0.267	0.294(2)	0	0.25	0.003(2)
		0.733 / 0.267	0.293(2)	0	0.25	
O1	*36f*	1	0.193(2)	-0.0185(17)	0.1921(5)	0.015(2)
		1	0.188(2)	-0.022(2)	0.1936(6)	0.029(4)
O2	*36f*	1	0.1884(14)	0.1717(14)	0.0852(5)	0.0082(17)
		1	0.1915(19)	0.1717(19)	0.0878(5)	0.017(3)
Na1	*6b*	0.8	0	0	0	
		0.7	0	0	0	
Na2	*18e*	1	0.606(4)	0	0.25	
		0.62	0.636(5)	0	0.25	0.015(8)
Na3	*36f*	0.2067	0.985(12)	0.690(11)	0.943(4)	0.015(8)

Anisotropic displacement parameters

Atom	U_{11}	U_{22}	U_{33}	U_{12}	U_{13}	U_{23}
Sc	0.005(2)	0.005(2)	0.018(4)	0.0024(10)	0.00000	0.00000
Na1	0.010(15)	0.010(15)	0.07(5)	0.005(8)	0.00000	0.00000
	0.08(7)	0.08(7)	0.01(4)	0.04(3)	0.00000	0.00000
Na2	0.17(3)	0.05(3)	0.12(4)	0.024(13)	0.036(14)	0.07(3)

Table 4.9: Positional and isotropic displacement parameter [Å^2] of the monoclinic phase in NSSiP$_{0.4}$ (standard deviations are in brackets). The values at 300 K are shown in black, at 100K in blue.

Atom	Wyckoff position	Occupancy	x	y	z	U_{iso}
Monoclinic $Na_3Sc_2P_3O_{12}$						
Sc	*8f*	1	0.3979(19)	0.252(5)	0.4438(17)	0.0093(19)
		1	0.3996(12)	0.248(3)	0.4481(16)	0.012(2)
P1	*8f*	1	0.644(5)	0.391(7)	0.733(7)	0.013(10)
		1	0.643(2)	0.395(5)	0.737(6)	0.011(7)
P2	*4e*	1	0.25	-0.046(14)	0.75	0.02(2)
		1	0.25	-0.072(8)	0.75	0.021(12)
O1	*8f*	1	0.544(4)	0.353(7)	0.603(6)	0.016(9)
		1	0.550(2)	0.328(4)	0.589(5)	0.004(5)
O2	*8f*	1	0.567(5)	0.059(7)	0.902(8)	0.020(11)
		1	0.573(3)	0.036(6)	0.944(6)	0.030(9)
O3	8f	1	0.674(4)	0.371(7)	0.958(6)	0.019(10)
		1	0.640(4)	0.349(9)	0.897(8)	0.047(14)
O4	8f	1	0.336(4)	0.428(7)	0.241(5)	0.005(8)
		1	0.344(3)	0.434(6)	0.267(6)	0.024(9)
O5	8f	1	0.575(4)	0.142(7)	0.234(6)	0.007(8)
		1	0.578(3)	0.144(5)	0.240(7)	0.014(7)
O6	8f	1	0.755(4)	0.169(7)	0.226(5)	0.012(11)
		1	0.758(3)	0.177(5)	0.225(6)	0.011(6)
Na1	*4c*	0.61	0.25	0.25	0	0.01(2)
		0.60	0.25	0.25	0	0.04(3)
Na2	*8f*	1	0.817(6)	0.441(9)	0.218(8)	0.018(17)
		0.95	0.808(5)	0.466(9	0.205(9)	0.034(13)
Na3	*4e*	0.39	0.5	0.34(3)	0.25	0.01(2)
		0.5	0.5	0.43(3)	0.25	0.034(13)

For NSP (x = 0), the band in the high wavenumber range is split into several modes in agreement with monoclinic symmetry [186] and in accordance with the XRD results.

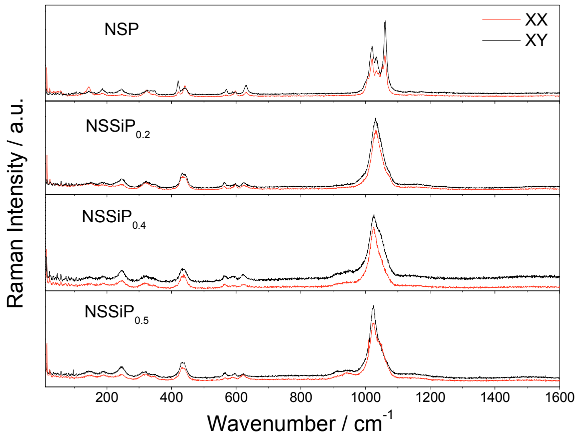

Figure 4.8: Raman spectra of NSSiP$_x$ for x= 0, 0.2, 0.4 and 0.5.

For x > 0, the band in the high wavenumber range shows a broad band with several components regrouping the ν$_3$ vibrations of SiO_4 and PO_4 in a rhombohedral symmetry. The wavenumber of the band of ν$_1$ and ν$_3$ vibration diminishes with increasing x as represented in Figure 4.9.

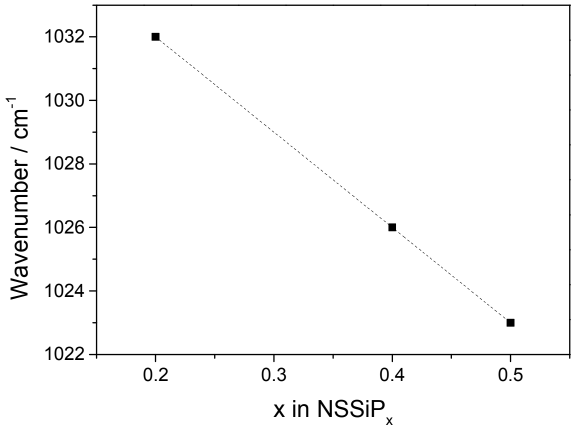

Figure 4.9: Wavenumber of the band of ν$_1$ and ν$_3$ vibration as a function of x in NSSiP$_x$.

This reflects the introduction of the Si on the P sites since the vibration of SiO_4 tetrahedra is observed at lower wavenumbers like in $Na_3Zr_2Si_2PO_{12}$ where the Raman band assigned to ν$_3$-SiO_4 and ν$_3$-PO_4 modes are observed at 920 cm^{-1} and 1030 cm^{-1}, respectively [189]. In the case of the rhombohedral structure, the splitting cannot be observed as clearly as for the monoclinic $Na_3Zr_2Si_2PO_{12}$.

4.2.2. Single crystals

To better understand the transition from the monoclinic to the rhombohedral structure and to further refine the crystallographic information about these NASICON materials, data on single crystals were gathered and the preparation of the single crystals and their investigation are presented in this chapter.

NSP single crystals

4 crystals with reasonable sizes around 400 µm as shown in Figure 4.10 were picked out of the synthesis mass and analysed by SEM, EDX and WDX.

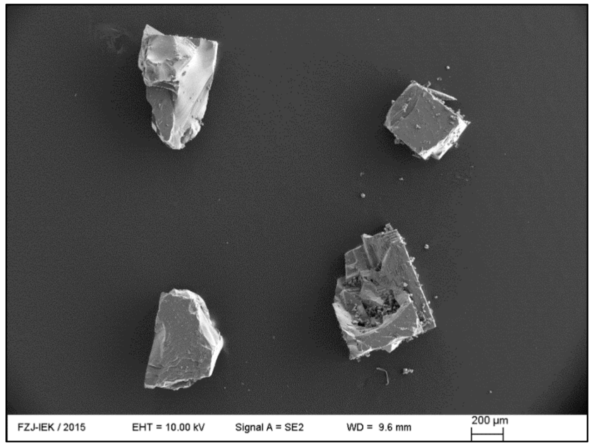

Figure 4.10: SEM picture of the 4 investigated NSP crystals.

Unfortunately, the samples were sensitive to electron beam as seen in Figure 4.11 where a square area was analysed. The area of the electron beam induces a swelling and cracking. That is why the WDX analysis gave no quantification of the observed elements because of the changing sample surface during the measurement. This observation was already discussed for β-alumina single crystals by Tietz et al. [190].

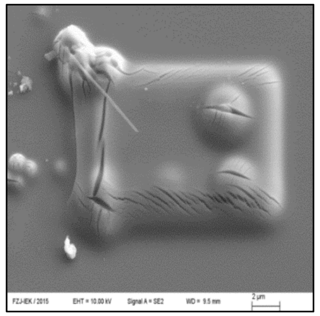

Figure 4.11: Observation with SEM of the deterioration of the NSP surface after WDX measurement.

The conditions for measuring the composition via EDX were then optimised. To do so, the stoichiometry of the material was measured with different incidence voltages. In all cases, changes in the stoichiometry indicated that the material started to decompose; a lower measuring time was used to determine the composition of the single crystals. The optimised parameters are: measurements in a square area of 10 x 10µm with 10 kV during 3 s. The obtained atomic % of each analysed atom are summarized in Table 4.10, the results were normalised to 2 mol Sc/formula unit and the amount of oxygen per formula unit was calculated to compensate the charges.

Even if a precise quantification cannot be concluded from these EDX measurements, the presence of Sc tells us that the extracted crystals are not from the flux medium $Na_4P_2O_7$ but are the desired NASICON composition.

Table 4.10: Elements quantification results via EDX for NSP single crystals.

Element	O	Na	P	Sc	composition normalized for Sc
		(atom %)			
crystal 1	60.2	16.3	14.1	9.4	$Na_{3.5}Sc_2P_{3.0}O_{12.8}$
crystal 2	58.2	16.4	15.3	10.1	$Na_{3.2}Sc_2P_{3.0}O_{11.5}$
crystal 3	60.7	15.8	14.2	9.4	$Na_{3.4}Sc_2P_{3.0}O_{12.9}$
crystal 4	58.7	17.6	14.4	9.3	$Na_{3.8}Sc_2P_{3.1}O_{12.6}$

The crystals were grinded to control their phase purity via XRD; the results are plotted in Figure 4.12.

At room temperature NSP is monoclinic [191] and the crystals obtained with the flux method preparation are also mainly monoclinic, confirmed by three reflections at 2θ = 19.5° and two reflections at 2θ = 28° [192]. Nevertheless, a rhombohedral phase is present, evidenced by the reflection at 2θ = 24°. The rhombohedral phase is stable up to 50℃ and the transition from the rhombohedral to the monoclinic phase is very easy as already realised for the batch of powder analysed with neutron scattering. Collin et al. already observed that the method of crystal growth influences their crystal structure at room temperature that can be monoclinic as for polycrystalline samples but also rhombohedral. They also introduced a superstructure of the rhombohedral cell with lattice parameters (2a, 2a, c) [186]. In their case, using the flux method, they obtained mainly rhombohedral crystals with the presence of the superstructure. Only a refinement of the XRD data on one crystal (and not on several crystals grinded) would permit to elucidate their structure.

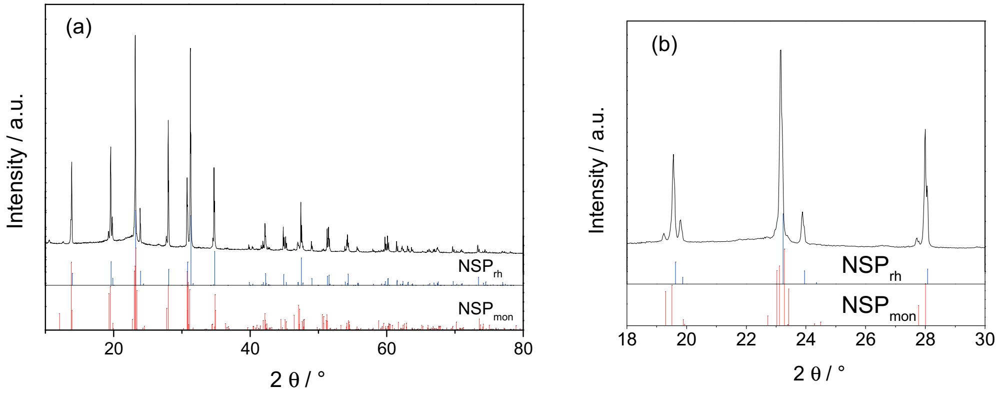

Figure 4.12: (a) XRD patterns of NSP single crystals and (b) detail of the XRD pattern between 2θ = 18° and 30° and comparison with the XRD patterns of rhombohedral and monoclinic $Na_3Sc_2(PO_4)_3$ [192] (NSP_{rh} and NSP_{mon}, respectively).

In addition, Raman measurements were made on some single crystals and the results are presented in Figure 4.13. A clear difference is observed for the band in the high wavenumber region compared to the polycrystalline NSP sample (Figure 4.8). The band is not split but a broad asymmetric peak is observed at 1038 cm^{-1} as in the rhombohedral NSP or in the above mentioned superstructure [186]. The Raman results on single crystals are consistent with the XRD results.

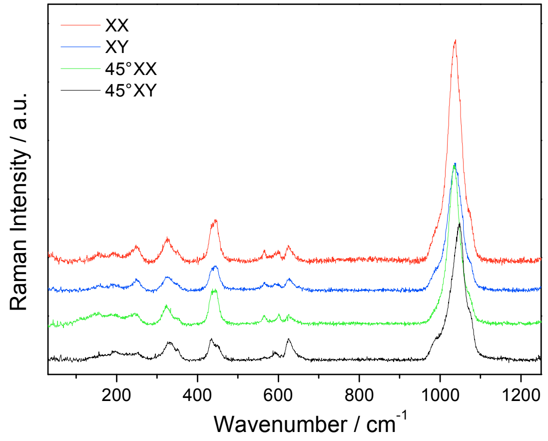

Figure 4.13: Raman spectrum of NSP single crystal

Finally, Figure 4.9 was extended in Figure 4.14 by adding the data of the single crystal NSP in the study of the wavenumber of the band of ν_1 and ν_3 vibration as a function of x in $NSSiP_x$. The data for x = 0 gathered from the single crystal match perfectly the linear behavior already observed.

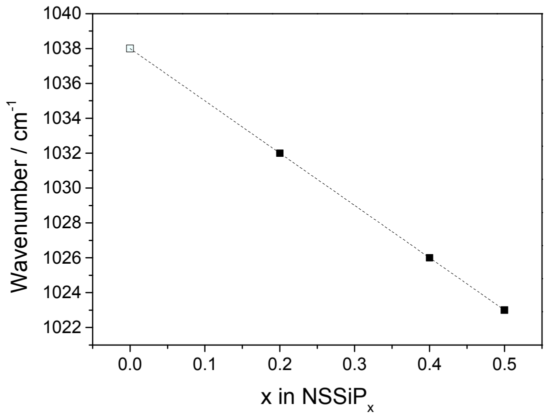

Figure 4.14: Wavenumber of the band of ν_1 and ν_3 vibration as a function of x in $NSSiP_x$ for polycrystalline samples (x > 0) and for single crystal NSP (open symbol)

$NSSiP_x$ single crystals

To date, the growth of single crystals of $NSSiP_x$ materials was not successful. The Si-source, Na_2SiO_3 was not incorporated in the obtained crystals and SiO_2 was found after each trial and no data are available for substituted NSP.

4.3. Thermal behaviour

4.3.1. High-temperature XRD

The XRD pattern of $NSSiP_{0.4}$ was measured up to 600 °C as seen in Figure 4.15. Compared to the room temperature XRD pattern, no additional reflection was observed at higher temperature displaying that no phase transition occurred for $NSSiP_{0.4}$ up to 600 °C.

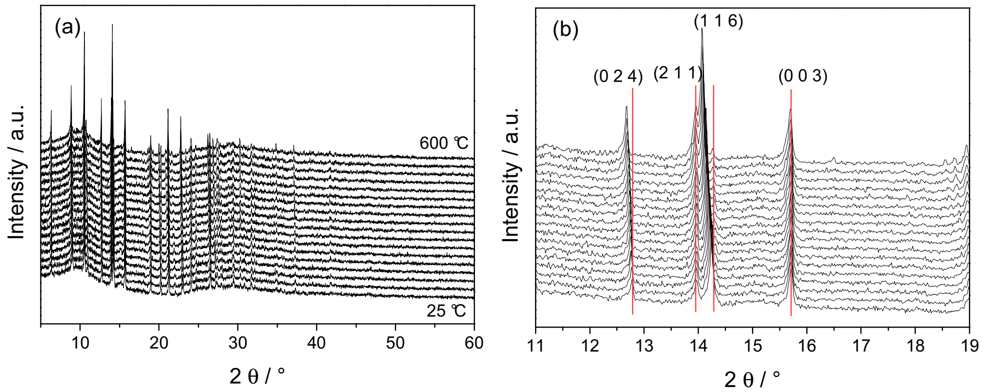

Figure 4.15: XRD pattern of $NSSiP_{0.4}$ from room temperature to 600 °C for 2 θ values between 5 and 60 ° (a) and 2 θ values between 11 and 19 ° with a representation of the reflection shift in red (b). The data are from [193].

For some reflections, a 2θ-shift to lower angles is observed during the heating. The two most strongly shifted reflections correspond to Miller indices (0 2 4) and (1 1 6), they both have a large *l* value. The reflections corresponding to (2 1 1) and (3 0 0), with a low *l* value, show almost no shift. This clearly indicates a highly anisotropic thermal expansion with large lattice changes along the *c* axis.

To verify this assumption, the lattice parameters *a* and *c* where calculated for each temperature as seen in Figure 4.16.

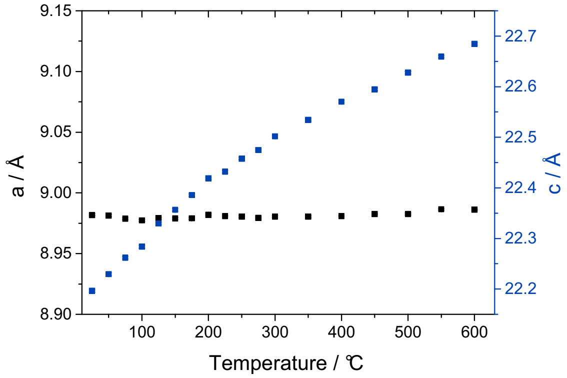

Figure 4.16: Evolution of the lattice parameters *a* and *c* with the temperature [193].

As it is typical for NASICON materials [194, 195], the coefficient of thermal expansion (*CTE*) of the lattice is anisotropic. The lattice parameter *a* experiences almost no change with increase of temperature (less than 0.4 %), whereas the lattice parameter *c* increases with increasing temperature. From room temperature to 600 ℃, the lattice parameter *c* expands up to 1.8 % which corresponds to 31 x 10^{-6} K^{-1} and the mean coefficient of thermal expansion of the material is 10 x 10^{-6} K^{-1}. This expansion is fully reversible.

The anisotropic thermal expansion will lead to large residual stresses during cooling (without thermal shock) inducing the formation of micro-cracks as it is already reported for NASICON type ceramics [196, 197].

4.3.2. Dilatometry

For an optimal polycrystalline sample, without cracks or defects, the *CTE* measured by high temperature XRD or by dilatometry should be very similar. As an example, the *CTE* of dense 8 mol% yttria-stabilised zirconia is 10.5 x 10^{-6} K^{-1} and $9.7 \cdot 10^{-6}$ K^{-1} when measured with dilatometry [198] and high-temperature XRD [199], respectively.

In the case of NASICON materials, for example $NSSiP_{0.4}$, the high anisotropy of the thermal expansion leading to the creation of cracks [196] makes the determination of the *CTE* with dilatometry controversial, as it is shown in the dilatometry curve of $NSSiP_{0.4}$ up to 1100 ℃ in Figure 4.17.

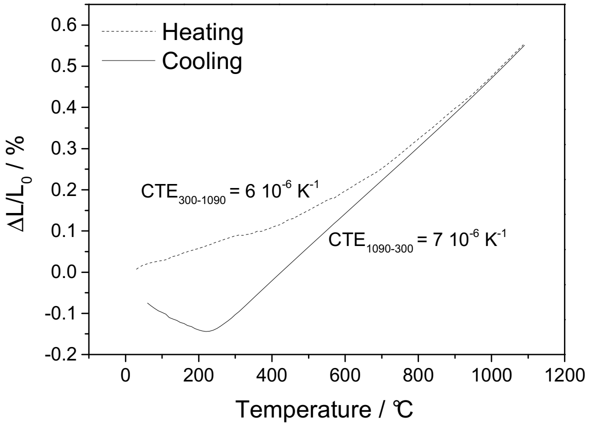

Figure 4.17: Dilatometry curves of $NSSiP_{0.4}$ during heating up to 1100 ℃ and cooling down to room temperature with 3 ℃ min^{-1}.

A hysteresis is observed during the heating and the cooling of the sample and the heating curve is not linear as expected from Equation 37. The *CTE* was therefore determined only from or down to 300 ℃ were the linearity of the data allowed it. The *CTE* values given in Figure 4.17 are in good agreement with the one calculated from the XRD data.

In her PhD thesis, S. Galal Yousef discussed the origin of micro-cracks in materials with anisotropic thermal expansion [200] and the *CTE* curve in Figure 4.17 is typical for this kind of behaviour. The following explanation is proposed: during the heating, the present micro-cracks that appeared during cooling of the sintering programme gradually disappear and the volume expansion is smaller than for a crack-free material since the volume changes are compensated by the closing of the cracks. During the cooling, the behavior of the material at high temperature is similar to an undamaged material until the cracks appear leading to an expansion of the sample in spite of decreasing temperature.

For materials with high anisotropic thermal expansion, there is a critical grain size below which the formation of micro-cracks can be avoided. It is calculated as:

$$G_{crit} = Q \frac{G_{gb}}{E\ (\Delta\alpha\Delta T)^2} \qquad \text{(Equation 38)}$$

where Q is a constant depending of the modeled grain's geometry, G_{gb} is the fracture surface energy, E is the Young's modulus, ΔT the given temperature window in which $\Delta\alpha$ is the difference between the larger and the mean coefficient of thermal expansion of the material [201]. Using the high-temperature XRD data, one can calculate $\Delta\alpha = 2.1 \times 10^{-5}\ K^{-1}$ for $\Delta T = 575$ K. The Young's modulus of the rhombohedral $NaZr_2(PO_4)_3$ calculated by Deng et al. of 120.9 GPa can be taken as first approximation [202]. In [201], different values of Q are discussed depending of the model used to describe the formation of the crack. In addition, G_{gb} is approximated between 2 and 10 J m^{-2}.

Using the different models, G_{crit} lies between 400 nm and 4 µm.

After the second annealing step around 1300 ℃, the particle size of the powders was determined with laser diffraction. As seen in Figure 4.18 for $NSSiP_{0.5}$ as an example, the particle size distribution is bimodal and the mean diameter of the particles is 38.9 µm. The powder was milled in ethanol as described in Chapter 3.1.1 and the particle size diminished to 6.4 µm with a monomodal distribution.

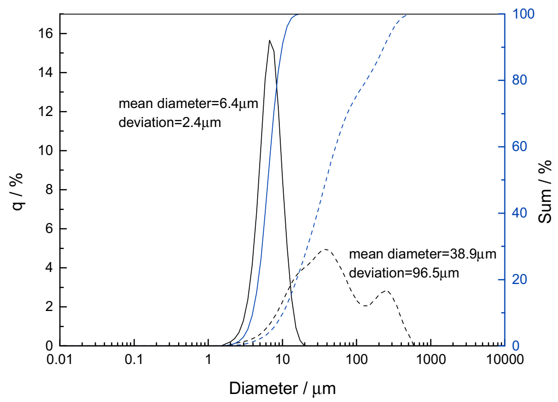

Figure 4.18: Particle size distribution before and after ball milling of $NSSiP_{0.5}$. The sample before ball milling is represented as dashed lines.

These results apply for all the compositions. After ball milling, the particle size is around 6 to 10 µm and the distribution is monomodal. This grain size of several µm is bigger than G_{crit} and the crack formation cannot be avoided. As an example, Figure 4.19 shows an SEM picture of a fractured pellet of highly densified $NSSiP_{0.4}$ (the sample was sintered at a temperature 20 ℃ higher than the optimal sintering temperature for the material). The micro-cracks of thermal origin are clearly visible.

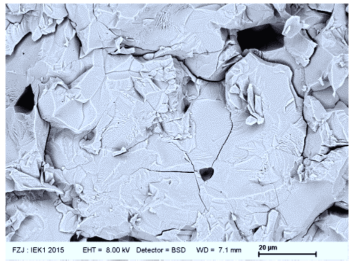

Figure 4.19: SEM picture of a fractured pellet of highly densified $NSSiP_{0.4}$ sample.

4.3.1. Sintering behaviour

Knowing that the material is sensitive to cracking, the search for the optimal temperature for its sintering was a delicate task. Especially since very little changes, like the use of a different oven or even a different position in one oven, could have a tremendous influence on the density. In addition, almost crack-free samples could only be achieved with a slow cooling rate but in all cases, the presence of these cracks could not completely be controlled and avoided.

Boehm et al. prepared $Na_3Sc_2(PO_4)_3$ samples by conventional solid state reaction and sintered samples at 1350 ℃ [99]. This temperature was taken as starting point for the sintering study and the introduction of Si in the structure lowered the sintering temperature. With the ball-milled powders with particle size of 6 to 10 µm, sintering tests at 1280 ℃ for 5h were carried out using dilatometry.

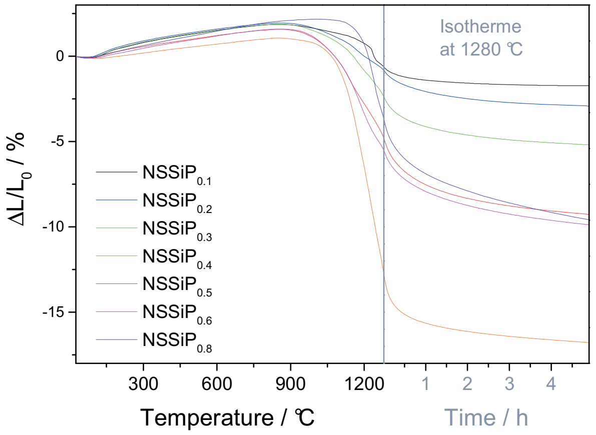

Figure 4.20: Sintering curves of the $NSSiP_x$ samples at 1280 ℃ for 5 h.

As seen in Figure 4.20, 1280 ℃ is a too low sintering temperature for all $NSSiP_x$ compounds with $x < 0.4$. It is optimal for $NSSiP_{0.4}$ and no dwell time is needed to sinter the sample. The $NSSiP_{0.5}$, $NSSiP_{0.6}$ and $NSSiP_{0.8}$ sample sinter at 1280 ℃ but the sintering lasts around 2 h and the density of the sample after sintering was lower than for other samples.

Further tests with lower temperatures did not improve the sintering of the samples $NSSiP_{0.6}$ and $NSSiP_{0.8}$ and the density listed in Table 4.11 are the mean values obtained for the different samples for the optimal sintering temperatures.

Table 4.11: Sintering temperature and achieved density for the investigated samples.

Material	Sintering temperature ℃	Theoretical density g cm^{-3}	Density g cm^{-3}	Relative density % (< 0.02 % error)
NSP	1350	2.832	2.589	91.4
$NSSiP_{0.1}$	1330	2.883	2.688	93.2
$NSSiP_{0.2}$	1320	2.890	2.743	94.9
$NSSiP_{0.3}$	1300	2.895	2.730	94.3
$NSSiP_{0.4}$	1280	2.903	2.773	95.5
$NSSiP_{0.5}$	1280	2.912	2.781	94.6
$NSSiP_{0.6}$	1280	2.921	2.567	91.6
$NSSiP_{0.8}$	1280	2.952	2.602	91.0

The optimal sintered NSSiP$_{0.4}$ sample is shown as an example in Figure 4.21. The grain size was calculated by linear intercept method using “lince-Linear Intercept 2.4.2e” software (Nichtmetallisch anorganische Werkstoffe, FB11, TU Darmstadt, Germany) using a correction factor of 1.7.

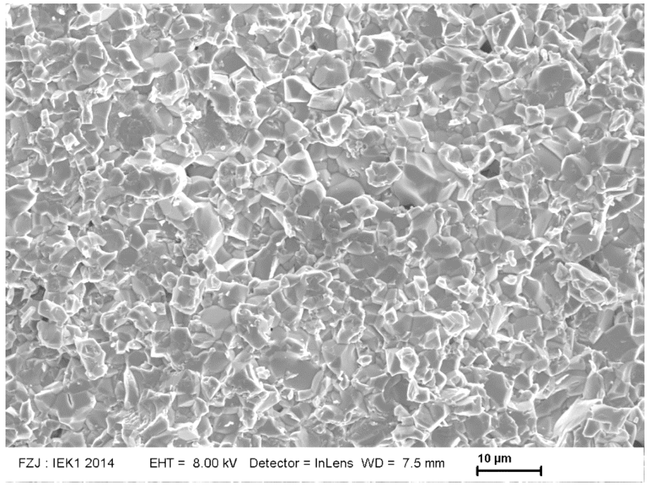

Figure 4.21: SEM picture of a fractured pellet of a NSSiP$_{0.4}$ sample.

A homogeneous microstructure was obtained with a mean grain size of 7.2 ± 1.6 µm, the sample is almost crack-free and only very few pores between the grains are observed. Isotropic grains were obtained without any preferential grain orientation within the microstructure.

Sintering tests at higher temperatures were also carried out as a try to increase the density but NSSiP$_{0.4}$ samples sintered at 1300 ℃ showed less densification with big pores between the grains and more cracks in the middle of grains. The cracked sample presented in Figure 4.19 is an example of this investigation. Figure 4.22 shows the presence of pores and cracks in this sample. In addition, small spherical pores are visible within the grains and at the grain boundaries and could be related to the gas evaporation from the sample described in Chapter 4.1 where a weight loss assimilated to sodium evaporation was observed by DTA/TG (Figure 4.1) around 1300 ℃. Higher sintering temperature will therefore not lead to higher densification but to a magnification of the defects of thermal origin.

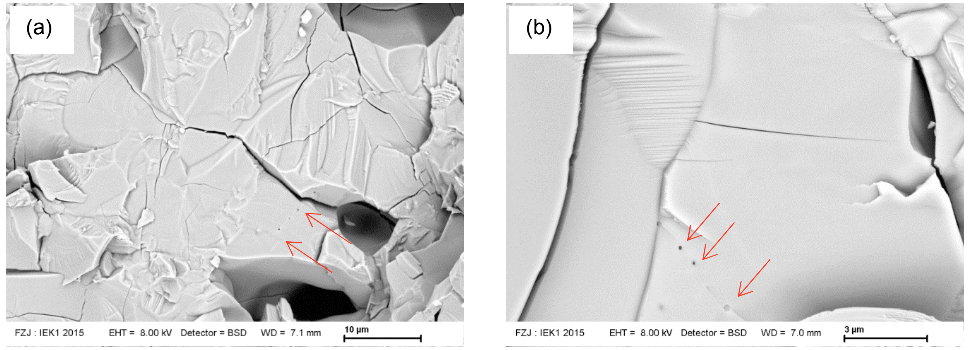

Figure 4.22: SEM picture of a fractured pellet of a NSSiP$_{0.4}$ sample sintered at 1300 ℃. (a) and (b) represent different spots on the pellet at different magnifications, the position of spherical pores is indicated with arrows.

The above summarized sintering temperatures were used for the rest of this work, but for all the samples the cracking could not be completely avoided as the materials are sensitive to minor changes in the sintering conditions. The influence of the density on the properties of the materials, especially the conductivity will be described in Chapter 4.4.1.

4.4. Conductivity measurements

4.4.1. Influence of the density

The conductivity measurements were carried out on samples with density values between 91 and 96 % as listed in Table 4.11. Figure 4.23 shows the dependence of the ionic conductivity at room temperature on the density of the measured pellets of NSSiP$_{0.4}$.

For density values lower than 88 % of the theoretical density, the conductivity of the samples is 5 to 8 times lower than for samples with density values between 91 and 96 %. This is intuitively understandable since a good contact between the grains is necessary to allow the ionic motions from one grain to the next.

A scattering of the conductivity data between 4 x 10^{-4} to 8 x 10^{-4} S cm^{-1} is observed for samples with densities between 91 to 96 % and no clear trend was obtained. The varying conductivities are probably also related to the already mentioned micro-cracks as it is difficult to prevent their appearance even with slow cooling rates after the sintering of the samples.

In conclusion, since the measured pellets have density between 91 and 96 %, the scattering of conductivity data for one composition is expected to come from the presence of cracks in the sample and not so much from the density differences.

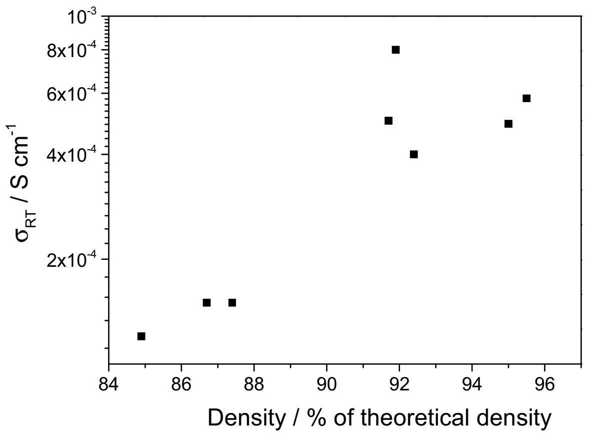

Figure 4.23: Conductivity of NSSiP$_{0.4}$ samples as a function of their density.

4.4.2. Influence of the Na concentration

It was mentioned above that the studied materials present a deficiency in Na content compared to the nominal stoichiometry. NSSiP$_{0.4}$ was synthesized with variable contents of Na and the conductivity of the obtained pellets was measured to verify which Na content leads to the highest conductivity. To do so, a defined deficiency (2, 5 and 10 %) or excess (5, 10, 15 and 20 %) of the sodium source was weighted during the preparation of the powders. The purity of the obtained powders was controlled by XRD as shown in Figure 4.24. For an excess of 10, 15 and 20 % of the weighted Na source, impurity phases of Na_3PO_4 and Sc_2O_3 are detectable. The other samples show a better phase purity.

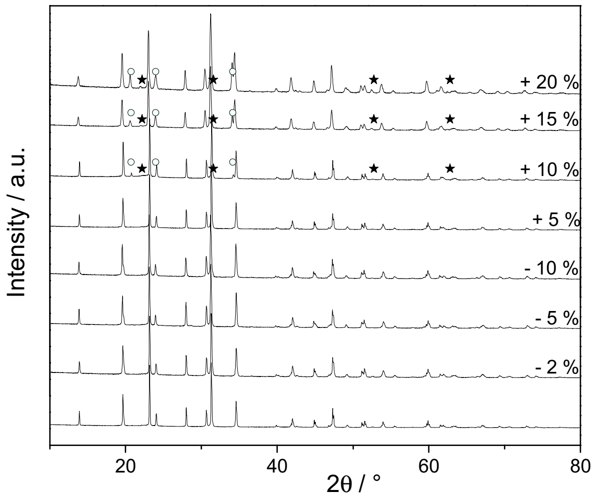

Figure 4.24: XRD pattern of the $NSSiP_{0.4}$ samples prepared with the indicated excess or deficiency of Na compared to the stoichiometric amount (lowest pattern). The open circles and filled stars represent Na_3PO_4 and Sc_2O_3, respectively.

The Na concentration of the samples was measured by ICP-OES and its influence on the conductivity of dense pellets as defined above is shown in Figure 4.25.

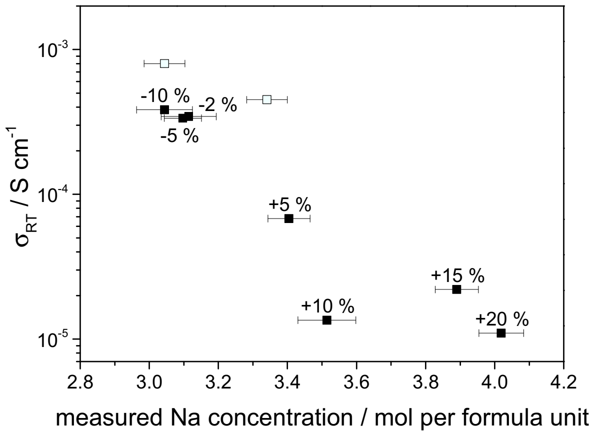

Figure 4.25: Conductivity values of $NSSiP_{0.4}$ samples against their Na concentration. The samples were prepared with the indicated excess or deficiency of Na (filled symbols) compared to the stoichiometric amount (open symbols).

The conductivity decreases with increasing Na content per formula unit, so that the samples synthesized with an excess of Na have conductivity values one order of magnitude lower as the other samples. The presence of the secondary phases probably also contribute to the lowest conductivity of the samples. For the samples with deficiency of Na content and the samples prepared with a stoichiometric amount of the Na source, the conductivity values lie in the same range and the highest conductivity is obtained when the Na concentration is around 10 % less than the stoichiometric amount. In addition, it is noticeable that the concentration of Na is not well controlled due to the Na evaporation. Nevertheless, the samples prepared with the stoichiometric amount of the Na source show the highest conductivity.

4.4.3. Room temperature conductivity

For the pellets of NSSiP$_x$ with $0.1 \leq x \leq 0.8$ with density values listed in Table 4.11 and the concentration of Na listed in Table 4.1 the impedance spectra at room temperature are shown in Figure 4.26.

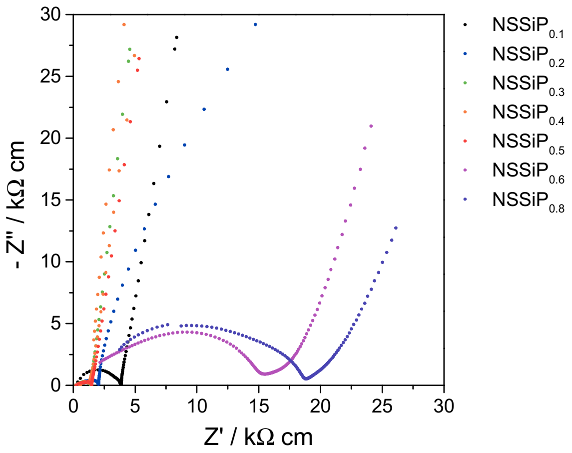

Figure 4.26: Impedance spectra of NSSiP$_x$ at room temperature. The conductivity values have been normalised to the pellets size.

The impedance spectra show a broad arc at high frequency values and a spike at lower frequencies. At least two components (bulk resistance and grain boundary resistance) can be used to simulate the broad arc. For some samples, a second process associated with the grain boundaries is observed, probably a space charge layer resistance as described by Norby et al. [203].

As one example in the solid solution, the fitting of the impedance spectra for NSSiP$_{0.4}$ is represented in Figure 4.27 and the value of resistances and capacitances (defined in Equation 28 and Equation 29) used for the fitting are summarised in Table 4.12.

Table 4.12: Fitted data of impedance spectra of NSSiP$_{0.4}$ shown in Figure 4.27. The capacitance values are calculated according to Equation 29.

R / Ω	**C_{CPE} / Ω^{-1} s^n**	**Exponent *n***	**C / F**
$R_1 = 254$	$C_{CPE1} = 2 \times 10^{-7}$	$n_1 = 0.53$	3.1×10^{-11}
$R_2 = 289$	$C_{CPE2} = 7 \times 10^{-7}$	$n_2 = 0.85$	1.5×10^{-7}
$R_3 = 1.6 \times 10^{12}$	$C_{CPE3} = 2 \times 10^{-5}$	$n_3 = 0.85$	4.5×10^{-4}

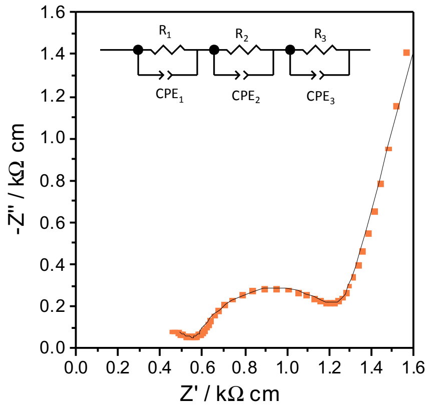

Figure 4.27: Impedance spectra of an $NSSiP_{0.4}$ sample at 30 ℃. The fitted parameters of the equivalent circuits shown here are listed in Table 4.12.

Three different elements are used for the fitting: the bulk resistance, the grain boundary resistance and the interface between the sample and the electrode and the very high value of resistance for R_3 corresponds to the blocking of the mobile ions at the electrode. This value of resistance does not represent the motion of the Na-ions in the sample and is therefore not taken into account in the calculation of the total conductivity.

Since the interpretation of the high frequency phenomena stays ambiguous only the total resistance, R_{Total}, as a sum of bulk and grain boundary resistances was deduced from the intercept of the low-frequency arc on the Z' axis. The conductivity was then calculated according to Equation 31.

The total conductivity values of $NSSiP_x$ for $0 \leq x \leq 0.8$ are summarized in Figure 4.28.

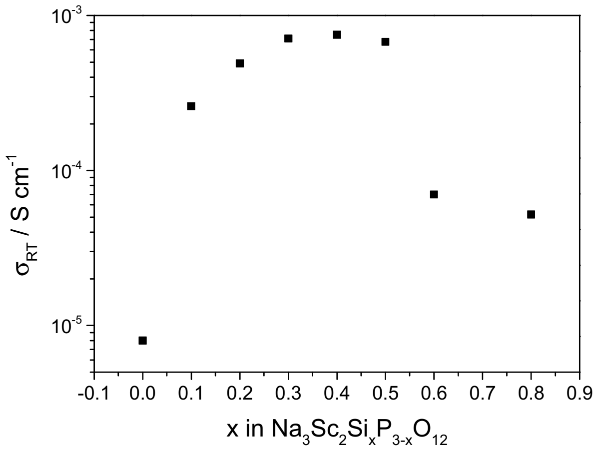

Figure 4.28: Evolution of the total conductivity at room temperature with x in $NSSiP_x$.

The conductivity increases with the substitution of P with Si and the conductivity values for $0.3 \leq x \leq 0.5$ are in the same range, around 7×10^{-4} S cm^{-1}, which places the materials among the 10 best NASICON sodium ionic conductors to date. For $x > 0.5$, the conductivity drops in correlation with the decreasing amount of Na vacancies as well as the structural parameters as described hereafter. The conductivity of $NSSiP_{0.6}$ and $NSSiP_{0.8}$ are one order of magnitude lower than for $x < 0.5$, around 4×10^{-5} S cm^{-1}.

4.4.4. Influence of the storage conditions on the impedance measurements at high temperature

The following results are described in [204]. The conductivity of NSSiP$_x$ pellets stored in ambient air was measured up to 400 ℃. From room temperature up to 120 ℃, the impedance spectra are similar to that at room temperature (see Figure 4.26). For temperatures above 120 ℃, only a straight line was observed and the total resistance, R_{Total}, as a sum of bulk and grain boundary resistances was deduced from the intercept of the straight line on the *Z'* axis, since the contribution of both phenomenon cannot be distinguished (that is why no normalised capacitance values were extrapolated from the fitting). As an example the impedance spectra of an NSSiP$_{0.4}$ sample recorded at 250, 300, 350 and 400 ℃ is shown in Figure 4.29 and the fitted parameters of the equivalent circuits are listed in Table 4.13. At high frequency values the inductance of the wires is visible when Z'' has positive values in the impedance spectrum. This happens at high temperature when the effect of the inductance of the wires stops being negligible, it could be minimized by shortening the cables. An inductor is therefore added to the equivalent circuit composed of the total resistance of the sample and to the capacitance of the blocking electrodes. The resulting Arrhenius plot is shown in Figure 4.30a.

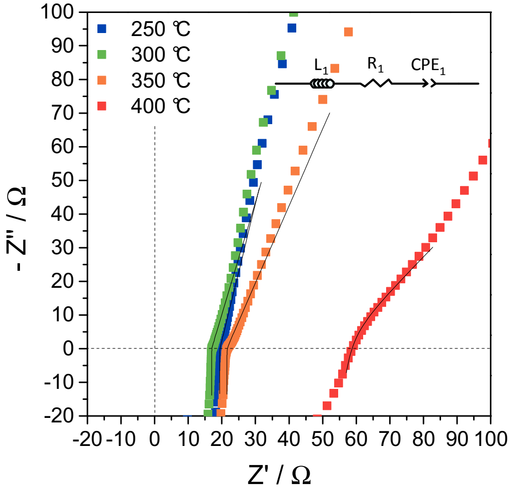

Figure 4.29: Impedance spectra of NSSiP$_{0.4}$ at 250, 300, 350 and 400 ℃. The fitted parameters of the equivalent circuits shown here are listed in Table 4.13.

Table 4.13: Fitted data of impedance spectra of NSSiP$_{0.4}$ shown in Figure 4.29.

T / ℃	L_1 / · 10^{-7} H	R_1 / Ω	C_{CPE1} / ·10^{-5} Ω^{-1} s^n	Exponent *n*
250	4.6	19.4	5.55	0.84
300	4.8	17.0	6.57	0.81
350	4.7	21.5	7.58	0.74
400	4.0	52.7	2.82	0.50

For a solid electrolyte, it is expected that the resistance decreases and therefore the conductivity increases with increasing temperature but between 300 ℃ and 400 ℃ a drastic loss of conductivity (or a gain of resistance) is observed (Figure 4.29, Table 4.13). A linear behavior is observed during the cooling of the sample but the loss of conductivity remains: before the measurement, the conductivity at room temperature was $\sigma_{25\,℃,\mathrm{before}}$ = 5.0 ×10^{-4} S/cm, after the measurement, the conductivity was $\sigma_{30\,℃,\mathrm{after}}$ = 2.6 ×10^{-5} S cm^{-1} (Figure 4.30a).

Figure 4.30b shows the Arrhenius plot for the total conductivity of a sample stored in Ar. No loss of conductivity during the measurement is observed and comparable conductivity values before ($\sigma_{20\,℃,\mathrm{before}}$ = 4.7 ×10^{-4} S cm^{-1}) and after ($\sigma_{25\,℃,\mathrm{after}}$ = 7.5 ×10^{-4} S cm^{-1}) measurement are obtained.

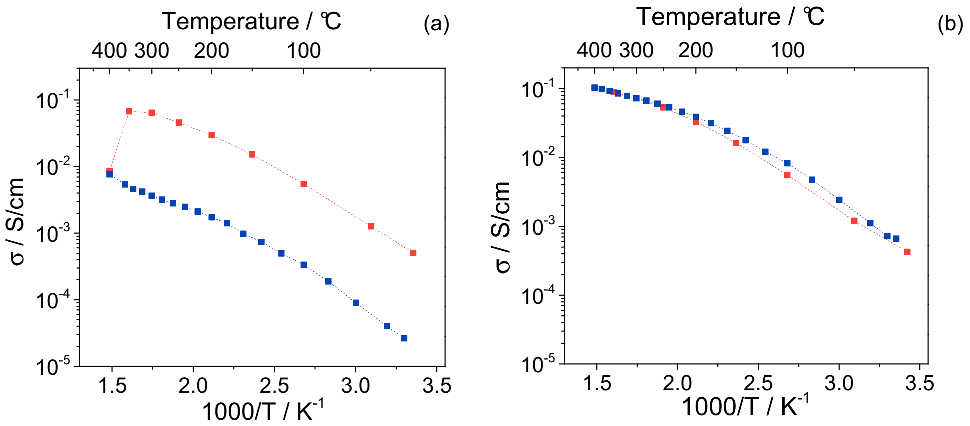

Figure 4.30: Arrhenius plot of total conductivity measured during heating (red symbols) and cooling (blue symbols) of $\mathrm{NSSiP}_{0.4}$ stored (a) in air and (b) in argon.

Comparing both Arrhenius plots, the conductivity value at room temperature are similar before heating up both samples which means that the conductivity is not influenced by the storage conditions. This is in agreement with the work of Fuentes et al. [205] which confirms the absence of proton conduction in hydrated NASICON samples.

The activation energy for the bulk conductivity was determined from ^{23}Na relaxation NMR measurements for two $\mathrm{NSSiP}_{0.4}$ samples, one stored in air, one stored in argon, as shown in Figure 4.31.

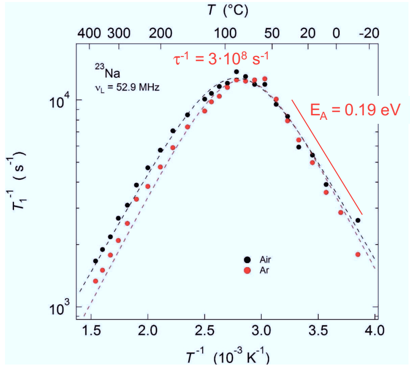

Figure 4.31: Relaxation NMR results for $\mathrm{NSSiP}_{0.4}$ samples stored in air (black symbols) and in argon (red symbols), from [193].

For both samples, the obtained activation energy values are similar (0.191 ± 0.004 eV and 0.205 ± 0.005 eV for the sample stored in argon and in air, respectively). During this measurement, only the bulk conductivity is detected indicated by the low values of activation energy. In addition, no substantial differences can be seen between both samples even at 400 °C, indicating that the reaction occurring between the sample and the water and/or CO_2 in air happens at the grain boundary level.

DSC/TG measurements coupled with mass spectrometer were carried out on an $NSSiP_{0.4}$ powder sample stored in air (Figure 4.32).

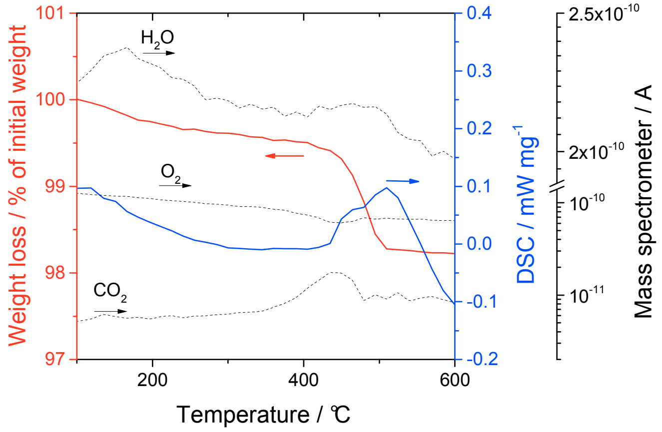

Figure 4.32: TG (red curve) and DSC (blue curve) up to 600 °C of a $NSSiP_{0.4}$ sample stored in air. Mass spectrometer signals are shown as black dotted curves: masses 18 (H_2O), 32 (O_2) and 44 (CO_2).

In this graph, the scale for the mass spectrometer is divided in two parts with different scaling to be able to visualize the peaks in the signal of water (mass 18). As a matter of fact, the dry argon used during the measurement contains at least 1 ppm of water which makes the detection of the small amount of additional water from the sample difficult.

A weight loss of 0.4 % of the original weight is observed around 100-200 °C and it is associated with a peak in the mass spectrometer for the water signal. A small amount of water at the surface of the sample is evaporated.

Starting from 380 °C, the sample experiences a more significant weight loss (1.3 % of the original weight) associated to a loss of water and CO_2 at 470 °C. The sample stored in argon was stable up to 600 °C. This observation fits to the results observed during the conductivity measurements.

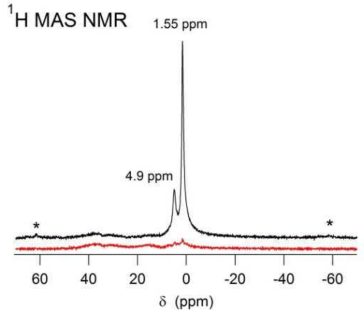

Figure 4.33: ^1H MAS-NMR spectra for $NSSiP_{0.4}$ samples stored in argon (red line) and in air (black line).

^1H MAS NMR measurements were also carried out on both samples (Figure 4.33) and a clear difference can be observed. Two peaks can be seen in the sample stored in air, one at 4.9 ppm belonging to molecular H_2O and one at 1.55 ppm belonging to OH-group.

The reactivity of the NASICON materials with H_2O and CO_2 is now confirmed but it has no influence on the conductivity measurements at room temperature. A loss of conductivity during heating of the hydrated sample is due to a loss of contact between the sample and the gold electrodes used for the conductivity measurement as it is shown in Figure 4.34.

The surfaces of the gold electrode on an $NSSiP_{0.4}$ sample stored in air and in argon after annealing at 500 °C show enormous differences already visible with the naked eye. The gold layer on the sample stored in air seems paler than the one on the sample stored in argon. Taking a closer look with the SEM, it is clear that the gold layer almost disappeared from the sample stored in ambient air whereas the sample stored in argon still displays a correct coverage except at the grain boundaries [204].

One can conclude from this study that a new recommendation for handling of NASICON-type materials is needed to prepare samples for impedance spectroscopy measurements: samples require storage in an Ar-filled glove box or in a dry environment. Except mentioned otherwise, all samples in the following were handled accordingly.

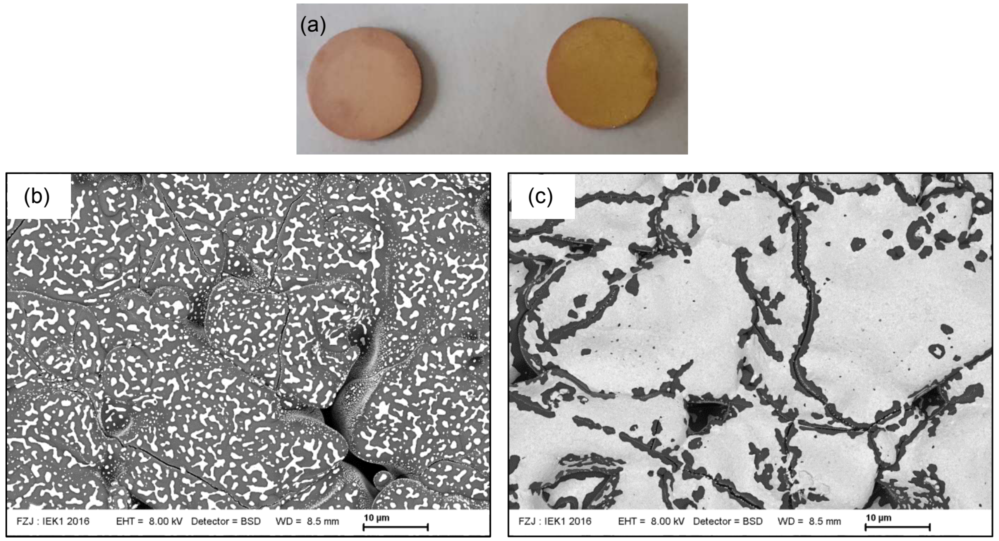

Figure 4.34: (a) Picture of the surface of the gold electrode on $NSSiP_{0.4}$ samples stored in ambient air (left-hand pellet) and in argon (right-hand pellet) after annealing at 500 °C and SEM pictures of the samples stored in ambient air (b) and in argon (c).

4.4.5. Activation energy

The conductivity of similar $NSSiP_x$ samples stored in an Ar-filled glove box was measured up to 400 °C. As mentioned above, up to 120 °C, the impedance spectra are similar to Figure 4.26 and for temperatures above 120 °C they are similar to the spectra at 300 °C for all the $NSSiP_x$ materials (Figure 4.35).

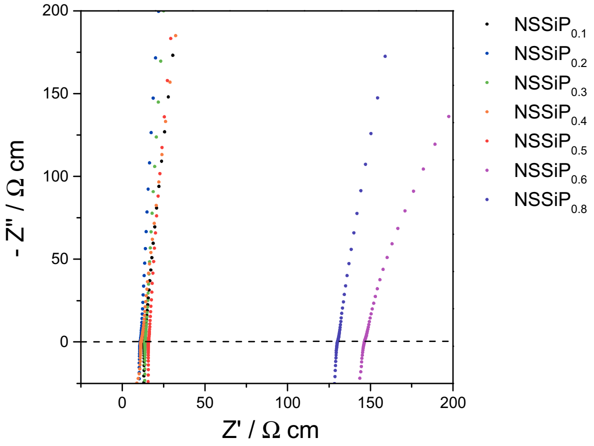

Figure 4.35: Impedance spectra of $NSSiP_x$ at 300 ℃. The conductivity values have been normalized to the pellets size.

The total conductivity was obtained from Equation 30 using the resistances in the equivalent circuits shown in Figure 4.27 (for low-temperature impedance spectra) and Figure 4.35 (for high-temperature impedance spectra). The resulting total conductivity values at 300 ℃ are summarized in Figure 4.36.

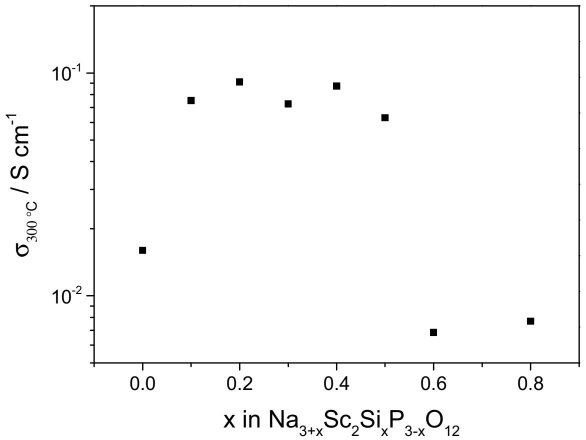

Figure 4.36: Dependence of the total conductivity at 300 ℃ on x in $NSSiP_x$.

The correlation of conductivity at 300 ℃ with x in $NSSiP_x$ is similar to what is observed at room temperature: the conductivity increases with increases x and drops when $x > 0.5$. The conductivity values at 300 ℃ for $0.1 \leq x \leq 0.5$ are in the same range and the difference between the materials is less pronounced as at room temperature.

For the $NSSiP_x$ materials the measurements from room temperature to 400 ℃ result in the Arrhenius plot of total conductivity shown in Figure 4.37.

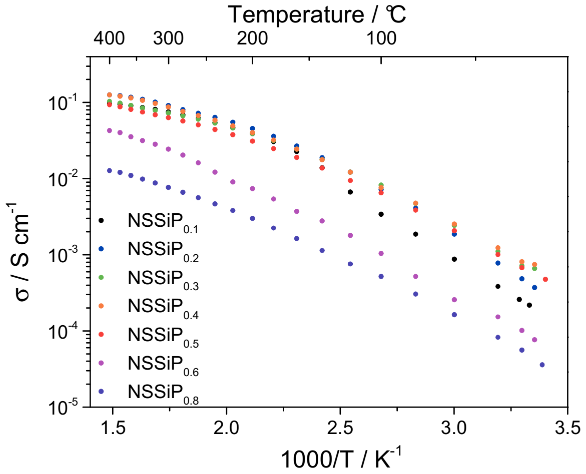

Figure 4.37: Arrhenius plot of the conductivity of NSSiP$_x$ with $0.1 \leq x \leq 0.8$ from 30 ℃ to 400 ℃.

A change in slope is observed for all compositions at around 200 ℃, but no phase transition was detected by high-temperature XRD and DSC/TG measurements (Figure 4.15 and Figure 4.32, respectively). The change in slope could be explained by the diminishing contribution of the grain boundary conductivity with increasing temperature as described for β-alumina by Hooper [79], where the activation energies of single crystals and polycrystalline samples were compared and match at high temperature. Unfortunately the data from room temperature to 400 ℃ do not allow to distinguish the bulk resistance from the grain boundary resistance. To verify this hypothesis, more data where gathered by measuring the conductivity of the materials from -30 ℃ to 30 ℃. From -30 ℃ to 0 ℃, two semi-circles are observed and can be attributed to the bulk resistance and the grain boundary resistance as shown in Figure 4.38 for NSSiP$_{0.4}$. The corresponding fitted impedance parameters are listed in Table 4.14.

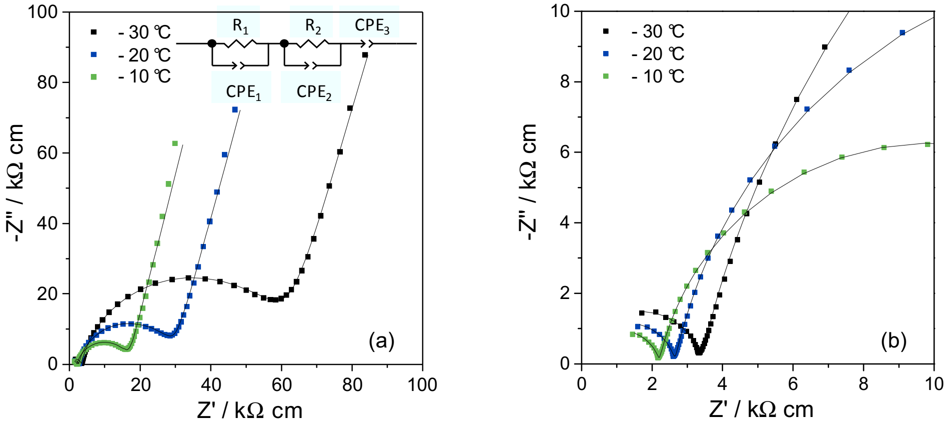

Figure 4.38: Impedance spectra of a NSSiP$_{0.4}$ sample at -30, -20 and -10 ℃ for (a) the whole frequency range and (b) the high frequency part. The fitted parameters of the equivalent circuit shown in (a) are listed in Table 4.14.

Table 4.14: Fitted data of impedance spectra of $NSSiP_{0.4}$ shown in Figure 4.38. The capacitance values are calculated according to Equation 29.

T / °C	R / Ω	C_{CPE} / Ω^{-1} s^n	Exponent *n*	C / F
- 30 °C	$R_1 = 799$	$C_{CPE1} = 2 \times 10^{-10}$	$n_1 = 0.92$	1.2×10^{-11}
	$R_2 = 13528$	$C_{CPE2} = 3 \times 10^{-7}$	$n_2 = 0.86$	2.8×10^{-8}
	$R_3 = 7.7 \times 10^{12}$	$C_{CPE3} = 1 \times 10^{-5}$	$n_3 = 0.83$	9.7×10^{-5}
- 20 °C	$R_1 = 627$	$C_{CPE1} = 3 \times 10^{-10}$	$n_1 = 0.91$	1.5×10^{-11}
	$R_2 = 6270$	$C_{CPE2} = 3 \times 10^{-7}$	$n_2 = 0.88$	3.0×10^{-8}
	$R_3 = 3.9 \times 10^{13}$	$C_{CPE3} = 1 \times 10^{-5}$	$n_3 = 0.83$	1.3×10^{-4}
- 10 °C	$R_1 = 522$	$C_{CPE1} = 3 \times 10^{-10}$	$n_1 = 0.90$	1.3×10^{-11}
	$R_2 = 3407$	$C_{CPE2} = 3 \times 10^{-7}$	$n_2 = 0.88$	2.9×10^{-8}
	$R_3 = 2.1 \times 10^{13}$	$C_{CPE3} = 1 \times 10^{-5}$	$n_3 = 0.84$	9.0×10^{-5}

The values of capacitance indicate that R_1 corresponds to the resistance of the bulk conductivity (R_{bulk}), R_2 to the resistance of grain boundary conductivity (R_{GB}) and R_3 to the blocking electrode [163]. The ratio R_{bulk} / R_{GB} increases with increasing temperature (0.06 for -30 °C, 0.1 for -20 °C and 0.16 for -10 °C in the case of $NSSiP_{0.4}$), indicating that the contribution of the grain boundary resistance diminishes with temperature increase, which also confirms the explanation for the change of slop in the Arrhenius plot in Figure 4.37.

An Arrhenius plot for the bulk conductivity was obtained at low temperature for all the $NSSiP_x$ materials as summarized in Figure 4.39. For each sample, the distinction between both semi-circles of bulk and grain boundary resistance could not be made for all measurement temperatures explaining the differences in the Arrhenius plot for the different compositions.

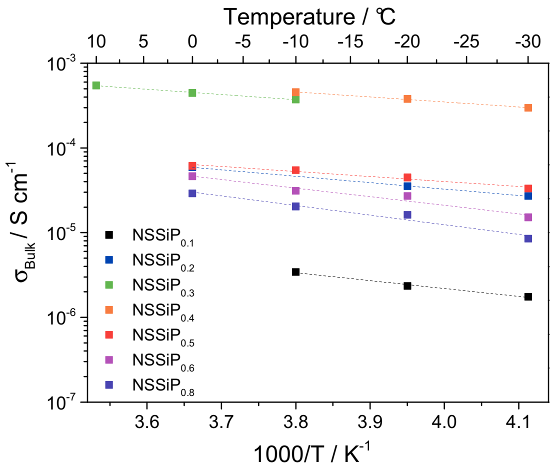

Figure 4.39: Arrhenius plot for the bulk conductivity of the $NSSiP_x$ samples.

The obtained values of bulk conductivity are in accordance with relaxation NMR measurements on $NSSiP_{0.4}$. The measured diffusion coefficient at 360 K was $D_{Na} = 6.4 \times 10^{-12}$ m² s^{-1} which corresponds to a conductivity of 4 mS cm^{-1} using the Nernst-Einstein equation:

$$D_{Na} = \sigma_{Na} \times \frac{kT}{C_{Na} \times e^2} \qquad \text{(Equation 39)}$$

where C_{Na} is the concentration of Na ions, *e* the elementary charge and *k* the Boltzmann constant.

Using the Arrhenius law, the value of bulk conductivity at 360 K can be extrapolated: $\sigma_{360\,K} = 1.6$ mS cm^{-1}. Keeping in mind the error on the determination of activation energy for the bulk conductivity, both values are in good agreement.

Using the slope of the Arrhenius plots in Figure 4.37 and Figure 4.39 and the Arrhenius law (Equation 9), the three following activation energies were calculated and are summarized in Figure 4.40:

- activation energy of total conductivity up to 200 ℃
- activation energy of total conductivity from 200 to 400 ℃
- activation energy of bulk conductivity.

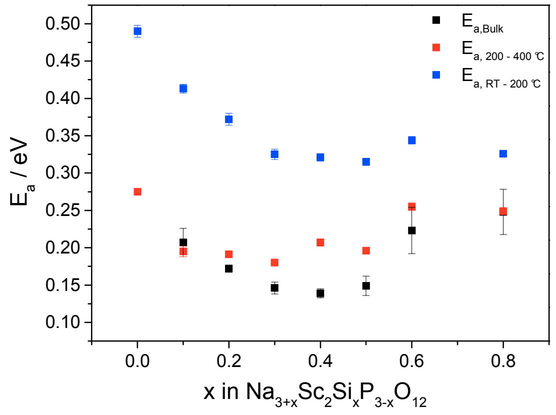

Figure 4.40: Dependence of activation energy on x in $NSSiP_x$: activation energy of the total conductivity at low temperature (blue symbols); activation energy of the total conductivity at high temperature (200-400 ℃; red symbols) and activation energy of the bulk conductivity (black symbols).

The activation energy of total conductivity at low temperature decreases with increasing x up to x = 0.3, after which the values lie in the same range. The determined values of 0.3-0.35 eV have been reported very often for highly conductive NASICON materials [7].

The activation energy of the bulk conductivity, however, is significantly smaller and the values correspond to similarly low values observed for the lithium-analogue $Li_{1+x}Al_xTi_{2-x}P_3O_{12}$ [206, 207]. It was also measured with relaxation NMR for $NSSiP_{0.4}$ as already seen in Figure 4.31. The obtained value of 0.191 ± 0.004 eV is a little bit higher than the value of 0.12 ± 0.02 eV obtained from the impedance measurements. The discrepancy can be attributed to the sometimes controversial interpretation of the impedance spectra at low temperature; nevertheless, the values are in the same range.

In addition, computational calculation applying the Nudged Elastic Band method (NEB) [177] to $NSSiP_{0.5}$ gave a value of activation energy of the bulk conductivity of 0.18 eV [183] which also is in the same range as the value of 0.14 ± 0.01 eV extrapolated from the impedance measurements. The results of the computational calculation are shown in Figure 4.41 where the x-axis represents the position of a Na(2) atom along its pathway to its equivalent position in the next unit cell along the minimum energy pathway. The two saddle-points at 0.18 eV define the energy barrier.

Both the NMR and computational investigations confirm the values of activation energy for the bulk conductivity extracted from the impedance measurements at low temperature.

For the whole solid solution, the activation energy of the bulk conductivity correlates better with the conductivity values since an increase was observed for x > 0.5. The impact of the grain boundary conductivity varies for each composition and influences the total conductivity (and accordingly the activation energy) which explains the better correlation of activation energy with conductivity for the bulk data. Finally, the activation energy at high temperature follows roughly the same trend as the activation energy of the bulk conductivity and also increases for x > 0.5 and only the end members of the series have matching activation energies as outlined by Hooper [79]. The activation energies at high temperature are lower than the data of the total conductivity at low temperature and higher than the data from bulk conductivity. This indicates that between 200 ℃ and 400 ℃ the contribution of the grain boundary conductivity is decreasing but not completely negligible. It can be expected that the activation energy of the bulk conductivity and of the total conductivity match at even higher temperatures.

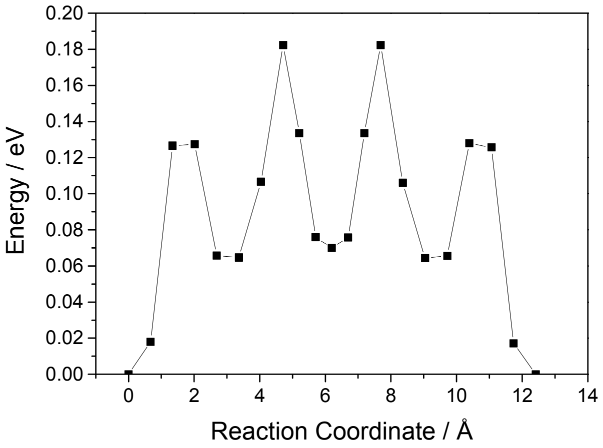

Figure 4.41: Minimum energy pathway for sodium ion transport in $NSSiP_{0.5}$ [183].

5. Discussion part 1: Study of the scandium-based solid solution

In the following chapter, the previously described results on the NSSiP$_x$ solid solution are correlated and analysed to understand the origin of high ionic conductivity for $0.3 \leq x \leq 0.5$.

5.1. Pathway for the Na conduction

Before looking in details into the crystallographic parameters that influence the conductivity, the pathway for the sodium conduction should be specifically analysed for both the rhombohedral and the monoclinic materials according to the obtained XRD and neutron data.

5.1.1. Rhombohedral NSSiP$_x$

The pathway of Na$^+$ ions in the structure has already been described in the first NASICON material by Hong et al. [10, 87] and is recalled in Chapter 2.3.2 and Figure 2.12(b).

Figure 5.1 represents a comparison of the conduction channel of alternating Na(1) and Na(2) positions in the rhombohedral NSSiP$_{0.4}$ from the refined XRD pattern and the refined neutron scattering pattern at 300 K.

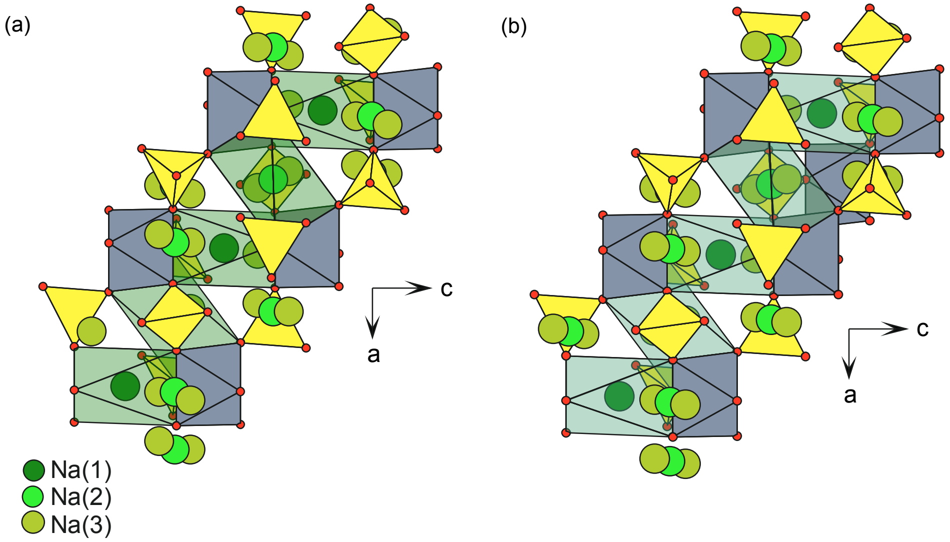

Figure 5.1: Representation of the conduction pathway in the NASICON structure along (1 $\bar{2}$ 0) using (a) the XRD data and (b) the neutron scattering data of NSSiP$_{0.4}$. The ScO$_6$ octahedra are represented in grey and the PO$_4$ tetrahedra in yellow.

Both figures look similar and the main visible difference is the position of the Na(2) and Na(3) atoms. The good agreement of both structures validates the refinement of the XRD pattern and the remaining intensity differences between the calculated pattern and the observed pattern for the XRD data in Figure 4.4 can be explained by the small deviations of the Na positions. At room temperature, the conduction occurs from the Na(1) position to the Na(2) or the Na(3) position so that it can be summarized Na(1) - Na(2) - Na(1) and Na(1) - Na(3) - Na(1). The hopping distance is 3.41 Å for Na(1) to Na(2) and 3.00 Å - 3.90 Å for the Na(1) to Na(3) pathway (or respectively 3.90 Å - 3.00 Å). No other pathway can be considered because the hopping distances are not favourable (< 1.9 Å or > 4 Å).

At 100 K, the displacement of the Na(2) Wyckoff position was not "visible" and the atoms were refined with an anisotropic displacement parameter leading to "elongated" atoms as seen in Figure 5.2.

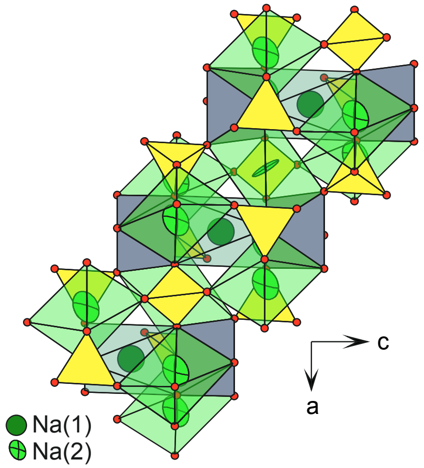

Figure 5.2: Representation of the conduction pathway in the NASICON structure along $(1\ \bar{2}\ 0)$ using the neutron scattering data of NSSiP$_{0.4}$ at 100 K. The ScO$_6$ octahedra are represented in grey and the PO$_4$ tetrahedra in yellow.

The atoms are elongated in the direction of the position of the Na(3) Wyckoff position, which means that at low temperature, the mobility is reduced but both models are in agreement. The hopping distance at 100 K is shortened to 3.32 Å. In addition at both 100 K and 300 K, one observed that the Na hopping in the structure is isotropic, the Na(1) atoms are 6-fold coordinated by Na(2) atoms resulting in a 3D conduction path.

5.1.2. Monoclinic NSP

Like in Na$_3$Zr$_2$Si$_2$PO$_{12}$, there are 3 Wyckoff positions for the Na-ions in the monoclinic structure and the conduction occurs from the Na(1) to the Na(2) position or from the Na(1) to the Na(3) position (Chapter 2.3.2, Figure 2.12 and Figure 2.14). Table 5.1 summarizes the interatomic distances between the Na atoms along both pathways at 100 K and at 300 K.

At both temperatures, the preferred pathway is from the Na(1) to the Na(3) positions since the interatomic distances are more favorable.

Table 5.1: Interatomic distances between the Wyckoff positions for the Na-ions along the pathways in the monoclinic $Na_3Sc_2(PO_4)_3$.

	Path Na(1)-Na(2)-Na(1)-Na(2)	**Path Na(1)-Na(3)-Na(1)-Na(3)**
100 K	3.28 Å - 3.28 Å - 3.28 Å -3.28 Å	3.21 Å - 3.68 Å - 3.68 Å - 3.21 Å
300 K	3.58 Å - 3.58 Å - 3.58 Å - 3.58 Å	2.98 Å - 3.81 Å - 3.81 Å - 2.98 Å

In the following, the different results obtained for the $NSSiP_x$ solid solution were correlated to get a better understanding of the two simultaneous impacts of Si substitution in NSP: a) the change in the Na content and hence the increase in charge carriers and b) the change in lattice size and hence the steric (but also electrostatic) change along the conduction paths. Both impacts influence the conductivity of the compounds.

5.2. Impact of the Na content on the conductivity

Increasing the amount of charge carriers increases the conductivity of the material as it was observed for compositions up to 3.4 moles of Na per formula unit in the nominal stoichiometry. For higher Na concentrations, the conductivity decreases due to the decreasing amount of Na vacancies. A balance between the amount of occupied and vacant Na sites is crucial for a high ionic conductivity. In $NSSiP_x$, the maximum amount of Na per formula unit is 4 mol and the highest conductivity is achieved around 3.12 mol (ICP-OES data) which represents a ratio of occupied Na sites over vacant Na sites of approximately 80/20: the conductivity increases with the amount of charge carriers but at least 20 % of the charge carrier positions have to be vacant. This result agrees with the trend observed by Vogel et al. [22] since the highest conductivities and lowest activation energies were obtained for an amount of 3.2 - 3.5 mol Na per formula unit in the serie $Na_{1+x}Hf_2Si_xP_{3-x}O_{12}$.

Not only the overall Na concentration must be in the above mentioned ratio, the occupancy of each atomic position also has to be considered. This is verified using the structure of $NSSiP_{0.4}$ from the refined neutron scattering pattern at 100 and 300 K. The occupancy of each Wyckoff position for the Na atoms in both rhombohedral and monoclinic structures present in the $NSSiP_{0.4}$ sample are reminded in Table 5.2.

Table 5.2: Occupancy of the Na positions compared to the maximum occupancy of the Wyckoff position of (a) the rhombohedral and (b) the monoclinic phase present in the $NSSiP_{0.4}$ samples analysed with neutron scattering.

(a)

	Na(1)	Na(2)	Na(3)
		mol per formula unit	
Maximum occupancy	1	3	1
300 K	0.7	1.86	1.26
100 K	0.8	3	0

(b)

	Na(1)	Na(2)	Na(3)
		mol per formula unit	
Maximum occupancy	1	2	1
300 K	0.6	1.9	0.5
100 K	0.61	2	0.39

At both temperatures, and in both phases the Na(1) position is not fully occupied. This was also verified with the XRD data for all the $NSSiP_x$ materials where for increasing x, the occupancy rises from 40 % to 72 % of maximum occupancy. The maximum conductivity is obtained for $NSSiP_{0.4}$ in which the Na(1) position was 52 % occupied.

Using the XRD data in an attempt to adapt the work of Kawai et al. on $Li_{3x}La_{0.67-x}TiO_3$ [208] to $NSSiP_x$, the evolution of conductivity was correlated to the concentration of Na^+ on the Na(1) Wyckoff position, the concentration of vacancy on the Na(1) position (named $C_{Na+ \text{ in } Na(1)}$ and $C_{V(1)}$, respectively) and the fraction of mobile charge carrier concentration *C* defined as:

$$C = \frac{C_{Na} \times C_V}{C_{Na} + C_V} \qquad \text{(Equation 40)}$$

where C_{Na} is the concentration of Na^+ and C_V the concentration of vacancies at the Na position. Data of the 30 NASICON materials with published crystallographic data [10, 22, 87, 90, 93, 96-102, 106, 107, 111-116, 121-133] were also added to this study.

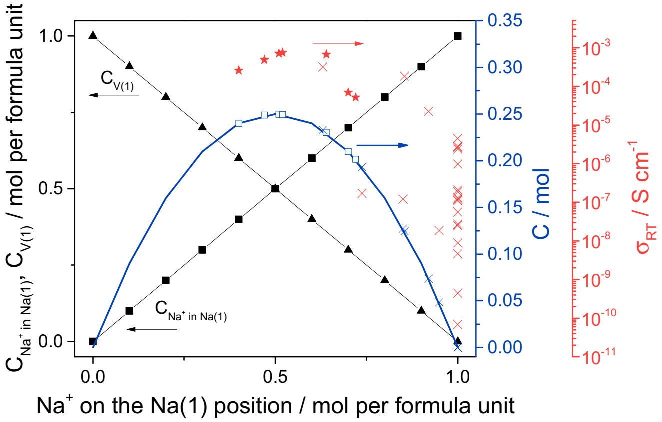

Figure 5.3: Variation of sodium ion conductivity at room temperature of $NSSiP_x$ and 30 other NASICON materials with known site occupancy [10, 22, 87, 90, 93, 96-102, 106, 107, 111-116, 121-133] as a function of sodium concentration in the Na(1) site and the concentration of vacancies on this site. The mobile charges of the experimental samples are represented as blue open squares, the literature data are represented as crosses.

For the $NSSiP_x$ solid solution, the dome-shaped behavior of the conductivity matches the dome-shaped behavior of *C* and the highest conductivity is obtain when approximately 50 % of the Na(1) position is occupied, as it was observed for the $Li_{3x}La_{0.67-x}TiO_3$ solid solution [208]. This result is verified in Figure 5.4 where $\log(\sigma_{RT})$ is linear dependent with *C.*

The conductivity of the 30 other NASICON materials added to Figure 5.3 do not follow a dome-shaped dependence of the amount of Na on the Na(1) site, especially because a lot of studied materials contain only 1 mol of Na in the formula unit and the Na(2) site is not occupied. Among all these materials a huge scattering of conductivity was observed and as it was already discussed in Chapter 2.3.4; the conductivity changes were interpreted by the significant impact of the $M^{(IV)}$ cations and maybe experimental uncertainty of the sodium content. Nevertheless, the most conductive NASICON material found in the literature have the lowest amount of Na on the Na(1) site, i.e. more specifically 63 % of Na(1) site occupancy. These observations lead to the following conclusion: the highest conductivity is obtained when the Na(1) site is approximately half occupied. This is in accordance with the expression of the pre-exponential factor directly proportional to *C(1-C)*, where *C* is the concentration of the mobile ion in one site (Equation 10). The pre exponential factor is therefore maximal if *C* = 0.5, i.e. if the position is half occupied.

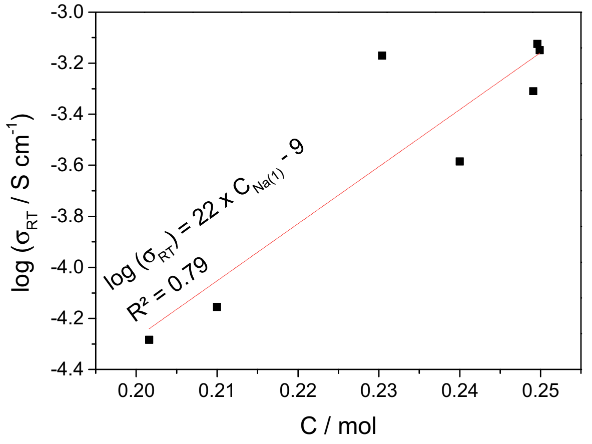

Figure 5.4: Log(σ_{RT}) as a function of the fraction of mobile charge carrier concentration *C* for the Na(1) position. The linear correlation is represented as a red line.

Going back to the neutron scattering data at 100 K, in both rhombohedral and monoclinic structures the Na(2) position is fully occupied which is not favourable for a good conductivity. In the monoclinic phase the full occupancy of the Na(2) position is a second argument to expect the conduction to occur preferentially along the pathway Na(1)-Na(3). At 300 K, the Na(2) Wyckoff position is not fully occupied anymore which probably allows a better hopping along the pathway Na(1)-Na(2).

For the rhombohedral structure, the displacement of the Na(2) position into metastable sites explains the high conductivity. The same study as in Figure 5.3 cannot be made for the sodium concentration at the Wyckoff position Na(2) since Na(3) should be taken into account. However, one can consider the Na(2) displacement defined as:

$$\frac{c_{Na(3)}}{c_{Na(2)} + c_{Na(3)}} \times 100 \qquad \text{(Equation 41)}$$

where $C_{Na(2)}$ and $C_{Na(3)}$ are the amount of Na^+ on the Na(2) and Na(3) sites, respectively.

In Figure 5.5, the Na(2) displacement is correlated to the total Na concentration in the NSSiP$_x$ materials and it is compared to their conductivity.

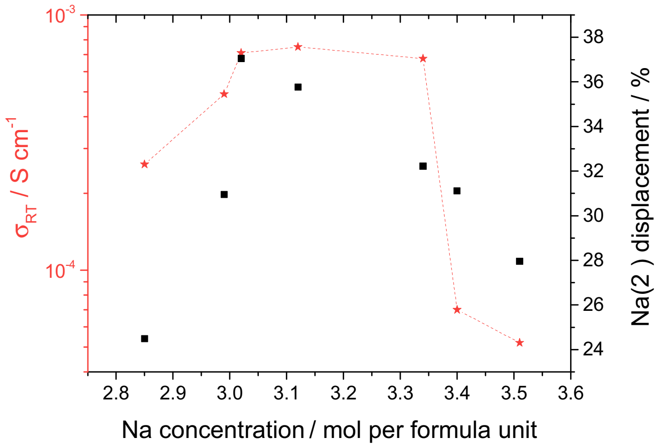

Figure 5.5: Na(2) displacement as a function of the analytical Na concentration in the NSSiP$_x$ materials and comparison with their conductivity.

A fairly good correlation is observed: the $NSSiP_x$ materials with the highest displacement of the Na(2) site have the highest conductivity values.

At this point, it is not possible to differentiate if these results can be defined as criteria for high conductivity or if they are observed because of the high conductivity of the materials. As a matter of fact, the high displacement of the Na(2) position is concluded from the high electronic density around the Na(2) position caused by their constant motion. In addition, half occupancy of the Na(1) site is an averaging value for the highly mobile Na^+. For materials with no Na motion, the Na(1) position appears fully occupied because the ions do not move from this position.

Altogether, since the Na occupancy in each Na site in the structure cannot be controlled by the synthesis route, these results cannot be used to help designing better conductive NASICON materials in the sense that no defined site occupation can be adjusted. However, the criterion to remember is the total Na concentration of 3.2-3.5 mol Na per formula unit already evidenced from comparing literature data [20], which is a good starting point achieving high ionic conductivities.

5.3. Correlation between the lattice size and the conductivity

In the following study, the correlations are made with the crystallographic data from the rhombohedral NASICON materials gathered with XRD, since neutron scattering data were only available for one composition. This leads to a larger scattering of data due to higher errors in the refinement of the atomic positions but the trends are still recognizable.

5.3.1. Na hopping distance

Since the Na^+ conduction occurs by successive hopping from the Na(1) to the Na(2) Wyckoff positions, the impact of the distance between these positions determined from the room temperature XRD data on the activation energy of the bulk conductivity measured between -30 and 0 ℃ was investigated. The small deviations of the distances due to the influence of thermal expansion do not change the general feature of Figure 5.6.

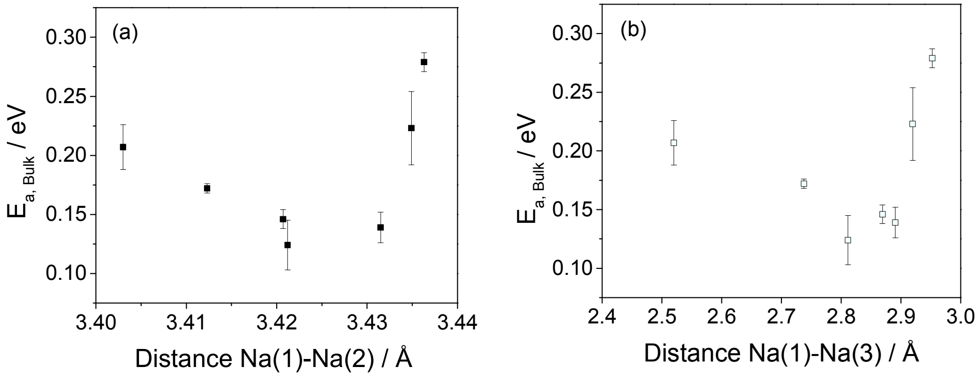

Figure 5.6: Correlation between the activation energy of the bulk conductivity and the interatomic distance between the Wyckoff positions (a) Na(1) and Na(2) and (b) Na(1) and Na(3).

An increasing hopping distance for the Na^+ ions is not favourable and leads to a high activation energy. In the case of $NSSiP_x$, the activation energy for the Na conduction rises when the distance between the positions Na(1) and Na(2) exceeds 3.433 Å. For shorter Na(1)-Na(2) distances, the activation energies slightly increase. Therefore only a tentative optimum distance at about 3.42-3.43 Å leading to the lowest activation energy can be deduced from Figure 5.6 (a).

The existence of an optimum hopping distance, about 2.8 – 2.9 Å, was also observed between the Na(1) and the Na(3) position (Figure 5.6 (b)). This is in agreement with the fact that the position Na(3) is a displacement of the Na(2) position as analysed using the neutron scattering data.

5.3.2. Bottleneck of Na conduction

As described in Chapter 2.3.5 the size of the smallest triangle of oxygen through which the Na^+ ions have to pass during the conduction (T1 in Figure 2.19) was correlated with the activation energy for approximately 30 NASICON materials with reported structural parameters [20].

Using the refined crystal structures from the XRD patterns of the $NSSiP_x$ compounds, the area of the T1 triangle was calculated. The standard deviation of the position of the oxygen atoms added to those of the lattice parameters gave an error on the area T1 of approximately 0.065 Å² so that a large scattering of the data is expected due to these errors of the area T1. In addition, the errors of activation energy for the bulk conductivity are also important so that no clear trend can be expected.

Therefore, the area of the triangle T1 for the $NSSiP_x$ solid solution was correlated to the values of activation energy of the total conductivity determined at low temperature. These values are affected by the varying grain boundary contributions for each composition but can be compared with already published data where only the activation energy of total conductivity are available, e.g. like in the case of the solid solution $Na_{1.4}M_{1.6}In_{0.4}(PO_4)_3$ as well as for scandium substituted NASICONs, $Na_{1+x+y}Zr_{2-x}Sc_x(SiO_4)_y(PO_4)_{3-y}$ [10, 90, 96, 98].

The results are presented in Figure 5.7 and a fairly good linear correlation is obtained (R² = 0.89): the trend is similar to other NASICON materials: the activation energy decreases when the T1 area increases.

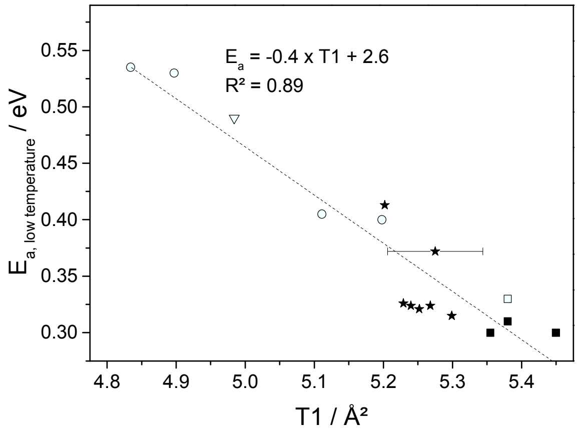

Figure 5.7: Activation energy of total conductivity as a function of the area T1 for $NSSiP_x$ (filled stars, and open reversed triangle for NSP using the structural data are from Collin et al. [90] and the activation energy from Winaud et al. [98]), $Na_{1+y+z}Zr_{2-y}Sc_y(SiO_4)_z(PO_4)_{3-z}$ [14] (filled squares), $Na_3Zr_2(SiO_4)_2(PO_4)$ [1] (open square) and $Na_{1.4}M_{1.6}In_{0.4}(PO_4)_3$ [27] (open circles) [185].

5.3.3. Distance between the Na atoms and the next oxygen atom

To assess whether other geometrical parameters could also block the conduction pathway of the Na-ions, the impact of the interatomic distance between the Na-ions and the next oxygen atoms was studied, as depicted in Figure 5.8.

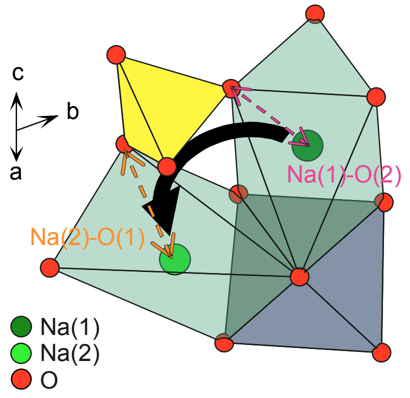

Figure 5.8: Representation of the Na(1)-Na(2) hopping for $Na_3Sc_2(PO_4)_3$ [90] along (2 -1 4). The ScO_6 octahedra are represented in grey and the PO_4 tetrahedra in yellow. The distances between the Na atoms and the next oxygen ions are indicated with dashed arrows.

The distance between the Wyckoff position Na(1) and the top of the T2 triangle O(2) was investigated as well as the distance between the Wyckoff position Na(2) and the top of the T1 triangle O(1). The results are plotted in Figure 5.9.

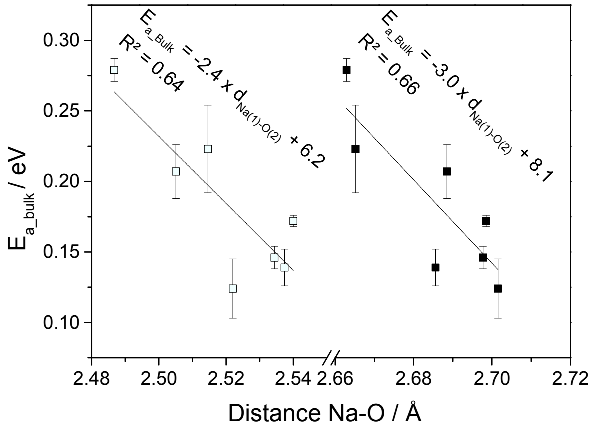

Figure 5.9: Correlation between the activation energy and the interatomic distance between the Na atoms and the next oxygen atoms in the structure: the open symbols represent the impact of the distance between Na(1) and O(2) and the filled symbols the distance between Na(2) and O(1) [185].

The correlations between the activation energy and the Na-O distances seem to reflect a reasonable linearity, even if a significant scatter was observed. Figure 5.9 also shows that both Na-O distances show the same slope although the distances of the two datasets differ by about 0.2 Å. In the case of

NSSiP$_x$, it appears that the bottleneck is merely determined by the T1 area, but rather by the Na$^+$-O^{2-} distances and the mobility is enhanced when the distances are large.

5.4. Conductivity of the mixed phase NSSiP$_{0.4}$

The conductivity results for the batch of powder analysed by neutron scattering still need to be discussed. The sample is composed of two phases of composition NSP and NSSiP$_{0.8}$. As single phase materials, the two compounds have conductivity values of 2.3 x 10^{-5} S cm^{-1} [98] and 5.6 x 10^{-5} S cm^{-1}, respectively. A similar conductivity is therefore expected for the mixed phase sample but 3.5 x 10^{-4} S cm^{-1} was measured: one order of magnitude higher than both the phases it is composed of.

Using the above described criteria, the high conductivity value of this mixed phase sample can be understood.

First, the hopping distances for the different pathways in the single phase materials are compared to those in the mixed phase material already described in Chapter 5.1:

- For the monoclinic NSP, the first pathway Na(1)-Na(2) represents a hopping distance of 3.48 Å, the second pathway Na(1)-Na(3)-Na(1) corresponds to alternate hopping distances of 1.59 Å and 4.31 Å so that the preferred pathway is the first one, since the second one does not show favorable hoping distances. In the mixed phase sample, both pathways are possible, even if the second one is preferred.
- For the rhombohedral NSSiP$_{0.8}$, the first pathway Na(1)-Na(2) corresponds to a hopping of 3.43 Å and the second pathway Na(1)-Na(3)-Na(1) represents alternate hopping of 2.95 Å and 3.78 Å. These values represent no significant differences compared to the rhombohedral phase in the mixed phase sample (3.41 Å and 2.98 Å-3.81, respectively).

From these considerations of hopping distance, the higher conductivity of the NSP phase in the mixed phase sample is understandable by the more favorable distances along the second pathway.

The study of the bottleneck also gives insights for the high conductivity. For NSP and NSSiP$_{0.8}$, the areas T1 are reminded in Table 5.3 as well as the calculated area T1 from both phases refined from the neutron scattering data.

Table 5.3: Area T1 for both the NSP and NSSiP$_{0.8}$ material as pure phase materials or in the NSSiP$_{0.4}$ sample analyzed via neutron scattering.

Phase	Area T1 for the single phase material / Å²	Area T1 in the batch analysed via neutron scattering / Å²
NSP	4.984 [90]	5.022
NSSiP$_{0.8}$	5.229	5.296

For both phases, the area T1 is bigger in the mixed phased sample, explaining its higher conductivity. In addition, it is interesting to note that the average value T1$_{av}$ = 5.159 Å² for both phases is very close to the area T1 for the pure phase NSSiP$_{0.4}$ of 5.252 Å².

The size of the lattice of both phases in the mixed phase sample was already discussed in Chapter 4.2.2. In Table 5.4, they are compared to rhombohedral NSSiP$_{0.8}$ and NSSiP$_{0.4}$ and monoclinic NSP. For the rhombohedral materials, the cell was transformed in its equivalent monoclinic cell.

Table 5.4: Refined lattice parameters in the equivalent monoclinic cell for NSP and $NSSiP_{0.8}$ in the mixed phase sample compared to the data of $NSSiP_{0.8}$, $NSSiP_{0.4}$ and NSP [90].

	a / Å	b / Å	c / Å	β / °
Monoclinic NSP in mixed phase sample	15.549	8.982	9.064	124.73
Rhombohedral $NSSiP_{0.8}$ in mixed phase sample	15.566	8.987	9.046	125.00
Rhombohedral $NSSiP_{0.8}$ single phase	15.646	9.033	8.996	125.43
Rhombohedral $NSSiP_{0.4}$ single phase	15.554	8.980	9.041	124.99
Monoclinic NSP single phase	15.404	8.919	9.103	123.53

Both phases in the mixed phase sample have similar lattice parameters very close to the lattice parameters of pure phase $NSSiP_{0.4.}$ The composition of the mixed phase sample can therefore be described as followed: the sample is composed of one NASICON structure with inhomogeneous distribution of Si so that two phases can be distinguished: a Si-rich phase refined as $NSSiP_{0.8}$ and a Si-poor phase refined as NSP. Both phases have similar lattice parameters and the rotation of the (PO_4) tetrahedral differs from one phase to the next leading to a loss of symmetry in NSP. Nevertheless, the high area T1 in both phases allows the sample to reach satisfactory values of conductivity.

6. Results and discussion part 2: Solid electrolyte tested in NIB

In this chapter, preliminary studies of solid-state Na-ion batteries with $NSSiP_{0.4}$ will be described. In all the following battery designs the electrolyte was a 1 mm thick dense pellet of $NSSiP_{0.4}$. Table 6.1 summarises the different cathode and anode materials tested in combination with the $NSSiP_{0.4}$ electrolyte as well as the specific capacity of the tested batteries before and after cycling at different C-rates.

Table 6.1: Summary of the different battery designs with dense $NSSiP_{0.4}$ pellet electrolyte.

Cathode	Anode	Type of electrode	Performances
$Na_3V_2(PO_4)_3$	Na	Mixed cathode slurry	25 % of theoretical capacity at C/11 dropping to 16 % after 30 cycles
NaV_3O_8	Na	Thin film cathode	10 % of theoretical capacity at C/2.6 dropping to 3 % after 25 cycles
Mo_3Sb_7	Na	Thin film anode (tested against Na)	52 % of theoretical capacity at C/17 dropping to 51 % after 3 cycles
Cu_2Sb	Na	Thin film anode (tested against Na)	15 % of theoretical capacity at C/12.6 dropping to less than 1 % after 11 cycles
NaV_3O_8	Mo_3Sb_7	Thin film cathode and anode	No possible charge/discharge
NaV_3O_8	Cu_2Sb	Thin film cathode and anode	2.3 % of theoretical capacity at C/10 dropping to 1 % after 11 cycles

In the following, the work on the $Na_3V_2(PO_4)_3$ and NaV_3O_8 cathode will be presented as well as the performance of the NaV_3O_8 | $NSSiP_{0.4}$ | Cu_2Sb cell.

The cycling of the Sb-containing anodes against Na metal will not be further developed, neither will be the NaV_3O_8 | $NSSiP_{0.4}$ | Mo_3Sb_7 cell since it was cycled but not charged and discharged.

6.1. Mixed phase cathode

6.1.1. Results

In the first cell design the NASICON material $Na_3V_2(PO_4)_3$ (NVP) was used as cathode and Na metal as anode. It is known that the electronic conductivity of NVP must be enhanced [209, 210] so carbon black was added. In addition, $NSSiP_{0.4}$ was mixed with the NVP cathode in order to have a higher contact area between the electrolyte and the cathode as pointed out by Lalère et al. [15].

The chemical stability between $NSSiP_{0.4}$ and NVP was first investigated with TG/DSC and XRD as seen in Figure 6.1. For this investigation, the samples were not stored in dry conditions.

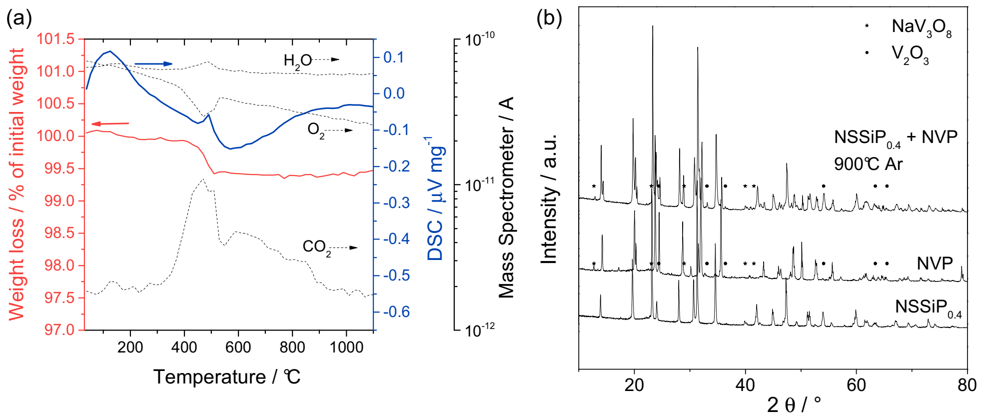

Figure 6.1: (a) DSC/TG up to 1100 ℃ in Ar of a mixture of NS SiP$_{0.4}$ and NVP powders coupled with a mass spectrometer. Masses 18 (H_2O), 32 (O_2), and 44 (CO_2) are shown as dotted lines and (b) ex-situ XRD pattern of NSSiP$_{0.4}$ and NVP powder after heat treatment at 900 ℃ in Ar.

A peak at 119 ℃ in the DSC curve as well as in the mass spectrometer line of the mass 18 associated to a weight loss shows the evaporation of water from the samples stored in air. Similarly, at 480 ℃, a weight loss is associated to a peak in the mass 18, 32 and 44 showing the loss of CO_2 and water of the samples. No other peak reflecting a reaction between NVP and NSSiP$_{0.4}$ is detectable proving their chemical compatibility. The powder mixture was annealed at 900 ℃ in argon and the stability of both materials is also confirmed by the ex-situ XRD analysis. In Figure 6.1(b), the impurity phases of NaV_3O_8 and V_2O_3 were already present in the cathode material before annealing.

The NVP | NSSiP$_{0.4}$ | Na battery prepared as described in Chapter 3.1.3 was cycled at room temperature with a speed of 10 mV/s, 1 mV/s and 0.1 mV/s. The corresponding CV results are shown in Figure 6.2.

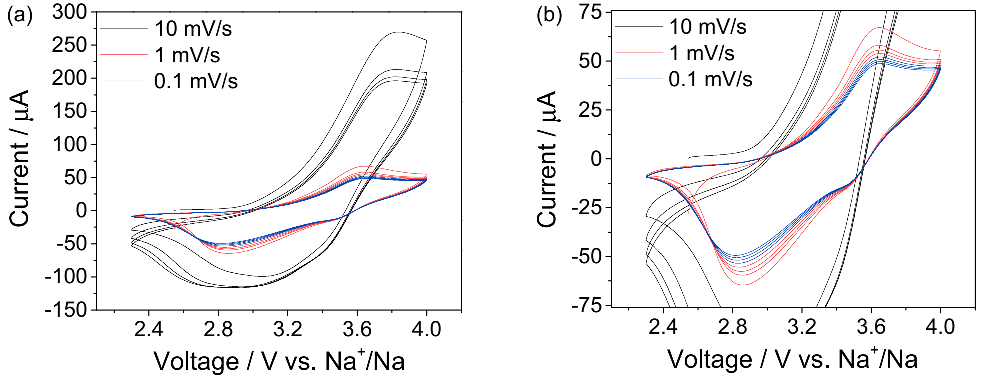

Figure 6.2: Cyclic voltammogram of the Na | NSSiP$_{0.4}$ | NVP/ NSSiP$_{0.4}$ battery between 2.3 and 4 V for 10 mV s^{-1}, 1 mV s^{-1} and 0.1 mV s^{-1} for 4 cycles. (a) represents the whole current range from -150 to 300 µA and (b) a zoom between -76 and 76 µA.

The battery can be cycled and the transition from V^{3+} to V^{4+} is observed around 3.4 V as expected [210]. The broad peaks and the potential difference between anodic and cathodic peaks of 0.6 V is the result of a high internal resistance of the cell. The shift of the anodic peak for different speed rate is due to kinetics of the system that cannot stabilise at higher speed rates.

The cell was then charged and discharged for 30 cycles between 2.5 and 4 V. For the first 2 cycles, a charge current of 20 µA corresponding to a C-rate of C/5.5 (calculated with a theoretical capacity of 117 mAh g^{-1} [62, 63] and 0.948 mg of active material) was used but the cell was not charging properly and the efficiency was diminishing too fast. The other 28 cycles were carried out with a charge current of 10 µA corresponding to a C-rate of C/11.

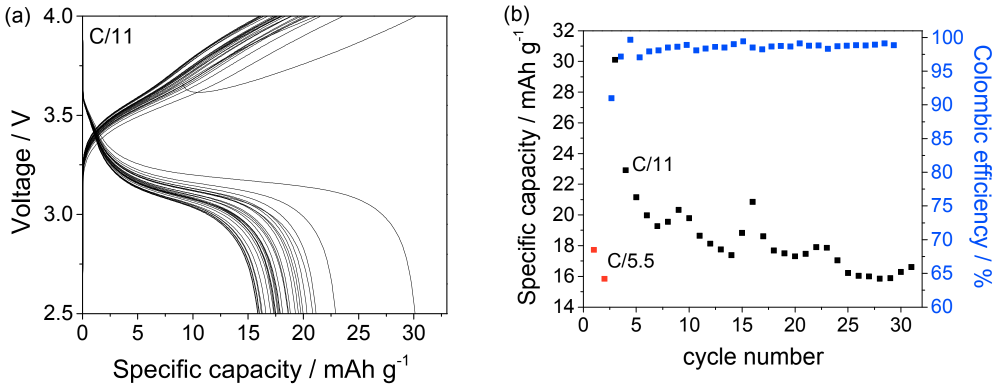

Figure 6.3: (a) Charge/discharge profiles of the NVP | $NSSiP_{0.4}$ | Na battery at 10 µA in a voltage range of 2.5 – 4 V. (b) Cycling performance of the NVP | $NSSiP_{0.4}$ | Na battery.

The cell has a very low specific capacity of 16 mAh g^{-1} compared to the theoretical specific capacity of NVP of 117 mAh g^{-1}. Furthermore, over the 30 cycles a loss of capacity of approximately 50 % is observed. In parallel, the coulombic efficiency stays fairly stable. In Chapter 2.2.1, it was defined as the ratio of the output of charge to the input of charge, so the loss of capacity during charge and discharge is equivalent since the loss of capacity is not combined with a loss of coulombic efficiency.

6.1.2. Post mortem analysis

The post mortem analysis of the cell can only be conducted on the cathode side since the sample has to be taken out of the argon-filled glove box and the sodium layer is removed prior to investigation for safety reasons.

The loss of capacity is understood after inspection of the cell in the SEM (Figure 6.4) revealing poor contact between the cathode layer (top of the picture) and the electrolyte (grey layer at the bottom of the picture). In batteries, the so-called phenomenon “breathing” of the cathode corresponding to its volume changes between charge and discharge [211, 212] or more precisely here the volume differences between the sodiated and desodiated cathode approximated to 8.26 % [213] between $Na_3V_2(PO_4)_3$ and $NaV_2(PO_4)_3$, induces a gap between the cathode and the electrolyte layer as observed here.

In this battery design, the preparation of the mixed cathode should be optimised. A good mixing is observed since every particle of electrolyte (light grey particles) is surrounded by the carbon/cathode powder (dark grey regions) but the particle size distribution of the electrode phase is not monomodal as particles of 10 µm are observed as well as smaller particles of 1–2 µm. A better milling of the preparation is necessary to have a homogenised distribution.

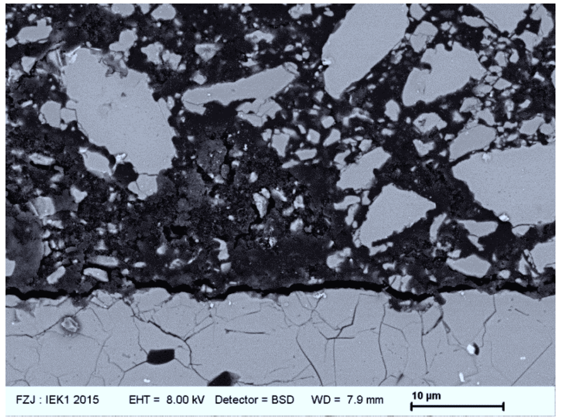

Figure 6.4: SEM picture of the contact between the mixed cathode and the electrolyte after 30 cycles.

Another drawback of the preparation is the low density of the mixed cathode. The sintering temperature of NVP is 900 °C and of NSSiP$_{0.4}$ is 1280 °C. The mixed sample was sintered at 900 ° C. For two ceramic materials with different sintering temperatures as it is the case in the present study, a constrained sintering occurs shifting the sintering of both phases to higher temperature [214]. In conclusion, the preparation of the mixed cathode at 900 °C didn't allow a good densification as it is observed in Figure 6.4 were pores are visible, leading to high internal resistance. Lalère et al. experienced this difficulty as well in the co-sintering of all the battery layers and their electrolyte phase also did not show a sufficient conductivity due to its low density. That is why they cycled the battery at 200 °C [15].

Two approaches are possible to enhance the too low ionic conductivity in the mixed-cathode leading to the already mentioned high internal resistance of the cell:

- The density of the mixed cathode materials could be enhanced by optimising the particle size and investigating other sintering methods like pressure assisted sintering.
- The influence of the ratio electrolyte/active material also has to be investigated and optimised.

In addition, secondary phases are observed in the SEM picture as white dots and their presence was also confirmed by the XRD analysis of the cathode after cycling (Figure 6.5).

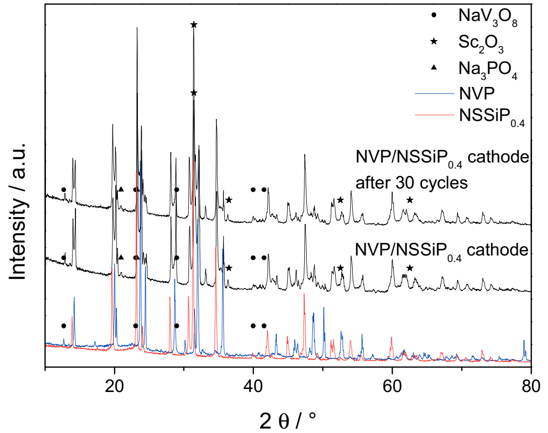

Figure 6.5: XRD pattern of the NVP/NSSiP$_{0.4}$ mixed cathode as prepared and after 30 cycles at room temperature between 2.5 and 4 V, compared to the XRD patterns of the NVP and NSSiP$_{0.4}$ powders.

The NaV_3O_8 impurity phase was detected in the cathode material but also an additional decomposition of the $NSSiP_{0.4}$ electrolyte to Na_3PO_4 and Sc_2O_3 is observed even before the cycling although the stability of NVP and $NSSiP_{0.4}$ was verified before. This leads to the third reason for the high resistance of this battery: impurity phases were present in the cathode layer.

Nevertheless, it was possible to cycle the cell meaning that even with its high internal resistance the conduction of the Na^+ ions from the anode to the cathode through the electrolyte occurred as well as the intercalation in the active material of the cathode.

Taking a closer look at the CV results of this cell (Figure 6.2), the peak intensity shows a reasonable linear correlation with the square root of the scan rate as shown in Figure 6.6. As mentioned before (Equation 34), this is the case for a reversible process. In addition, for the scan rates of 0.1 and 1 mV s^{-1}, the anodic and cathodic peaks have the same height meaning that the same amount of sodium is inserted in the anode during charge and inserted in the cathode during discharge (Equation 33). This result is in agreement with the coulombic efficiency of approximately 100 %. Nevertheless, at the highest scan rate of 10 mV s, the system did not have the time to stabilize and the anodic and cathodic peaks showed discrepancy. The anodic peak is higher showing that more sodium is extracted from the cathode during the charge as inserted during the discharge.

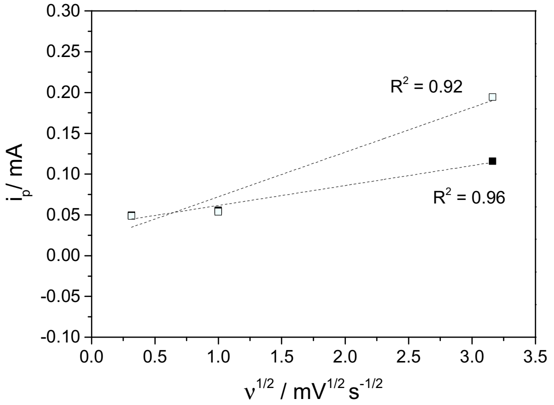

Figure 6.6: Intensity of the cathodic peak (filled symbols) and of the anodic peak (open symbols) as a function of the square root of the scan rate.

6.2. Thin film cathode

To improve the contact between cathode and electrolyte, another deposition technique was used at ORNL: the deposition of the cathode, in this case NaV_3O_8, by PVD as described in Chapter 3.1.4.

6.2.1. NaV_3O_8 against Na metal

After the deposition of the cathode on the dense electrolyte an annealing step is needed to crystallise the cathode. Different temperatures for different annealing times were investigated as listed in Table 6.2. The difference in the weight of the cathodes is related to the different diameter of the $NSSiP_{0.4}$ support.

Table 6.2: Optimisation of the annealing temperature and time for the crystallisation of NaV_3O_8.

NaV_3O_8 film thickness	NaV_3O_8 weight	Annealing temperature	Annealing Time
425 nm	0.137 mg	400 ℃	1 h
691 nm	0.162 mg	400 ℃	4 h
691 nm	0.184 mg	400 ℃	12 h
691 nm	0.223 mg	600 ℃	4 h

Figure 6.7 shows the XRD pattern of the samples annealed at 400 ℃ for 1, 4 and 12 h. The thin film evaporated from the sample annealed at 600 ℃ (the pellet came out of the oven with white colour, without any film on the surface). The reference pattern for NaV_3O_8 is taken from a layer deposited on alumina with the same parameters (K. Browning [215]).

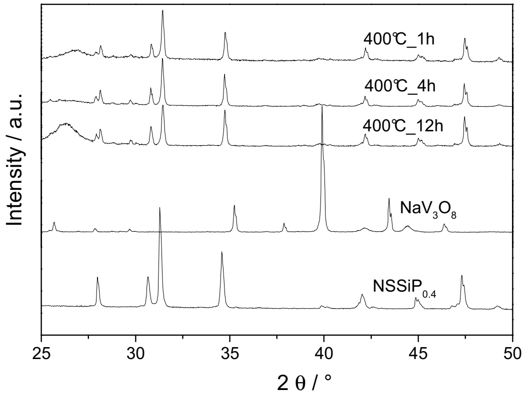

Figure 6.7: XRD pattern of the NaV_3O_8 thin films annealed at 400 ℃ for 1, 4 and 12 h.

The major reflections observed are from the pattern of the NASICON substrate and the reflection at 2θ = 40 ° of the reference NaV_3O_8 is not detectable for the samples on the $NSSiP_{0.4}$ pellets. Nevertheless, reflections at 2θ = 27.9 ° and 29.7° match with the reference demonstrating the existence of the crystalline NaV_3O_8 thin film.

A better intensity was obtained with grazing incidence XRD (GIXRD) between 2θ = 5 ° and 100 ° as seen in Figure 6.8.

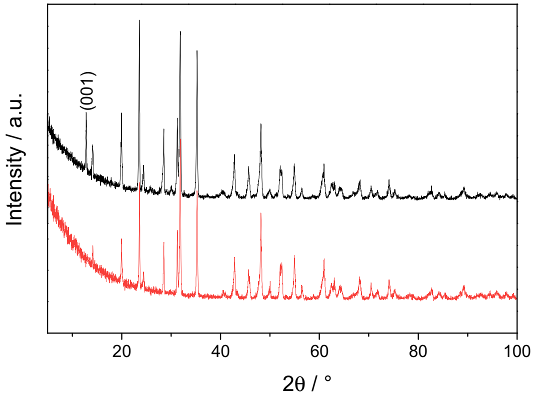

Figure 6.8: GIXRD of a $NSSiP_{0.4}$ pellet (red curve) and of the NaV_3O_8 thin film deposited on a $NSSiP_{0.4}$ pellet (black curve).

The reflection at 2θ = 12.8 ° shows the highest intensity proving that the film grows with a preferred orientation along (hkl) = (001), i.e. along the c-axis [52] as schematically represented in Figure 6.9. It was discussed in Chapter 2.2.2 and Figure 2.6 that the most preferable orientation would be along the b-axis since it is the most favorable Na conduction pathway but with this growing direction, no VO_x (x = 4 or 6) polyhedral hinders the transfer of Na^+ ions from the NASICON substrate to the thin film cathode, which is essential for the functioning of the battery.

The preparation of the thin film cathode this way is therefore suitable to build a NIB.

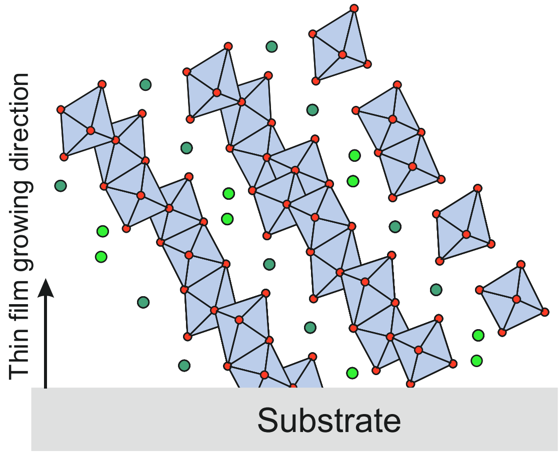

Figure 6.9: Representation of the growing direction of the thin film of NaV_3O_8 on the NASICON substrate along the c-axis. The data are taken from [55], the VO_x polyhedra are represented in grey and the Na atoms in green.

Since the cathode is a thin film, no additive was used to enhance its electronic conductivity. Carbon black is not a possible candidate because the cathode needs to be annealed in air at 400 ℃. In this study, no work was invested in this direction but this has to be kept in mind for a further improvement of the cathode.

SEM pictures were made after annealing to evaluate the thickness of the thin film cathode and the adherence to the electrolyte.

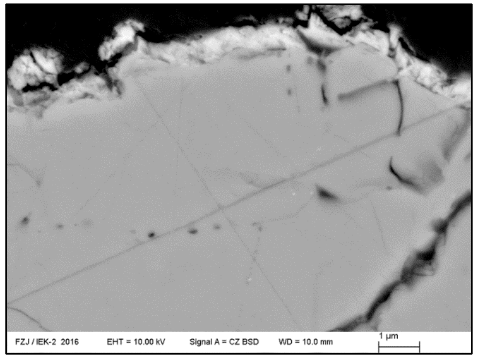

Figure 6.10: SEM pictures of the NaV_3O_8 cathode after annealing for 4 h at 400 ℃ on an NS SiP$_{0.4.}$

In Figure 6.10, it is clearly visible that the surface of the electrolyte pellet was not satisfactory as it was not smooth and the deposition of the thin film on the pellet was difficult to achieve. Nevertheless, the layer of NaV_3O_8 is recognized and presents a thickness of half a µm approximately, which matches the expectation. Furthermore, on the grain presented in this picture, the contact of the NaV_3O_8 thin film on the electrolyte seems to be acceptable.

The samples annealed for 4 h and 12 h do not show significant differences in the XRD so their electrochemical activity was tested against Na metal. NaV_3O_8 | $NSSiP_{0.4}$ | Na batteries were charged and discharged from 1.8 to 4 V with a speed rate of 10 µA corresponding to C/2.6. The results for a sample annealed for 4 h are shown in Figure 6.11. The first discharge plateau corresponds to 10 % of the theoretical capacity and a significant capacity loss is observed over the 25 cycles. During the discharge cycles, a contact problem is observed leading to the irregularities in the charging curves.

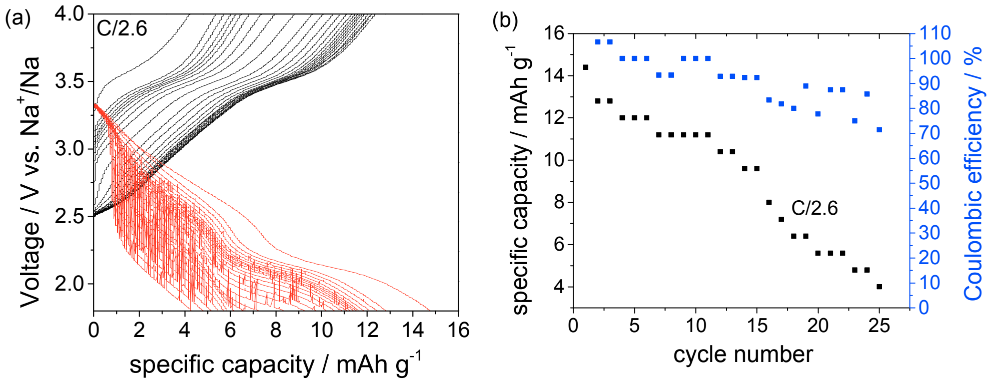

Figure 6.11: (a) Charge/discharge profiles of the NaV_3O_8 (annealed 4 h)| $NSSiP_{0.4}$ | Na cell at 10 µA in a voltage range of 1.8-4 V. (b) Cycling performance of the cell.

For both 4 h and 12 h annealing time, the cathode proved being electrochemically active and the cell could be charged and discharged over 25 cycles but the capacity is really low with less than 3 % of the theoretical capacity (145 mAh g^{-1} [52]). The same thin film deposited on alumina and cycled with liquid electrolyte achieved 80 % of the theoretical capacity [215]. Since the cathode annealed for 4 h showed electrochemical activity and no improvement was obtained from annealing for a longer time, the annealing time of this cathode was fixed to 4 h for the next samples.

SEM pictures of the NaV_3O_8 cathode with the Au current collector layer on top were made after this cycling for 25 cycles (Figure 6.12).

The cathode material is not dense at all and under the Au layer it looks as if it crumbled. This morphology of the cathode was probably aggravated by the metallographic preparation of the sample. For a very fragile layer, the grinded and polishing of the embedded sample can lead to damages. After the cycling, the cathode material was not dense anymore, which probably explains the loss of capacity.

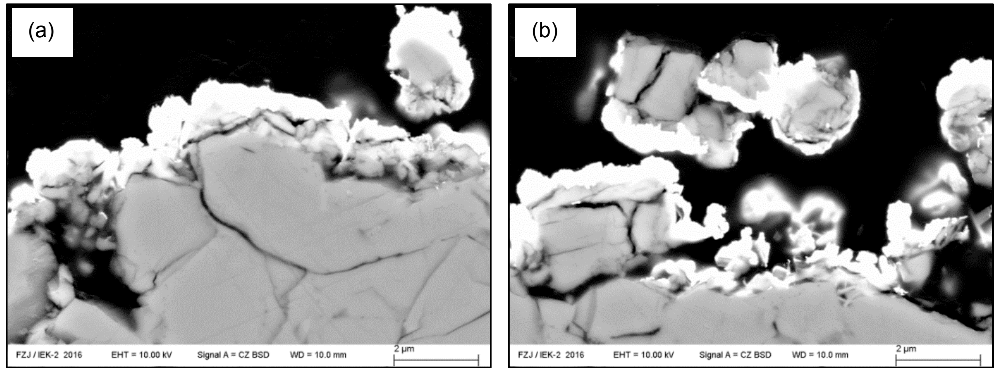

Figure 6.12: SEM picture of the Au | NaV_3O_8 | $NSSiP_{0.4}$ cell after 25 cycles. (a) and (b) represent two different spots on the cathode.

6.2.2. Mo_7Sb_3 and Cu_2Sb thin film anodes

Mo_3Sb_7 | $NSSiP_{0.4}$ | Na and Cu_2Sb | $NSSiP_{0.4}$| Na cells were cycled between 0.25 and 1.5 V and between 0.2 and 1.4 V, respectively. The applied current of 10 µA corresponds to C/17 for Mo_3Sb_7 and C/12.6 for Cu_2Sb. Unfortunately, only a poor adherence of the sodium metal on the $NSSiP_{0.4}$ could be achieved. Nevertheless, the obtained capacity of 255 mAh g^{-1} represents 52 % of the theoretical capacity for Mo_3Sb_7 (494 mAh g^{-1} [75]) and for Cu_2Sb the first discharge capacity was 50 mAh g^{-1}, which corresponds to 15 % of the theoretical capacity.

For both anode materials, as well as for the testing of NaV_3O_8 against Na, a lot of difficulties and unknown phenomena occur because of the use of Na metal in the cells:

- The first difficulty is to get a good contact between the Na metal and the ceramic electrolyte. The adherence is really poor and a lot of methods were tried out like pressing the disc of Na or heating it up but in the second case, the wetting is not satisfactory. This problem is also well known and discussed for liquid anode cells were alloys are used to improve the wetting on Na on ceramic electrolytes, for example Na-Cs alloys [216]. A trial with Na-Au alloy was conducted without any success. Na evaporation would be the most suitable method to work with Na anode.
- Another difficulty is the quality of the Na metal. Na is very reactive and if the atmosphere in the glovebox is not dry enough, the metallic Na oxidises and an insulating layer can be found on the side of the electrolyte or on the side of the current collector leading to huge internal resistance values.
- At last, dendrites of Na might have grown in the $NSSiP_{0.4}$ electrolyte as some silver coloured dots on the Na side of the electrolyte indicate (Figure 6.13) and would explain the poor charging of the cell

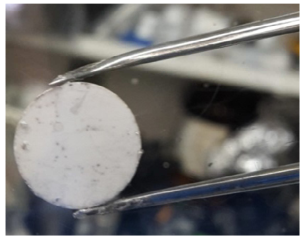

Figure 6.13: Na side of the $NSSiP_{0.4}$ pellet after cycling of the Mo_3Sb_7 | $NSSiP_{0.4}$ | Na cell.

Nevertheless, in the case of both anode materials, the obtained capacity values are promising and the anodes were used in cells with NaV_3O_8 thin film cathode to get rid of the problematic metallic Na anode.

6.2.3. NaV_3O_8 | $NSSiP_{0.4}$ | Cu_2Sb cell

The first attempts to charge/discharge the cell were not successful because of contact problems, but cyclic voltammetry tests could be carried out between 0.2 to 3 V at a speed of 1 mV/s as seen in Figure 6.14.

During the first cycle, the Na^+ ions are inserted in the anode to make the Na_xSb alloy, after that all the cycles look similar with 2 anodic peaks around 2 V (from 2.1 V to 1.9 V over the cycles) and 1.15 V (from 1.14 to 1.23 V over the cycles) and one cathodic peak at 0.5 V. The V^{4+} to V^{5+} oxidation happens at different voltages as observed earlier [217-219]. Kang et al. verified the oxidation states of vanadium during the charging and confirmed that both peaks in the cyclic voltammogram correspond to the redox couple V^{4+} / V^{5+} [217]. The presence of two redox peak was explained by Kawakita et al. [219]. There are different available sites with energy differences for holding Na-ions and the insertion of Na in these different sites can happen at different voltages. The mean value of 1.6 V matches previous studies: the V^{4+} to V^{5+} oxidation should happen around 2.4 V [52] and the reference of the anode is 0.75 V.

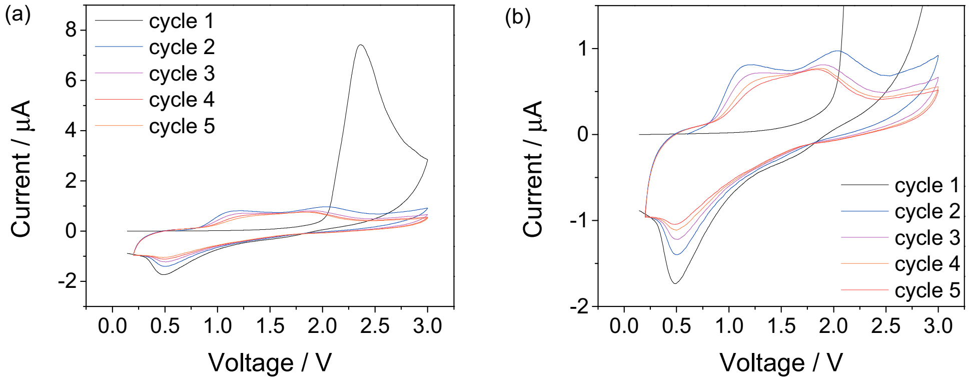

Figure 6.14: Cyclic voltammogram of the Cu_2Sb| $NSSiP_{0.4}$| NaV_3O_8 cell between 0.2 and 3 V for 1 mV/s for 5 cycles. (a) represents the whole current range from -2.5 to 9 µA and (b) a zoom between -2 and 1.5 µA.

The total mass of the cathode and the anode are 0.16 mg and 0.4 mg respectively, so that the redox peaks of the anode, which represents a higher capacity (323 mAh g^{-1} [76] against 145 mAh g^{-1} [52]), are not to be distinguished in the cyclic voltammogram.

The potential difference between the redox peaks of 1.1 V is very high but comparable to previous studies on the cathode material (0.86 V potential difference for one of the samples in the study [218]). This is the result of a high internal resistance of the cell. Nevertheless, this solid-state battery is cycling which represents a very promising first result.

Figure 6.15 represents the charge/discharge profile of a battery with same composition at 2 µA (C/10) over 10 cycles.

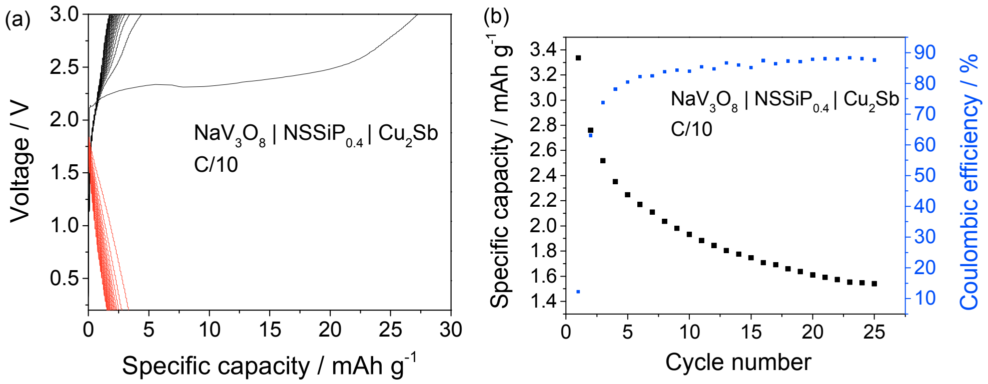

Figure 6.15: (a) Charge/discharge profiles of the Cu_2Sb| NSSiP$_{0.4}$| NaV_3O_8 cell at 2 µA in a voltage range of 0.2 – 3.0 V. (b) Cycling performance of the cell.

The first charge is different than the other ones exactly like previously observed in the cyclic voltammogram (Figure 6.14) because the Na enters the Cu_2Sb anode forming the Na_xSb alloy. After this first cycle, the specific capacity corresponded to 2.3 % of the theoretical capacity of NaV_3O_8 and drops to 1 % of theoretical capacity after 25 cycles. This value of capacity is not satisfactory.

In Figure 6.16, SEM pictures of the anode and cathode side of the cell after the electrochemical testing are shown. The anode side presents a dense and uniform layer covering the entire electrolyte and shows no cracks or other defects.

The NaV_3O_8 cathode shows a better microstructure as after its testing against Na metal. Nevertheless, a gap is observed between the electrolyte and the cathode and once again the breathing of the cathode [211, 212] leads to a loss of contact between cathode and electrolyte.

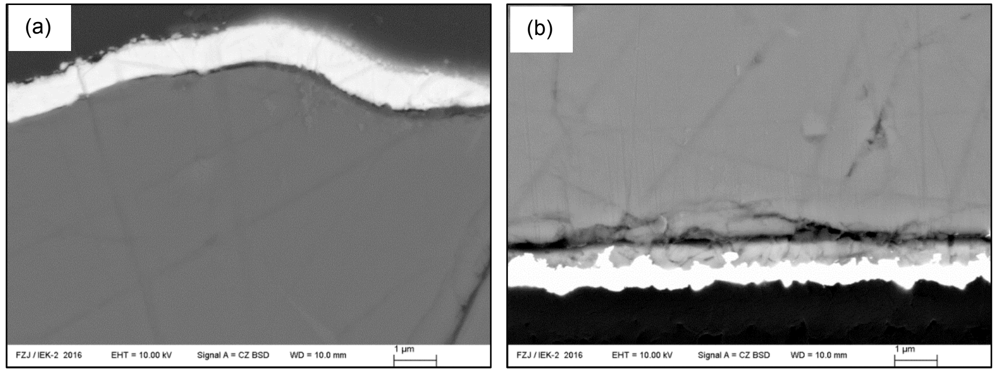

Figure 6.16: SEM picture of (a) the Cu_2Sb anode and (b) the Au | NaV_3O_8 cathode after cycling of the Cu_2Sb | NSSiP$_{0.4}$| NaV_3O_8 cell.

Overall, the following three main factors lead to the high resistance of the cell:

- The poor microstructure of the electrolyte leading to lower conductivity values. The pellets used for these preliminary battery tests presented the already mentioned defects in NASICON materials: micro cracks and pores between the grains.
- The presence of a gap between the cathode and the electrolyte not allowing the Na-ions to transfer from one material to the next.
- The low electronic conductivity of the cathode that was not enhanced with additives.

Nevertheless, two very positive results can be concluded from these results:

- The issue of bad contact with Na metal in the solid-state battery was resolved by using Cu_2Sb anode and its preparation leads to satisfactory layers.
- For the first time, a solid-state Na battery based on inorganic materials could be cycled at room temperature.

In addition, it is worth noting that this design of a solid-state battery is not optimal; to reach the best efficiency, a thin electrolyte (with very low resistance) should be combined with thick electrodes (high energy density). As a matter of fact, using a thick electrolyte as substrate allows sintering it prior to the deposition of the cathode, which has to be annealed at lower temperature. It was already mentioned that one challenge for the building of solid state batteries is the difference in annealing temperature for all the compounds. This can be handled with the design used here.

7. Summary and conclusion

In this thesis, NASICON-type materials as potential solid ceramic electrolytes for solid-state Na-ion battery were investigated. The NASICON materials have been known and thoroughly studied since the 1970s but the interest was lost shortly after the commercialisation of the concurrent β-alumina. Nevertheless, in the past years, these solid electrolytes attracted attention again because of the concerns of high processing costs and fragility of the β-alumina.

Comparing approximately 110 reported NASICON materials mainly from the 1980s and 1990s, a guideline to achieve high conductivity for materials with general formula $Na_{1+2w+x-y+z}M^{(II)}_wM^{(III)}_xM^{(V)}_yM^{(IV)}_{2-w-x-y}(SiO_4)_z(PO_4)_{3-z}$ was first developed:

- The amount of Na per formula unit, achieved by compensating the valence of the substituted M cations and Si should be between 3 and 3.5 mol.
- The mean ionic radius of the M cations should be approximately 0.72 Å.
- The substitution of P with Si also has a positive impact on the conductivity.

This guideline led to the investigation of the solid solution $Na_{3+x}Sc_2Si_xP_{3-x}O_{12}$ for $0 \leq x \leq 0.8$ on three main aspects:

- Crystal structure
- Conductivity values and activation energy of the Na transport
- Use of one $NSSiP_x$ material as a solid electrolyte in NIBs.

From the crystallographic analysis of the materials, information about both the rhombohedral and the monoclinic NASICON structure were gathered and for $x > 0$, the material is mainly rhombohedral. Nevertheless, it was observed that the transition from one structure to the next does not require a lot of energy and for one batch of sample with $x = 0.4$, a ratio 1:1 of both structures was obtained after an additional annealing step. Comparably, single crystals of NSP ($x = 0$) showed a rhombohedral structure instead of the expected monoclinic. Already in the late 1980s, Collin et al. [186] interpreted the smooth changes from one symmetry to the next with different arrangement of the Na atoms in the structure. These explanations could not be finished within this work since neutron diffraction data were obtained on only one composition and single crystal XRD data are still in progress.

The conductivity study of the solid solution gave similar results as for the solid solutions $Na_{1+x}Zr_2Si_xP_{3-x}O_{12}$ [10] and $Na_{1+x}Hf_2Si_xP_{3-x}O_{12}$ [22] as represented in Figure 7.1. A dome-shaped curve is obtained between the conductivity of the materials and the Na(1) site occupation, which is strongly related to the total Na concentration and linked to the amount of Si of the compounds. The maxima of conductivity are in all cases achieved for a concentration of Na between 3 and 3.5 mol, more precisely 3.4 mol for the $NSSiP_x$ materials. This concentration seems to be an optimum value for more NASICON-type materials. For example in a very recent study, Ma et al. found the highest conductivity in the series $Na_{3+x}Sc_xZr_{2-x}Si_2P_3O_{12}$ when $x = 0.4$ [220].

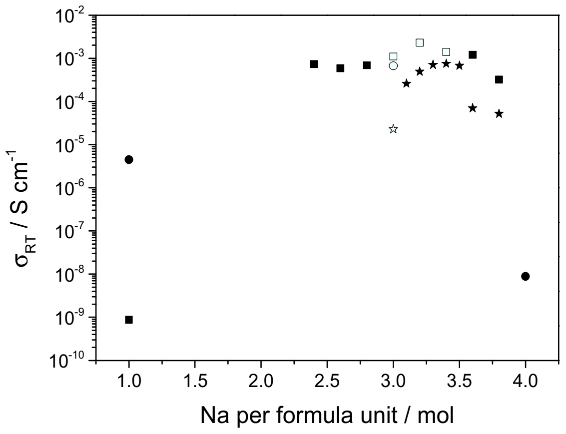

Figure 7.1: Conductivity at room temperature against Na content for $Na_{1+x}Zr_2Si_xP_{3-x}O_{12}$ [10] (circles), $Na_{1+x}Hf_2Si_xP_{3-x}O_{12}$ [22] (squares) and $NSSiP_x$ (stars). All materials with filled symbols have rhombohedral structure, the open symbols correspond to monoclinic materials.

For x = 0.4, the conductivity at room temperature of 8×10^{-4} S cm^{-1} places this compound amongst the 10 best Na-conductive NASICON materials as indicated in Figure 7.2. This result also confirms the validity of the guideline to design high conductive sodium-based NASICONs.

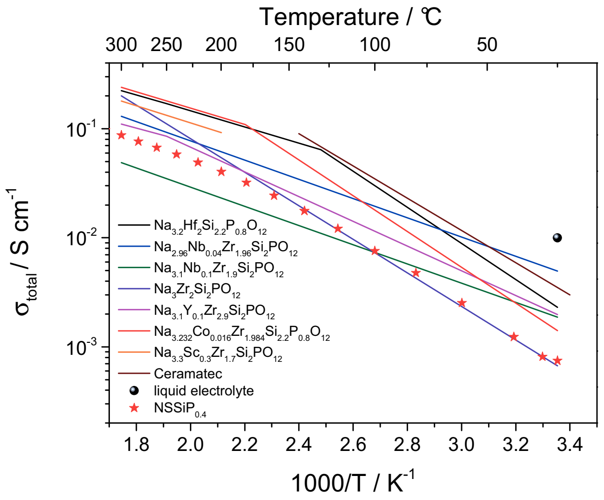

Figure 7.2: Arrhenius plot of the total conductivity of sintered polycrystalline NASICON material from the company Ceramatec [80] and seven of the best NASICON-type Na ionic conductors [10, 22, 95, 96, 108] compared to $NSSiP_{0.4.}$

Nevertheless, the goal of reaching the ionic conductivity of liquid electrolyte is still not achieved and a lot of efforts have to be put in the processing of the material. As a matter of fact, the bulk conductivity is satisfactory; the difficulty lies in tuning the grain boundaries to get as low resistance as possible. In addition, micro-cracks form easily in this material and they have a negative impact on the conductivity and battery performances. That is why new synthesis routes have to be investigated or high energy milling to reduce the particle size. One possibility investigated by Ma et al. is the solution-assisted solid-state reaction leading to nano-powder with very low grain boundary resistance [220].

In the future, the study of the NASICON structure could be deepened so that the conditions leading to the monoclinic or the rhombohedral phase becomes clearer. For this purpose, the compilation of a phase field diagram would be of great use. In addition, a profounder study of the formation of the micro-cracks should be carried out to obtain defect-free electrolyte layers, maybe also working on diminishing their thickness by application of ceramic processing techniques, e.g. tape casting opening the way to industrial production. Finally, this study of scandium-based NASICON materials was an exploratory work but the results presented in this thesis should be applied to investigate NASICON materials without critical elements (Sc, Co, N, Nb…) in order to prepare cheaper electrolytes.

Despite the comparatively low conductivity of the best samples of $NSSiP_{0.4}$ compared to liquid electrolyte, their usability as solid electrolyte could be demonstrated in several battery designs. In all cases, the achieved capacities were still not satisfactory and a lot of optimisation is required to improve the efficiency of the different cells.

- The cell prepared with a mixed cathode slurry can be improved by a more homogeneous mixing of the electrode and the electrolyte within the mixed cathode. In addition, impurity phases were present in the cathode material and its synthesis should be improved. In this battery design, one issue is also the contact between the electrolyte and the electrodes. On the one side, the adherence of the Na metal anode adherence is not optimal on the ceramic pellet, on the other hand, the cathode slurry was only hand-brushed and better deposition techniques should be used.
- The cells with thin film anode and cathodes showed promising results, especially on the anode side, with the deposition of defect-free layers allowing the absence of Na metal. In the case of this battery design, the main issue was the microstructure of the electrolyte which presented cracks and pores. In addition, the surface was hand-polished and showed a high roughness, not optimal for PVD deposition of the electrodes.

Still, the first solid-state Na-ion battery based only on inorganic materials was cycled at room temperature and this represents a very promising result.

References

1. Yang, Z., Zhang, J., Kintner-Meyer, M.C., Lu, X., Choi, D., Lemmon, J.P., and Liu, J., *Electrochemical energy storage for green grid.* Chemical Reviews, 2011. **111**(5): 3577-3613.
2. Ibrahim, H., Ilinca, A., and Perron, J., *Energy storage systems—Characteristics and comparisons.* Renewable and Sustainable Energy Reviews, 2008. **12**(5): 1221-1250.
3. Palomares, V., Serras, P., Villaluenga, I., Hueso, K.B., Carretero-González, J., and Rojo, T., *Na-ion batteries, recent advances and present challenges to become low cost energy storage systems.* Energy & Environmental Science, 2012. **5**(3): 5884-5901.
4. Pan, H., Hu, Y.-S., and Chen, L., *Room-temperature stationary sodium-ion batteries for large-scale electric energy storage.* Energy & Environmental Science, 2013. **6**(8): 2338-2360.
5. Ellis, B.L. and Nazar, L.F., *Sodium and sodium-ion energy storage batteries.* Current Opinion in Solid State and Materials Science, 2012. **16**(4): 168-177.
6. Beevers, C.A. and Ross, M.A.S., *The crystal structure of beta alumina* $Na_2O\text{-}11Al_2O_3$. Zeitschrift für Kristallographie, 1937. **97**: 59-66.
7. Sauvage, F., Laffont, L., Tarascon, J.M., and Baudrin, E., *Study of the insertion/deinsertion mechanism of sodium into* $Na_{0.44}MnO_2$. Inorganic Chemistry, 2007. **46**: 3289-3294.
8. Cao, Y., Xiao, L., Wang, W., Choi, D., Nie, Z., J. Yu , Saraf, L.V., Yang, Z., and Liu, J., *Reversible sodium ion insertion in single crystalline manganese oxide nanowires with long cyclelife.* Advanced Materials, 2011. **23**: 3155-3160.
9. Ma, X., Chen, H., and Ceder, G., *Electrochemical properties of monoclinic* $NaMnO_2$. Journal of the Electrochemical Society, 2011. **158**(12): A1307-A1312.
10. Hong, H.Y.P., *Crystal structures and crystal chemistry in the system* $Na_{1+x}Zr_2Si_xP_{3-x}O_{12}$. Materials Research Bulletin, 1976. **11**: 173-182.
11. Zaghib, K., Trottier, J., Hovington, P., Brochu, F., Guerfi, A., Mauger, A., and Julien, C.M., *Characterization of Na-based phosphate as electrode materials for electrochemical cells.* Journal of Power Sources, 2011. **196**(22): 9612-9617.
12. Barkerz, J., Saidi, M.Y., and Swoyer, J.L., *A Sodium-Ion Cell Based on the Fluorophosphate Compound* $NaVPO_4F$. Electrochemical and Solid State letters, 2003. **6**(1): A1-A4.
13. Sauvage, F., Quarez, E., Tarascon, J.M., and Baudrin, E., *Crystal structure and electrochemical properties vs.* Na^+ *of the sodium fluorophosphate* $Na_{1.5}VOPO_4F_{0.5}$. Solid State Ionics, 2006. **8**(10): 1215-1221.
14. Recham, N., Chotard, J.N., Dupont, L., Djellab, K., Armand, M., and Tarascon, J.-M., *Ionothermal synthesis of sodium-based fluorophosphate cathode materials.* Journal of the Electrochemical Society, 2009. **156**(12): A993-A999.
15. Lalère, F., Leriche, J.B., Courty, M., Boulineau, S., Viallet, V., Masquelier, C., and Seznec, V., *An all-solid state NASICON sodium battery operating at 200 ℃.* Journal of Power Sources, 2014. **247**: 975-980.
16. Zhang, H., Li, J., Zhang, H., Liang, X., Yin, C., Diao, Q., Zheng, J., and Lu, G., *NASICON-based potentiometric* Cl_2 *sensor combining NASICON with* Cr_2O_3 *sensing electrode.* Sensors and Actuators B: Chemical, 2013. **180**: 66-70.
17. Dang, H.-Y. and Guo, X.-M., *Characteristics and performance of NASICON-based* CO_2 *sensor using* $Bi_8Nb_2O_{17}$ *plus Pt as solid-reference electrode.* Sensors and Actuators B: Chemical, 2013. **178**: 163-168.
18. Shimizu, Y., Takase, S., Ida, K., Imamura, M., and Koguma, I., *Preparation of NASICON-based ceramic thick-film with electrophoretic deposition for solid-state photoluminescence device.* Key Engineering Materials, 2009. **412**: 107-111.
19. Anantharamulu, N., Rao, K.K., Rambabu, G., Kumar, B.V., Radha, V., and Vithal, M., *A wide-ranging review on NASICON type materials.* Journal of Materials Science, 2011. **46**(9): 2821-2837.
20. Guin, M. and Tietz, F., *Survey of the transport properties of sodium superionic conductor materials for use in sodium batteries.* Journal of Power Sources, 2015. **273**: 1056-1064.
21. Shannon, R.D., *Revised effective ionic radii and systematic studies of interatomic distances in halides and chalcogenides.* Acta Crystallographica, 1976. **A32**: 751-767.
22. Vogel, E.M., Cava, R.J., and Rietman, E., Na^+ *ion conductivity and crystallographic cell characterization in the Hf-NASICON system* $Na_{1+x}Hf_2Si_xP_{3-x}O_{12}$. Solid State Ionics, 1984. **14**: 1-6.

23. Larcher, D. and Tarascon, J.-M., *Towards greener and more sustainable batteries for electrical energy storage*. Nature Chemistry, 2015. **7**: 19-29.
24. Fu, J., *Superionic Conductivity of Glass-ceramics in the System* Li_2O*-*Al_2O_3*-*TiO_2*-*P_2O_5*.* Solid State Ionics, 1997. **96**: 195-200.
25. Bruce, P.G., *Solid-State chemistry of lithium power sources.* Chemical Communications, 1997. **19**: 1817-1824.
26. Kang, H., Liu, Y., Cao, K., Zhao, Y., Jiao, L., Wang, Y., and Yuan, H., *Update on Anode Materials for Na-ion Batteries.* Journal of Materials Chemistry A, 2015. **3**: 17899-17913.
27. Julien, C., Mauger, A., Vijh, A., and Zaghib, K., *Lithium Batteries Science and Technology*2016: Springer.
28. Bünting, A., *Herstellung von Elektrodenstrukturen für Lithium-Ionen-Dünnschichtbatterien*, 2015, PhD thesis, Ruhr-Universität Bochum.
29. Xu, J., *Advanced Materials for Lithium-Ion Batteries and Sodium-Ion Batteries*, 2014, PhD thesis, University of Wollongong: Institute for Superconducting and Electronic Materials.
30. Kummer, J.T. and Weber, N., *Battery having a Molten Alkali Metal Anode and Molten Sulfur Cathode*, 1968.
31. Oshima, T. and Kajita, M., *Development of Sodium-Sulfur Batteries.* International Journal of Applied Ceramic Technology, 2004(3): 269-276.
32. Kundu, D., Talaie, E., Duffort, V., and Nazar, L.F., *The Emerging Chemistry of Sodium Ion Batteries for Electrochemical Energy Storage.* Angewandte Chemie International Edition, 2015. **54**: 3431-3448.
33. Sudworth, J.L., *The sodium/nickel chloride (ZEBRA) battery.* Journal of Power Sources, 2001. **100**: 149-163.
34. Böhm, H. and Beyermann, G., *ZEBRA Batteries, enhanced power by doping.* Journal of Power Sources, 1999. **84**: 270-274.
35. Galloway, R.C. and Haslam, S., *The ZEBRA electrc vehicle battery: power and energy improvements.* Journal of Power Sources, 1999. **80**: 164-170.
36. Javadi, T. and Petric, A., *Thermodynamic Analysis of Reaction Products Observed in ZEBRA Cell Cathodes.* Journal of the Electrochemical Society, 2011. **158**(6): 700-704.
37. Coors, W.G., Boxley, C., Robins, M., and Eccleston, A., *Low temperature molten sodium secondary cell with sodium ion conductive electrolyte membrane*, 2012.
38. Barker, J., *Condensed polyanion electrode*, F. Ltd, Editor 2013.
39. http://www.faradion.co.uk/technology/sodium-ion-technology/.
40. Hueso, K.B., Armand, M., and Rojo, T., *High temperature sodium batteries: status, challenges and future trends.* Energy & Environmental Science, 2013. **6**: 734-749.
41. Zhu, X., Zhao, R., Deng, W., Ai, X., Yang, H., and Cao, Y., *An All-solid-state and All-organic Sodium-ion Battery based on Redox-active Polymers and Plastic Crystal Electrolyte.* Electrochimica Acta, 2015. **178**: 55-59.
42. Tanibata, N., Matsuyama, T., Hayashi, A., and Tatsumisago, M., *All-solid-state sodium batteries using amorphous* TiS_3 *electrode with high capacity.* Journal of Power Sources, 2015. **275**: 284-287.
43. Ni'mah, Y.L., Cheng, M.-Y., Cheng, J.H., Rick, J., and Hwang, B.-J., *Solid-state polymer nanocomposite electrolyte of* $TiO_2/PEO/NaClO_4$ *for sodium ion batteries.* Journal of Power Sources, 2015. **278**: 375-381.
44. Kim, J.-K., Lim, Y.J., Kim, H., Cho, G.-B., and Kim, Y., *A hybrid solid electrolyte for flexible solid-state sodium batteries.* Energy & Environmental Science, 2015. **8**: 3589-3596.
45. Delmas, C., Fouassier, C., and Hagenmuller, P., *Structural classification and properties of the layered oxides.* Physica B, 1980. **99**(1-4): 81-85.
46. Velikokhatnyi, O.I., Choi, D., and Kumta, P.N., *Effect of boron on the stability of monoclinic* $NaMnO_2$*: Theoretical and experimental studies.* Materials Science and Engineering B, 2006. **128**: 115-124.
47. Duffort, V., Talaie, E., Black, R., and Nazar, L.F., *Uptake of* CO_2 *in Layered P2-*$Na_{0.6}Mn_{0.5}Fe_{0.5}O_2$*: Insertion of Carbonate Anions.* Chemistry of Materials 2015. **27**(7): 2515-2524.
48. Clément, R.J., Bruce, P.G., and Grey, C.P., *Reveiw-Maganese-Based P2-Type Transition Metal Oxides as Sodium-Ion Battery Cathode Materials.* Journal of the Electrochemical Society, 2015. **162**(14): A2589-A2604.
49. Xu, J., Lee, D.H., Clément, R.J., Yu, X., Leskes, M., Pell, A.J., Pintacuda, G., Yang, X.-Q., Grey, C.P., and Meng, Y.S., *Identifying the Critical Role of Li Substitution in P2–*$Na_x[Li_yNi_zMn_{1-y-z}]O_2(0 < x, y, z < 1)$ *Intercalation Cathode Materials for High-Energy Na-Ion Batteries.* Chemistry of Materials, 2014. **26**(2): 1260-1269.

50. Yabuuchi, N., Hara, R., Kajiyama, M., Kubota, K., Ishigaki, T., Hoshikawa, A., and Komaba, S., *New O2/P2-type Li-Excess Layered Manganese Oxides as Promising Multi-Functional Electrode Materials for Rechargeable Li/Na Batteries.* Advanced Energy Materials, 2014. **4**(13): 1301453.
51. Billaud, J., Singh, G., Armstrong, A.R., Gonzalo, E., Roddatis, V., Armand, M., Rojo, T., and Bruce, P.G., *$Na_{0.67}Mn_{1-x}Mg_xO_2$ $(0 \le x \le 0.2)$: a high capacity cathode for sodium-ion batteries.* Energy & Environmental Science, 2014. **7**(4): 1387-1391.
52. Nguyen, D., Gim, J., Mathew, V., Song, J., Kim, S., Ahn, D., and Kim, J., *Plate-Type NaV_3O_8 Cathode by Solid State Reaction for Sodium-Ion Batteries.* ECS Electrochemistry Letters, 2014. **3**(7): A69-A71.
53. Kawakita, J., Miura, T., and Kishi, T., *Effect of crystallinity on lithium insertion behaviour of $Na_{1+x}V_3O_8$.* Solid State Ionics, 1999. **124**(1-2): 29-35.
54. H.He, Jin, G., Wang, H., Huang, X., Chen, Z., Sun, D., and Tang, Y., *Annealed NaV_3O_8 nanowires with good cycling stability as a novel cathode for Na-ion batteries* Journal of Materials Chemistry A, 2014. **2**: 3563-3570.
55. Schindler, M., Hawthorne, F.C., Alexander, M.A., Kutluoglu, R.A., Mandaliev, P., Halden, N.M., and Mitchell, R.H., *Na-Li-$[V_3O_8]$ insertion electrodes: Structures and diffusion pathways.* Journal of Solid State Chemistry, 2006. **179**: 2616-2628.
56. Liu, J., Chang, D., Whitfield, P., Janssen, Y., Yu, X., Zhou, Y., Bai, J., Ko, J., Nam, K.-W., Wu, L., Zhu, Y., Feygenson, M., Amatucci, G., Ven, A.V.d., Yang, X.-Q., and Khalifah, P., *Ionic Conduction in Cubic $Na_3TiP_3O_9N$, a Secondary Na-Ion Battery Cathode with Extremely Low Volume Change.* Chemistry of Materials, 2014. **26**(10): 3295-3305.
57. Chen, H., Hao, Q., Zivkovic, O., Hautier, G., Du, L.-S., Tang, Y., Hu, Y.-Y., Ma, X., Grey, C.P., and Ceder, G., *Sidorenkite ($Na_3MnPO_4CO_3$): A New Intercalation Cathode Material for Na-Ion Batteries.* Chemistry of Materials, 2013. **25**(14): 2777-2786.
58. Prosini, P.P., Cento, C., Masci, A., and Carewska, M., *Sodium extraction from sodium iron phosphate with a Maricite structure.* Solid State Ionics, 2014. **263**: 1-8.
59. Barpanda, P., Liu, G., Ling, C.D., Tamaru, M., Avdeev, M., Chung, S.-C., Yamada, Y., and Yamada, A., *$Na_2FeP_2O_7$: A Safe Cathode for Rechargeable Sodium-ion Batteries.* Chemistry of Materials, 2013. **25**(17): 3480-3487.
60. Barpanda, P., Ye, T., Avdeev, M., Chung, S.-C., and Yamada, A., *A new polymorph of $Na_2MnP_2O_7$ as a 3.6 V cathode material for sodium-ion batteries.* Journal of Materials Chemistry A, 2013. **1**: 4194-4197.
61. Barpanda, P., Lu, J., Ye, T., Kajiyama, M., Chung, S.-C., Yabuuchi, N., Komaba, S., and Yamada, A., *A layer-structured $Na_2CoP_2O_7$ pyrophosphate cathode for sodium-ion batteries* Royal Society of Chemistry Advances, 2013. **3**: 3857-3860.
62. Song, W., Cao, X., Wu, Z., Chen, J., Huangfu, K., Wang, X., Huang, Y., and Ji, X., *A study into the extracted ion number for NASICON structured $Na_3V_2(PO_4)_3$ in sodium-ion batteries.* Phys. Chem. Chem. Phys., 2014. **16**: 17681-17687.
63. Song, W., Ji, X., Wu, Z., Zhu, Y., Yang, Y., Chen, J., Jing, M., Li, F., and Banks, C.E., *First exploration of Na-ion migration pathways in the NASICON strucutre $Na_3V_2(PO_4)_3$.* Journal of Materials Chemistry A, 2014. **2**(5358-5362).
64. Li, Z., Ravnsbæk, D.B., Xiang, K., and Chiang, Y.-M., *$Na_3Ti_2(PO_4)_3$ as a sodium-bearing anode for rechargeable aqueous sodium-ion batteries.* Electrochemistry Communications, 2014. **44**: 12-15.
65. Jian, Z., Zhao, L., Pan, H., Hu, Y.-S., Li, J., Chen, W., and Chen, L., *Carbon coated $Na_3V_2(PO_4)_3$ as novel electrode material for sodium ion batteries.* Electrochemistry Communications, 2012. **14**: 86-89.
66. Shakoor, R.A., Seo, D.-H., Kim, H., Park, Y.-U., Kim, J., Kim, S.-W., Gwon, H., Lee, S., and Kang, K., *A combined first principles and experimental study on $Na_3V_2(PO_4)_2F_3$ for rechargeable Na batteries.* Journal of Materials Chemistry, 2012. **22**: 20535-20541.
67. Ellis, B.L., Makahnouk, W.R.M., Makimura, Y., Toghill, K., and Nazar, L.F., *A multifunctional 3.5 V iron-based phosphate cathode for rechargeable batteries.* Nature Materials, 2007. **6**: 749-753.
68. Barpanda, P., Oyama, G., Nishimura, S.-i., Chung, S.-C., and Yamada, A., *A 3.8-V earth-abundant sodium battery electrode.* Nature Communications, 2014. **5**: 4358.
69. Yabuuchi, N., Kubota, K., Dahbi, M., and Komaba, S., *Research Development on Sodium-Ion Batteries.* Chemical Reviews, 2014. **114**: 11636-11682.
70. Komaba, S., Murata, W., Ishikawa, T., Yabuuchi, N., Ozeki, T., Nakayama, T., Ogata, A., Gotoh, K., and Fujiwara, K., *Electrochemical Na Insertion and Solid Electrolyte Interphase for Hard-Carbon Electrodes and Application to Na-Ion Batteries.* Advanced Functional Materials, 2011. **21**(20): 3859-3867.

71. Park, S.I., Gocheva, I., Okada, S., and Yamakib, J.I., *Electrochemical Properties of $NaTi_2(PO_4)_3$ Anode for Rechargeable Aqueous Sodium-Ion Batteries* Journal of the Electrochemical Society, 2011. **158**(10): A1067-A1070.
72. Wang, Y., Yu, X., Xu, S., Bai, J., Xiao, R., Hu, Y.S., Li, H., Yang, X.Q., Chen, L., and Huang, X., *A zero-strain layered metal oxide as the negative electrode for long-life sodium-ion batteries.* Nature Communications, 2013. **4**: 2365.
73. Darwiche, A., Marino, C., Sougrati, M.T., Fraisse, B., Stievano, L., and Monconduit, L., *Better Cycling Performances of Bulk Sb in Na-Ion Batteries Compared to Li-Ion Systems: An Unexpected Electrochemical Mechanism.* Journal of the American Chemical Society, 2012. **134**(51): 20805-20811.
74. Qian, J., Wu, X., Cao, Y., Ai, X., and Yang, H., *High Capacity and Rate Capability of Amorphous Phosphorus for Sodium Ion Batteries.* Angewandte Chemie International Edition, 2013. **52**: 4633-4636.
75. Baggetto, L., Allcorn, E., Unocic, R.R., Manthiram, A., and Veith, G.M., *Mo_3Sb_7 as a very fast anode material for lithium-ion and sodium-ion batteries.* Journal of Materials Chemistry A, 2013. **1**: 11163-11169.
76. Baggetto, L., Allcorn, E., Manthiram, A., and Veith, G.M., *Cu_2Sb thin films as anode for Na Batteries.* Electrochemistry Communications, 2013. **27**: 168-171.
77. Hayashi, A., Noi, K., Sakuda, A., and Tatsumisago, M., *Superionic glass-ceramic electrolytes for room-temperature rechargeable sodium batteries.* Nature Communications, 2012. **3**: 1-5.
78. Ponrouch, A., Marchante, E., Courty, M., Tarascon, J.M., and Palacín, M.R., *In search of an optimized electrolyte for Na-ion batteries.* Energy & Environmental Science, 2012. **5**: 8572-8583.
79. Hooper, A., *A study of the electrical properties of single-crystal and polycrystalline β-alumina using complex plane analysis.* Journal of Physics D: Applied Physics, 1977. **10**: 1487-1496.
80. Coors, W.G., Gordon, J.H., and Menzer, S.G., *Electrochemical cell comprising ionically conductive membrane and porous multiphase electrode*, in *US Patent No. 2010/0297537 A1*2010.
81. Bohnke, O., Ronchetti, S., and Mazza, D., *Conductivity measurements on nasicon and nasicon-modified materials.* Solid State Ionics, 1999. **122**: 127-136.
82. Briant, J.L. and Farrington, G.C., *Ionic conductivity in Na^+, K^+, and Ag^+ β"-alumina.* Journal of Solid State Chemistry, 1980 **33**: 385-390.
83. Fergus, J.W., *Ion transport in sodium ion conducting solid electrolytes.* Solid State Ionics, 2012. **227**: 102-112.
84. Lu, X., Xia, G., Lemmon, J.P., and Yang, Z., *Advanced materials for sodium-beta alumina batteries: Status, challenges and perspectives.* Journal of Power Sources, 2010. **195**: 2431-2442.
85. Lu, X., Lemmon, J.P., Sprenkle, V., and Yang, Z., *Sodium-beta alumina batteries: Status and challenges.* The Journal of The Minerals, Metals & Materials Society, 2010. **62**(9): 31-36.
86. Heavens, S.N., *Strength improvement in beta" alumina by incorporation of zirconia.* Journal of Materials Science, 1988. **23**(10): 3515-3518.
87. Hong, H.Y.P., Goodenough, J.B., and Kafalas, J.A., *Fast Na^+ ion transport in skeleton structures.* Materials Research Bulletin, 1976. **11**: 203-220.
88. Catti, M., Stramare, S., and Ibberson, R., *Lithium location in NASICON-type Li conductors by neutron diffraction. I. α' Triclinic -$LiZr_2(PO_4)_3$.* Solid State Ionics, 1999. **123**: 173-180.
89. Iglesias, J.E., Sanz, J., Martinez-Juarez, A., and Rojo, J.M., *Low temperature triclinic distortion in NASICON-type $LiSn_2(PO_4)_3$.* Journal of Solid State Chemistry, 1997. **120**: 322-326.
90. Collin, G., Comes, R., Boilot, J.P., and Colomban, P., *Disorder of tetrahedra in Nasicon-type structure - part I. $Na_3Sc_2(PO_4)_3$: structures and ion-ion correlations.* Journal of Physics and Chemistry of Solids, 1986. **47**: 843-854.
91. Dashjav, E. and Tietz, F., *Neutron diffraction analysis of NASICON-type $Li_{1+x}Al_xTi_{2-x}P_3O_{12}$.* Zeitschrift für Anorganische und Allgemeine Chemie, 2014. **640**: 3070-3073.
92. Boilot, J.P., Collin, G., and Colomban, P., *Relation structure-fast ion conduction in the NASICON Solid Solution.* Journal of Solid State Chemistry, 1988. **73**: 160 - 171.
93. Winand, J.M., Rulmont, A., and Tarte, P., *Nouvelles solutions solides $L^{(I)}M^{(IV)2-x}N^{(IV)x}(PO_4)_3$ (L = Li,Na, M,N = Ge,Sn,Ti,Zr,Hf). Synthèse et étude par diffraction X et conductivité Ionique.* Journal of Solid State Chemistry 1991. **93**: 341-349.
94. Carrasco, M.P., Guillem, M.C., and Alamo, J., *Preparation, structural characterization and study of the properties of the system $NaGe_2(PO_4)_3$-$NaTi_2(PO_4)_3$.* Solid State Ionics, 1992. **63/65**: 684-687.

95. Takahashi, T., Kuwabara, K., and Shibata, M., *Conductivites of Na^+ ion conductors based on NASICON* Solid State Ionics, 1980. **1**: 163-175.

96. Subramanian, M.A., Rudolf, P.R., and Clearfield, A., *The preparation, structure and conductivity of scandium-substituted NASICON.* Journal of Solid State Chemistry, 1985. **60**: 172-181.

97. Losilla, E.R., Aranda, M.A.G., Bruque, S., and West, A.R., *Understanding Na mobility in NASICON materials: a Rietveld, 23Na and 31P MAS NMR, and impedance study.* Chemistry of Materials, 1998. **10**: 665-673.

98. Winaud, J.M., Rulmont, A., and Tarte, P., *Ionic conductivity of the $Na_{1+x}M(III)_x(PO_4)_3$ systems (M = Al, Ga, Cr, Fe, Sc, In, Y, Yb).* Journal of Materials Science 1990. **25**: 4008-4013.

99. Boehm, L., Delbecq, C.J., Hutchinson, E., and Susman, S., *Fast ion conduction and phase transitions in various preparations of $Na_3Sc_2P_3O_{12}$.* Solid State Ionics, 1981. **5**: 311-314.

100. Losilla, E.R., Aranda, M.A.G., Bruque, S., and West, A.R., *Sodium mobility in the NASICON Series $Na_{1+x}Zr_{2-x}In_x(PO_4)_3$.* Chemistry of Materials, 2000. **12**: 2134-2142.

101. d'Yvoire, F., Pintard-Screpel, M., Bretey, E., and de la Rochere, M., *Phase transitions and ionic conduction in 3D skeleton phosphates $A_3M_2(PO_4)_3$: A = Li, Na, Ag, K ; M = Cr, Fe.* Solid State Ionics, 1983. **9/10**: 851-858.

102. Delmas, C., Viala, J.C., Olazcuaga, R., Flem, G.L., and Hagenmuller, P., *Ionic conductivity in NASICON-type phases $Na_{1+x}Zr_{2-x}L_x(PO_4)_3$ (L= Cr, In, Yb).* Solid State Ionics, 1981. **34**: 209-214.

103. Miyajima, Y., Miyoshi, T., Tamaki, J., Matsuoka, M., Yamamoto, Y., Masquelier, C., Tabuchi, M., Saito, Y., and Kageyama, H., *Solubility range and ionic conductivity of large trivalent ion doped $Na_{1+x}M_xZr_{2-x}P_3O_{12}$ (M: In, Yb, Er, Y, Dy, Tb, Gd) solid electrolytes.* Solid State Ionics, 1999. **124**: 201-211.

104. Miyajima, Y., Saito, Y., Matsuoka, M., and Yamamoto, Y., *Ionic conductivity of NASICON-type $Na_{1+x}M_xZr_{2-x}P_3O_{12}$ (M: Yb, Er, Dy).* Solid State Ionics, 1996. **84**: 61-64.

105. Nagai, M., Fujitsu, S., and Kanazawa, T., *Conduction paths in the three-dimentional ionic conductor $Na_{1+x}Y_xZr_{2-x}(PO_4)_3$.* Solid State Ionics, 1981. **34**: 233-236.

106. Maldonado-Manso, P., Aranda, M.A.G., Bruque, S., Sanz, J., and Losilla, E.R., *Nominal vs. actual stoichiometries in Al-doped NASICONs: A study of the $Na_{1,4}Al_{0,4}M_{1,6}(PO_4)_3$ (M=Ge, Sn, Ti, Hf, Zr) family.* Solid State Ionics, 2005. **176**(17-18): 1613-1625.

107. Mouahid, F.E., Bettach, M., Zahir, M., Maldonado-Manso, P., Bruque, S., Losilla, E.R., and Aranda, M.A.G., *Crystal chemistry and ion conductivity of the $Na_{1+x}Ti_{2-x}Al_x(PO_4)_3$ (0<=x<=0.9) NASICON series.* Journal of Materials Chemistry, 2000. **10**: 2748-2753.

108. Krok, F., Kony, D., Dygas, J.R., Jakubowski, W., and Bogusz, W., *On some properties of NASICON doped with MgO and CoO.* Solid State Ionics, 1989. **36**: 251-254.

109. Bogusz, W., Krok, F., and Jakubowski, W., *Influence of doping on some physical properties of NASICON.* Solid State Ionics, 1983. **9/10**: 803-808.

110. Wang, W., Zhang, Z., Ou, X., and Zhao, J., *Properties and phase relationship of the $Na_{1+x}Hf_{2-y}Ti_ySi_xP_{3-x}O_{12}$ system.* Solid State Ionics, 1988. **28**: 442-445.

111. Ignaszak, A., Pasierb, P., Gajerski, R., and Komornicki, S., *Synthesis and properties of NASICON-type materials.* Thermochimica Acta, 2005. **426**(1-2): 7-14.

112. Carrasco, M.P., Guillem, M.C., and Alamo, J., *Structural study, thermal expansion and electrical conductivity of the composition $NaSnZr(PO_4)_3$.* Solid State Ionics, 1992. **63/65**: 688-691.

113. Bennouna, L., Arsalane, S., Brochu, R., Lee, M.R., Chassaing, J., and Quarton, M., *Spécifité des ions $Nb^{(IV)}$ et $Mo^{(IV)}$ dans les monophosphates de type NASICON.* Journal of Solid State Chemistry, 1995. **114**: 224-229.

114. Cava, R.J., Vogel, E.M., and Johnson, D.W., *Effect of homovalent framework cation substitutions on the sodium ion conductivity in $Na_3Zr_2Si_2PO_{12}$*, in *Communications of the American Ceramic Society*1982. C-157-C-159.

115. Aono, H. and Sugimoto, A., *Ionic conductivity and sinterability of NASICON-type ceramics: the systems $NaM_2(PO_4)_3$ + yNaO (M=Ge, Ti, Hf and Zr).* Journal of the American Ceramic Society 1996. **79**: 2786-2788.

116. Rodrigo, J.L. and Alamo, J., *Phase transition in $NaSn_2(PO_4)_3$. Thermal Expansion of $NaM(IV)_2(PO_4)_3$; M(IV)=Ti, Sn, Zr.* Materials Research Bulletin, 1991. **26**: 475-480.

117. Winand, J.M., Rulmont, A., and Tarte, P., *Synthèse et étude de nouveaux Arsenates $M(I)_3N(III)_2(AsO_4)_3$ et de solutions solides $M(I)_3N(III)_2(AsO_4)x(PO_4)_{3-x}$ (M = Li, Na; N = Fe, Sc, In, Cr).* Journal of Solid State Chemistry, 1990. **87**: 83-94.

118. West, A.R., *Solid state chemistry and its applications*, ed. J.W. Sons1987.

119. Goodenough, J.B., *Oxide-ion electrolytes.* Annual Review of Materials Research, 2003. **33**: 91-128.

120. Almond, D.P., Duncan, C.K., and West, A.R., *The determination of Hopping Rates and Carrier Concentration in Ionic Conductors by a new Analysis of AC Conductivity.* Solid State Ionics, 1983. **8**: 159-164.
121. Carrasco, M.P., Guillem, M.C., and Alamo, J., *Synthesis and structural study of $NaTi_2(PO_4)_3$-$NaSn_2(PO_4)_3$ solid solutions. I. The effect of composition on lattice parameters.* Materials Research Bulletin, 1992. **27**(603-610).
122. Carrasco, M.P., Guillem, M.C., and Alamo, J., *Preparation and structural study of sodium titanium phosphate-sodium tin phosphate solid solutions. II. Thermal expansion.* Materials Research Bulletin 1993. **28**: 547-556.
123. Ivanov, A., Yu, K., Belokoneva, E.L., Tismenko, E., and N.V.Simonov, *The crystal structure of Na, Ti-orthophosphate $NaTi_2(PO_4)_3$.* Doklady Akademii Nauk SSSR, 1980. **252**: 1122-1125.
124. Rodrigo, J.L. and Alamo, J., *High temperature neutron diffraction study of sodium di-tin tri-phosphate* Materials Research Bulletin, 1992. **27**: 1091-1098.
125. Bennouna, L., Arsalane, S., Brochu, R., Lee, M.-R., Chassaing, J., and Quarton, M., *Specificites des ions Nb(IV) et Mo(IV) dans les monophosphates de type NASICON.* Journal of Solid State Chemistry, 1995. **114**: 224-229.
126. Squattrito, P.J., Rudolf, P.R., Hinson, P.G., Clearfield, A., Volin, K., and Jorgensen, J.D., *Sodium and oxygen disorder in a scandium-substituted NASICON: a time of flight neutron powder diffraction study of $Na_{2,5}Zr_{1,8}Sc_{0,2}Si_{1,3}P_{1,7}O_{12}$.* Solid State Ionics, 1988. **31**: 31-40.
127. Lucazeau, G., Barj, M., Soubeyroux, J.L., Dianoux, A.J., and Delmas, C., *Neutron scattering and diffraction study of $Na_3Cr_2P_3O_{12}$, $NaZr_2P_3O_{12}$ and $Na_3ZrMgP_3O_{12}$.* Solid State Ionics, 1986. **18/19**: 959-963.
128. Masquelier, C., Wurm, C., Carvajal, J.R., Gaubicher, J., and Nazar, L., *A powder neutron diffraction investigation of the two rhombohedral NASICON analogues: gamma-($Na_3Fe_2(PO_4)_3$) and $Li_3Fe_2(PO_4)_3$.* Chemistry of Materials, 2000. **12**: 525-532.
129. Chakir, M., Jazouli, A.E., and Waal, D.d., *Synthesis, crystal structure and spectroscopy properties of $Na_3AZr(PO_4)_3$ (A = Mg, Ni) and $Li_{2.6}Na_{0.4}NiZr(PO_4)_3$ phosphates.* Journal of Solid State Chemistry, 2006. **179**: 1883-1891.
130. Alpen, U.V., Bell, M.F., and Hoefer, H.H., *Compositional dependence of the electrochemical and structural parameters in the NASICON system ($Na_{1+x}Si_xZr_2P_{3-x}O_{12}$).* Solid State Ionics, 1981. **34**: 215-218.
131. Yvanov, D., Currie, J., Bouchard, H., Lecours, A., Andrian, J., Yelon, A., and Poulin, S., *Sputtered silicate-limit NASICON thin films for electrochemical sensors.* Solid State Ionics, 1994. **67**: 295-299.
132. Capponi, J.J., Joubert, J.C., and Shannon, R.D., *Crystal structure and ionic conductivity in $Na_4Zr_2Si_3O_{12}$.* Journal of Solid State Chemistry, 1981. **39**: 219-229.
133. Zhao, D., Xie, Z., Hu, J., Zhang, H., Zhang, W.L., Yang, S.L., and Cheng, W.D., *Structure determination, electronic and optical properties of $NaGe_2P_3O_{12}$ and $Cs_2GeP_4O_{13}$.* Journal of Moleclar Structure, 2009. **922**: 127-134.
134. Søtofte, I. and Fu, D.-C., *Redetermination of the crystal structure of $Na_3Sc_2(PO_4)_3$.* Solid State Ionics, 1988. **26**: 307-310.
135. Song, J., *Chapter 17: All Solid-State Thin Film Batteries*, in *Handbook of Solid State Batteries*2015, World Scientific Publishing Co. Pte. Ltd.
136. Mattox, D.M., *Chapter 10: Atomistic Film Growth and Some Growth-Related Film Properties*, in *Handbook of Physical Vapor Deposition (PVD) Processing* 2010, Norwich, N.Y. : William Andrew ; Oxford : Elsevier Science.
137. Aroyo, M.I., *International Tables for Crystallography*. Vol. Volume A: Space-group Symmetry, Volume A1: Symmetry Relations between Space Groups. 2013, Departamento Fisica de la Materia Condensada, Universidad del Pais Vasco, UPV/EHU, Bilbao, Spain.
138. Aroyo, M.I., Perez-Mato, J.M., Orobengoa, D., Tasci, E., de la Flor, G., and Kirov, A., *Crystallography online: Bilbao Crystallographic Serve.* Bulgarian Chemical Communications, 2011. **43**(2): 183-197.
139. Aroyo, M.I., Perez-Mato, J.M., Capillas, C., Kroumova, E., Ivantchev, S., Madariaga, G., Kirov, A., and Wondratschek, H., *Bilbao Crystallographic Server I: Databases and crystallographic computing programs.* Zeitschrift für Kristallographie, 2006. **221**(1): 15-27.
140. Aroyo, M.I., Kirov, A., Capillas, C., Perez-Mato, J.M., and Wondratschek, H., *Bilbao Crystallographic Server II: Representations of crystallographic point groups and space groups.* Acta Crystallographica, 2006. **A62**: 115-128.
141. Cowley, J.M., *Diffraction physics*1975.
142. Fultz, B. and Howe, J., *Transmission electron microscopy and diffractometry of materials*2008, Berlin: Springer.

143. Altomare, A., Giacovazzo, C., and Moliterni, A., *Chapter 7: Indexing and Space Group Determination*, in *Powder Diffraction : Theory and Practice*2008, Cambridge UK: Royal Society of Chemistry.
144. Petricek, V., Dusek, M., and Palatinus, L., *Crystallographic computing system JANA2006: General features.* Zeitschrift für Kristallographie, 2014. **229**(5): 345-352.
145. Chang, S.-L., *Thin-Film Characterization by Grazing Incidence X-ray Diffraction and Multiple Beam Interference.* Journal of Physics and Chemistry of Solids, 2001. **62**: 1765-1775.
146. Young, R.A., *The Rietveld Method* 1993, International Union of Crystallography Oxford University Press.
147. Dreele, R.B.V., *Chapter 9: Rietveld Refinement*, in *Powder Diffraction: Theroy and Practice*2008, Cambridge UK: Royal Society of Chemistry.
148. Rietveld, H.M., *A profile refinement method for nuclear and magnetic structures.* Journal of Applied Crystallography, 1969. **2**: 65-71.
149. Rietveld, H.M., *Line profiles of neutron powder-diffraction peaks for structure refinement.* Acta Crystallographica, 1967. **22**: 151-152.
150. Young, R.A., Mackie, P.E., and Dreele, R.B.V., *Application of Pattern-Fitting Structure-Refinement Method to X-Ray Powder Diffractometer Patterns.* Journal of Applied Crystallography, 1977. **10**: 262-269S.
151. Pynn, R., *Chapter 2: Neutron Scattering - a Non-destructive Microscope for Seeing Inside Matter*, in *Neutron applications in earth, energy and environmental sciences*2009: Berlin : Springer.
152. Raman, C.V., *A new Radiation.* Indian Journal of Physics, 1928. **2**: 387-398.
153. West, A.R., *Chapter 4: Other techniques: Microscopy, Spectroscopy, Thermal analysis*, in *Basic Solid State Chemistry* E. John Wiley & Sons, Editor 1999.
154. Beran, A. and Libowitzky, E., *Spectroscopic Methods in Mineralogy* 2004, Eötvös University Press Budapest.
155. Damen, T.C., Porto, S.P.S., and Tell, B., *Raman Effect in Zinc Oxide.* Physical Review, 1966. **142**(2): 570-574.
156. Soares, J.A.N.T., *Chapter 2: Introduction to Optical Characterization of Materials*, in *Practical Materials Characterization*, M. Sardela, Editor 2014, New York, Springer.
157. Barsoukov, E. and Macdonald, J.R., *Impedance Spectroscopy Theory, Experiment and Applications* 2nd. edition2005: Wiley-Interscience.
158. Orazem, M.E. and Tribollet, B., *Electrochemical Impedance Spectroscopy*2008: John Wiley & Sons.
159. Ahmed, R. and Reifsnider, K., *Study of Influence of Electrode Geometry on Impedance Spectroscopy.* International Journal of Electrochemical Science, 2011. **6**: 1159-1174.
160. Lasia, A., *Electrochemical Impedance Spectroscopy and its Applications in Modern Aspects of Electrochemistry*. Vol. 32. 1999: New York: Kluwer Academic/Plenum Publishers.
161. Hjalmarsson, P., Søgaard, M., and Mogensen, M., *Electrochemical behaviour of* $(La_{1-x}Sr_x)_sCo_{1-y}Ni_yO_{3-\delta}$ *ασ πορουσ ΣΟΦΧ χατηοδεσ.* Solid State Ionics, 2009. **180**: 1395-1405.
162. Lyons, M.E.G., *Electroactive Polymer Electrochemistry. Part 1 Fundamentals* 1994: Springer Science+Business Media New York.
163. Irvine, J.T.S., Sinclair, D.C., and West, A.R., *Electroceramics: Characterization by Impedance Spectroscopy.* Advanced Materials, 1990. **2**(3): 132-138.
164. Bocarsly, A.B., *Chapter Electrochemical Techniques - Cyclic Voltammetry* in *Characterization of Materials* E. John Wiley & Sons, Editor 2002. 837-850.
165. Girault, H.H., *Chapter 10: Cyclic voltammetry*, in *Analytical and physical electrochemistry*2004, Lausanne, Switzerland : EPFL ; New York : Marcel Dekker. 376-409.
166. Smith, A., *A High Precision Study of Li-Ion Batteries*, in *Department of Physic and Atmospheric Science* 2012, PhD thesis, Dalhousie University
167. Reed, S.J.B., *Chapter 4: Scanning electron microscopy* in *Electron Microprobe Analysis and Scanning Electron Microscopy in Geology* 2006: Cambridge University Press.
168. Polenova, T., Gupta, R., and Goldbourt, A., *Magic Angle Spinning NMR Spectroscopy: A Versatile Technique for Structural and Dynamic Analysis of Solid-Phase Systems.* Analytical Chemistry, 2015. **87**: 5458-5469.
169. Alia, A., Ganapathy, S., and Groot, H.J.M.d., *Magic Angle Spinning (MAS) NMR: a new tool to study the spatial and electonic structure of photosynthetic complexes.* Photosynthesis Research, 2009. **102**: 415-425.
170. Heitjans, P. and Indris, S., *Diffusion and ionic conduction in nanocrystalline ceramics.* Journal of Physics: Condensed Matter, 2003. **15**: R1257-R1289.
171. Epp, V. and Wilkening, M., *Chapter 5: Li-ion Dynamics in Solids as seen via Relaxation NMR* in *Handbook of Solid State Batteries* 2015, World Scientific Publishing Co. Pte. Ltd.

172. Laye, P.G., *Chapter 3:Differential Thermal Analysis and Differential Scanning Calorimetry* in *Principles of Thermal Analysis and Calorimetry*, P. Haines, Editor 2002: Cambridge, UK : Royal Society of Chemistry.
173. Maca, K., Pouchy, V., and Boccaccini, R., *Sintering Densification Curve – a Practical Approach for its Construction from Dilatometric Shrinkage Data* Science of Sinering, 2008. **40**: 117-122.
174. Hohenberg, P. and Kohn, W., *Inhomogeneous Electron Gas.* Physical Review, 1964. **136**: B864-B871.
175. Kohn, W. and Sham, L.J., *Self-consistent equations including exchange and correlation effects.* Physical Review, 1965. **140**: A1133-A1138.
176. Sheppard, D., Terrell, R., and Henkelman, G., *Optimization methods for finding minimum energy paths.* The Journal of Chemical Physics, 2008. **128**: 134106-134101-134106-134110.
177. Henkelman, G., Uberuaga, B.P., and Jónsson, H., *A climbing image nudged elastic band method for finding saddle points and minimum energy paths.* Journal of Chemistry and Physics, 2000. **113**: 99001-99904.
178. Kresse, G. and Hafner, J., *Ab initio molecular dynamics for liquid metals.* Physical Review, 1993. **B47**: 558-561.
179. Kresse, G. and Furthmüller, J., *Efficiency of ab-initio total energy calculations for metals and semiconductors using a plane-wave basis set.* Computational Materials Science, 1996. **6**(1): 15-50.
180. Kresse, G. and Furthmüller, J., *Efficient iterative schemes for ab initio total-energy calculations using a plane-wave basis set.* Physical Review, 1996. **B54**: 11169-11186.
181. Blöchl, P.E., *Projector augmented-wave method.* Physical Review, 1994. **B50**: 17953-17979.
182. Kresse, G. and Joubert, D., *From ultrasoft pseudopotentials to the projector augmented-wave method.* Physical Review, 1999. **B59**: 1758-1775.
183. Bhat, K., Lustfeld, H., and Blügel, S., in preparation, 2016.
184. O'Keeffe, M. and Hyde, B.G., *Crystal Structures I. Patterns and Symmetry*1996: Mineralogical Society of America, Washington, D. C.
185. Guin, M., Tietz, F., and Guillon, O., *New promising NASICON material as solid electrolyte for sodium-ion batteries: Correlation between composition, crystal structure and ionic conductivity of* $Na_{3+x}Sc_2Si_xP_{3-x}O_{12}$. Solid State Ionics, 2016: submitted.
186. Collin, G., Comes, R., Boilot, J.P., and Colomban, P., *Disorder of Tetrahedra in Nasicon-Type Structure-I.* $Na_3Sc_2(PO_4)_3$*; Structure and ion-ion Correlations.* Journal of Physics and Chemistry of Solids, 1986. **47**(9): 843-854.
187. Tarte, P., Rulmont, A., and Merckaert-Ansay, C., *Vibrational spectrum of nasicon-like, rhombohedral orthophosphates* $M^IM^{IV2}(PO_4)_3$. Spectrochimica Acta, 1986. **42A**(9): 1009-1016.
188. Polles, G.L., Videau, J.-J., and Olazcuaga, R., *Analyse Structurale par Spectroscopie Raman et Infrarouge de quelques Phosphates de Cuivre de Type NASICON.* Journal of Solid State Chemistry, 1996. **127**: 341-349.
189. Barj, M., Perthuis, H., and Colomban, P., *Relations bewteen sublattice Disorder, Phase Transitions and Conductivity in NASICON.* Solid State Ionics, 1983. **9-10**: 845-850.
190. Tietz, F., Koepke, J., and Urland, W., *Analytical investigations of* β*-*Al_2O_3 *and* β''*-*Al_2O_3 *crystals.* Journal of Crystal Growth, 1992. **118**(3-4): 314-318.
191. Boilot J.P., Colomban, P., Collin, G., and Comes, R., *NASICON analog* $Na_3Sc_2(PO_4)_3$*, thermal behaviour of the α, β and γ types, structure, correlations and transitions.* Solid State Ionics, 1988. **28-30**: 437-441.
192. Boilot, J.-P., Colomban, P., Collin, G., and Comes, R., *Disorder of tetrahedra in NASICON-type structure.* $Na_3Sc_2(PO_4)_3$*: structures and ion-ion correlations.* Journal of Physics and Chemistry of Solids, 1986. **47**: 843-854.
193. Kaus, M., Guin, M., Yavuz, M., Knapp, M., Tietz, F., Guillon, O., Ehrenberg, H., and Indris, S., in preparation, 2016.
194. Pet'kov, V.I., Asabina, E.A., and Shchelokov, I.A., *Thermal Expansion of NASICON Materials.* Inorganic Materials, 2013. **49**(5): 502-506.
195. Woodcock, D.A., Lightfoot, P., and Ritter, C., *Mechanism of low thermal expansion in the cation-ordered Nasicon structure.* Chemical Communications, 1998. **1**: 107-108.
196. Srikanth, V., Subbarao, E.C., Agrawal, D.K., Huang, C.-Y., and Roy, R., *Thermal Expansion Anisotropy and Acoustic Emission of* $NaZr_2P_3O_{12}$ *Family Ceramics.* Journal of the American Ceramic Society, 1991. **74**(2): 365-368.
197. Yamai, I. and Ota, T., *Grain Size-Microcracking Relation for* $NaZr_2(PO_4)_3$ *Family Ceramics.* Journal of the American Ceramic Society, 1993. **76**(2): 487-491.

198. Shiratori, Y., Tietz, F., Buchkremer, H.P., and Stöver, D., *YSZ-MgO composite electrolyte with adjusted thermal expansion coefficient to other SOFC components.* Solid State Ionics, 2003. **164**: 27-33.

199. Biswas, M., Kumbhar, C.S., and Gowtam, D.S., *Characterisation of Nanocrystalline Yttria-Stabilized Zirconia: An In Situ HTXRD Study.* ISRN Nanotechnology, 2011. **2011**: 1-4.

200. Yousef, S.G., *Mikrorissbildung durch anisotrope thermische Ausdehnung: Experiment und numerische Simulation*, in *Material- und Geowissenschaften*2004, PhD thesis, Technischen Universität Darmstadt.

201. Laws, N. and Lee, J.C., *Microcracking in Polycrystalline Ceramics: Elastic Isotropy and Thermal Anisotropy.* Journal of the Mechanics and Physics of Solids, 1989. **37**(5): 603-518.

202. Deng, Z., Wang, Z., Chu, I.H., Luo, J., and ong, S.P., *Elastic Properties of Alkali Superionic Conductor Electrolytes from First Principles Calculations.* Journal of the Electrochemical Society, 2016. **163**(2): A67-A74.

203. Kjølseth, C., Fjeld, H., Prytz, Ø., Dahl, P.I., Estournès, C., Haugsrud, R., and Norby, T., *Space-charge theory applied to the grain boundary impedance of proton conducting* $BaZr_{0.9}Y_{0.1}O_{3-\delta}$*.* Solid State Ionics, 2010. **181**: 268-275.

204. Guin, M., Indris, S., Kaus, M., Ehrenberg, H., Tietz, F., and Guillon, O., *Revision of the stability of NASICON type materials.* Solid State Ionics, 2016: in preparation.

205. Fuentes, R.O., Figueiredo, F., Marques, F.M.B., and Franco, J.I., *Reaction of NASICON with water.* Solid State Ionics, 2001. **139**: 309-314.

206. Yoon, Y., Kim, J., Park, C., and Shin, D., *The Relationship of Structural and Electrochemical Properties of NASICON Structure* $Li_{1.3}Al_{0.3}Ti_{1.7}(PO_4)_3$ *Electrolytes by a sol-gel Method.* Journal of Ceramic Processing Research, 2013. **14**: 563-566.

207. Kotobuki, M. and Koishi, M., *Preparation of* $Li_{1.5}Al_{0.5}Ti_{1.5}(PO_4)_3$ *Solid Electrolyte via a sol–gel route using various Al sources.* Ceramics International, 2012. **39**: 4645-4649.

208. Kawai, H. and Kuwano, J., Journal of Electrochemical Society, 1994. **141**: L78-L79.

209. Jian, Z., Zhao, L., Pan, H., Hu, Y.S., Li, H., Chen, W., and Chen, L., *Carbon coated* $Na_3V_2(PO_4)_3$ *as novel electrode material for sodium ion batteries.* Electrochemistry Communications, 2012. **14**(1): 86-89.

210. Uebou, Y., Kiyabu, T., Okada, S., and Yamaki, J.I., *Electrochemical Sodium Insertion into the 3D-Framework of* $Na_3M_2(PO_4)_3$ *(M = Fe,V).* The reports of Institute of Advanced Material Study Kyushu University, 2002. **16**: 1-5.

211. Pavlov, D. and Ignatova, S., *'Breathing' of the lead-acid battery negative plate during cycling.* Journal of applied Electrochemistry, 1987. **17**: 715-723.

212. Zhou, Y.-N., Ma, J., Hu, E., Yu, X., Gu, L., Nam, K.-W., L.Chen, Z.Wang, and ang, X.Q., *Tuning charge–discharge induced unit cell breathing in layer-structured cathode materials for lithium-ion batteries.* Nature Communications, 2014. **2014**: 1-8.

213. Jian, Z., Yuan, C., Han, W., Lu, X., Gu, L., Xi, X., Hu, Y.S., Li, H., Chen, W., Chen, D., Ikuhara, Y., and Chen, L., *Atomic Structure and Kinetics of NASICON* $Na_3V_2(PO_4)_3$*Cathode for Sodium-Ion Batteries.* Advanced Functional Materials, 2014: 1-8.

214. Bordia, R.K. and Scherer, G.W., *On constrained Sintering.* Acta metallurgica, 1988. **36**(9): 2393-2416.

215. Browning, K.L. and Veith, G.M., in preparation, 2016.

216. X.Lu, Li, G., Kim, J.Y., Mei, D., Lemmon, J.P., Sprenkle, V.L., and Liu, J., *Liquid-metal electrode to enable ultra-low temperature sodium–beta alumina batteries for renewable energy storage.* Nature Communications, 2014. **2014**: 1-8.

217. Kang, H., Liu, Y., Shang, M., Lu, T., Wang, Y., and Jiao, L., NaV_3O_8 *nanosheet@polypyrrole core-shell composaites with good electrochemical performance as cathodes for Na-ion batteries.* Nanoscale, 2015. **7**: 9261-9267.

218. He, H., Jin, G., Wang, H., Huang, X., Chen, Z., Sun, D., and Tang, Y., *Annealed* NaV_3O_8 *nanowires with good cycling stability as a novel cathode for Na-ion batteries.* Journal of Materials Chemistry A, 2014. **2**: 3563-3570.

219. Kawakita, J., Majima, M., Miura, T., and Kishi, T., *Preparation and Lithium Insertion Behaviour of Oxygen-deficient* $Li_{1+x}V_3O_{8-}\delta$*.* Journal of Power Sources, 1997. **66**: 135-139.

220. Ma, Q.L., Guin, M., Naqash, S., Tsai, C.-L., Tietz, F., and Guillon, O., *Pushing to the limits: sodium super-ionic conductivity in scandium-substituted* $Na_3Zr_2(SiO_4)_2(PO_4)$*.* 2016: submitted.

List of figures

List of tables

Annexes

Annex 1: Conductivity at room temperature and 300 ℃, activation energy and pre-exponential factor of compositions with the formula $Na_{1+z}M^{(IV)}_{v}M'^{(IV)}_{2-v}(SiO_4)_z(PO_4)_{3-z}$. The values with an asterix were calculated using the Arrhenius law (Equation 9).

NASICON material	**σ_{RT} [S/cm]**	**$\sigma_{300℃}$ [S/cm]**	**E_a [eV]**	**A [S K/cm]**	**Ref.**
$NaZr_2(PO_4)_3$	4.50 x 10^{-6}	4.89 x 10^{-5} *	0.47	1.18 x 10^{5} *	[10, 93, 116]
$NaGe_2(PO_4)_3$	1.10 x 10^{-12} *	2.56 x 10^{-6} *	0.81	1.61 x 10^{4} *	[115]
$NaTi_2(PO_4)_3$	4.43 x 10^{-10} *	2.98 x 10^{-5} *	0.62	3.99 x 10^{3} *	[114-116]
$NaHf_2(PO_4)_3$	8.77 x 10^{-10} *	1.03 x 10^{-4} *	0.65	2.54 x 10^{4} *	[22, 114, 115]
$NaSn_2(PO_4)_3$	1.66 x 10^{-11} *	3.98 x 10^{-7} *	0.575	2.59 x 101 *	[93, 112]
$NaGe_{0.5}Ti_{1.5}(PO_4)_3$	5.93 x 10^{-13} *	9.14 x 10^{-7} *	0.798	5.43 x 10^{3} *	[93, 94]
$NaGeTi(PO_4)_3$	8.53 x 10^{-12} *	2.11 x 10^{-6} *	0.7	1.72 x 10^{3} *	[93, 94]
$NaGe_{1.5}Ti_{0.5}(PO_4)_3$	3.14 x 10^{-11} *	9.35 x 10^{-6} *	0.71	9.36 x 10^{3} *	[93, 94]
$NaSn_{0.5}Ti_{1.5}(PO_4)_3$	1.77 x 10^{-11} *	1.35 x 10^{-6} *	0.637	3.09 x 10^{2} *	[93, 122]
$NaSnTi(PO_4)_3$	6.88 x 10^{-11} *	3.82 x 10^{-6} *	0.62	6.18 x 10^{2} *	[93, 122]
$NaSn_{1.5}Ti_{0.5}(PO_4)_3$	5.15 x 10^{-10} *	6.42 x 10^{-6} *	0.54	2.06 x 10^{2} *	[93, 122]
$NaSn_{0.5}Zr_{1.5}(PO_4)_3$	4.24 x 10^{-11} *	2.84 x 10^{-6} *	0.63	5.62 x 10^{2} *	[93, 112]
$NaSnZr(PO_4)_3$	2.47 x 10^{-10} *	1.66 x 10^{-5} *	0.63	3.28 x 10^{3} *	[93, 112]
$NaSn_{1.5}Zr_{0.5}(PO_4)_3$	7.93 x 10^{-10} *	2.51 x 10^{-5} *	0.59	2.22 x 10^{3} *	[93, 112]
$NaNbZr(PO_4)_3$	2.49 x 10^{-8} *	3.10 x 10^{-4}	0.54	9.97 x 10^{3} *	[113]
$NaNbTi(PO_4)_3$	1.59 x 10^{-6} *	1.00 x 10^{-3}	0.38	1.26 x 10^{3} *	[113]
$NaMoZr(PO_4)_3$	2.06 x 10^{-9} *	3.10 x 10^{-5}	0.55	1.22 x 10^{3} *	[113]
$NaMoTi(PO_4)_3$	3.07 x 10^{-7} *	2.80 x 10^{-4}	0.4	5.28 x 10^{2} *	[113]
$Na_3Zr_2(SiO_4)_2(PO_4)$	6.70 x 10^{-4}	2.00 x 10^{-1}	0.33 (LT) / 0.27 (HT)	7.56 x 10^{4} (LT) / 2.71 x 10^{4} (HT) *	[10, 87, 111]
$Na_4Zr_2(SiO_4)_3$	8.87 x 10^{-9}	1.10 x 10^{-3}	0.38	6.98 x 10^{0} *	[130, 131]
$Na_{2.4}Hf_2(SiO_4)_{1.4}(PO_4)_{1.6}$	7.30 x 10^{-4}	3.99 x 10^{-1} *	0.4 (LT) / 0.28 (HT)	1.26 x 10^{6} (LT) / 6.62 x 10^{4} (HT) *	[22]

$Na_{2.5}Hf_2(SiO_4)_{1.5}(PO_4)_{1.5}$	1.87×10^{-4}	1.34×10^{-2}	0.27	2.04×10^{3} *	[22]
$Na_{2.6}Hf_2(SiO_4)_{1.6}(PO_4)_{1.4}$	5.90×10^{-4}	1.44×10^{-1} *	0.35 (LT) / 0.26 (HT)	1.45×10^{5} (LT) / 1.60×10^{4} (HT) *	[22]
$Na_{2.8}Hf_2(SiO_4)_{1.8}(PO_4)_{1.2}$	6.90×10^{-4}	4.06×10^{-1} *	0.42 (LT) / 0.23 (HT)	2.59×10^{6} (LT) / 2.45×10^{4} (HT) *	[22]
$Na_3Hf_2(SiO_4)_2(PO_4)$	1.10×10^{-3}	2.17×10^{-1} *	0.35 (LT) / 0.21 (HT)	2.70×10^{5} (LT) / 8.73×10^{3} (HT) *	[22]
$Na_{3.2}Hf_2(SiO_4)_{2.2}(PO_4)_{0.8}$	2.30×10^{-3}	4.81×10^{-1} *	0.36 (LT) / 0.19 (HT)	8.34×10^{5} (LT) / 1.29×10^{4} (HT) *	[22]
$Na_{3.4}Hf_2(SiO_4)_{2.4}(PO_4)_{0.6}$	1.40×10^{-3}	2.88×10^{-1} *	0.35 (LT) / 0.22 (HT)	3.44×10^{5} (LT) / 1.42×10^{4} (HT) *	[22]
$Na_{3.6}Hf_2(SiO_4)_{2.6}(PO_4)_{0.4}$	1.20×10^{-3}	2.88×10^{-1} *	0.34 (LT) / 0.29 (HT)	2.00×10^{5} (LT) / 5.86×10^{4} (HT) *	[22]
$Na_{3.8}Hf_2(SiO_4)_{2.8}(PO_4)_{0.2}$	3.20×10^{-4}	8.15×10^{-2} *	0.35 (LT) / 0.27 (HT)	7.87×10^{4} (LT) / 1.11×10^{4} (HT) *	[22]
$Na_{3.5}Hf_{0.2}Ti_{1.8}(SiO_4)_{1.5}(PO_4)_{1.5}$	3.36×10^{-4}	3.52×10^{-2}	0.245	1.39×10^{3} *	[110]
$Na_{3.5}Hf_{0.6}Ti_{1.4}(SiO_4)_{1.5}(PO_4)_{1.5}$	2.81×10^{-4}	3.61×10^{-2}	0.27	3.07×10^{3} *	[110]
$Na_{3.5}HfTi(SiO_4)_{1.5}(PO_4)_{1.5}$	1.35×10^{-4}	3.47×10^{-2}	0.26	9.99×10^{2} *	[110]
$Na_{3.5}Hf_{1.4}Ti_{0.6}(SiO_4)_{1.5}(PO_4)_{1.5}$	8.70×10^{-5}	1.19×10^{-2}	0.5	7.34×10^{6} *	[110]
$Na_3Hf_{0.2}Ti_{1.8}(SiO_4)_2(PO_4)$	2.32×10^{-4}	1.33×10^{-2}	0.3	8.15×10^{3} *	[110]
$Na_3Hf_{0.4}Ti_{1.6}(SiO_4)_2(PO_4)$	9.60×10^{-5}	8.40×10^{-3}	0.31	4.97×10^{3} *	[110]
$Na_3Hf_{0.6}Ti_{1.4}(SiO_4)_2(PO_4)$	2.84×10^{-4}	1.48×10^{-2}	0.29	6.76×10^{3} *	[110]
$Na_3Hf_{0.8}Ti_{1.2}(SiO_4)_2(PO_4)$	1.78×10^{-4}	7.00×10^{-3}	0.31	9.22×10^{3} *	[110]
$Na_3HfTi(SiO_4)_2(PO_4)$	1.31×10^{-4}	6.50×10^{-3}	0.28	2.11×10^{3} *	[110]
$Na_3Ti_{0.1}Zr_{1.9}(SiO_4)_2(PO_4)$	2.37×10^{-4} *	6.90×10^{-2}	0.38 (LT) / 0.2 (HT)	1.88×10^{5} (LT) / 2.27×10^{3} (HT) *	[95]
$Na_3Ti_{0.2}Zr_{1.8}(SiO_4)_2(PO_4)$	1.89×10^{-4} *	5.50×10^{-2}	0.38 (LT) / 0.2 (HT)	1.49×10^{5} (LT) / 1.81×10^{3} (HT) *	[95]
$Na_3Ti_{0.3}Zr_{1.7}(SiO_4)_2(PO_4)$	2.13×10^{-4} *	6.20×10^{-2}	0.38 (LT) / 0.2 (HT)	1.68×10^{5} (LT) / 2.04×10^{3} (HT) *	[95]

Annex 2: Conductivity at room temperature and 300 ℃, activa tion energy and pre-exponential factor of compositions with the formula $Na_{1+2w+z}M^{(II)}_{w}M'^{(IV)}_{2-w}(SiO_4)_z(PO_4)_{3-z}$. The values with an asterix were calculated using the Arrhenius law (Equation 9).

NASICON material	**σ_{RT} [S/cm]**	**$\sigma_{300℃}$ [S/cm]**	**E_a [eV]**	**A [S K/cm]**	**Ref.**
$Na_{3.08}Mg_{0.04}Zr_{1.96}(SiO_4)_2(PO_4)$	7.66 x 10^{-4} *	1.60 x 10^{-1}	0.36 (LT) 0.19(HT)	2.78 x 10^{5} (LT) 4.30 x 10^{3} (HT) *	[95]
$Na_{3.2}Mg_{0.1}Zr_{1.9}(SiO_4)_2(PO_4)$	3.48 x 10^{-4} *	6.20 x 10^{-2}	0.34 (LT) 0.22(HT)	5.80 x 10^{4} (LT) 3.06 x 10^{3} (HT) *	[95]
$Na_{3.6}Mg_{0.3}Zr_{1.7}(SiO_4)_2(PO_4)$	1.44 x 10^{-4} *	3.90 x 10^{-2}	0.36 (LT) 0.25(HT)	5.24 x 10^{4} (LT) 3.53 x 10^{3} (HT) *	[95]
$Na_{3.08}Zn_{0.04}Zr_{1.96}(SiO_4)_2(PO_4)$	3.66 x 10^{-5} *	3.50 x 10^{-2}	0.43 (LT) 0.31(HT)	2.02 x 10^{5} (LT) 1.07 x 10^{4} (HT) *	[95]
$Na_{3.2}Zn_{0.1}Zr_{1.9}(SiO_4)_2(PO_4)$	1.09 x 10^{-4} *	4.40 x 10^{-2}	0.37 (LT) 0.31(HT)	5.84 x 10^{4} (LT) 1.34 x 10^{4} (HT) *	[95]
$Na_{3.4}Zn_{0.2}Zr_{1.4}(SiO_4)_2(PO_4)$	9.19 x 10^{-4} *	4.90 x 10^{-2}	0.28(LT) 0.14(HT)	1.48^{x} 10^{4} (LT) 4.78 x 10^{2} (HT) *	[95]
$Na_{3.6}Zn_{0.3}Zr_{1.7}(SiO_4)_2(PO_4)$	2.93 x 10^{-5} *	2.80 x 10^{-2}	0.43 (LT) 0.31(HT)	1.62 x 10^{5} (LT) 8.54 x 10^{3} (HT) *	[95]
$Na_{3.28}Mg_{0.04}Zr_{1.96}(SiO_4)_{2.2}(PO_4)_{0.8}$	1.53 x 10^{-3} *	2.40 x 10^{-1}	0.34 (LT) 0.19(HT)	2.55 x 10^{5} (LT) 6.44 x 10^{3} (HT) *	[108]
$Na_{3.36}Mg_{0.08}Zr_{1.92}(SiO_4)_{2.2}(PO_4)_{0.8}$	8.09 x 10^{-4} *	9.50 x 10^{-2}	0.32 (LT) 0.19(HT)	6.19 x 10^{4} (LT) 2.55 x 10^{3} (HT) *	[108]
$Na_{3.52}Mg_{0.16}Zr_{1.84}(SiO_4)_{2.2}(PO_4)_{0.8}$	2.62 x 10^{-4} *	2.00 x 10^{-2}	0.29 (LT) 0.19(HT)	6.24 x 10^{3} (LT) 5.37 x 10^{2} (HT) *	[108]
$Na_{3.36}Zn_{0.08}Zr_{1.92}(SiO_4)_{2.2}(PO_4)_{0.8}$	1.95 x 10^{-3} *	2.10 x 10^{-1}	0.32 (LT) 0.17(HT)	1.49 x 10^{5} (LT) 3.76 x 10^{3} (HT) *	[109]
$Na_{3.36}Cu_{0.08}Zr_{1.92}(SiO_4)_{2.2}(PO_4)_{0.8}$	1.09 x 10^{-3} *	2.09 x 10^{-1}	0.36 (LT) 0.17(HT)	3.95 x 10^{5} (LT) 3.74 x 10^{3} (HT) *	[109]
$Na_{3.36}Co_{0.08}Zr_{1.92}(SiO_4)_{2.2}(PO_4)_{0.8}$	1.85 x 10^{-3} *	2.40 x 10^{-1}	0.33 (LT) 0.18(HT)	2.08 x 10^{5} (LT) 5.26 x 10^{3} (HT) *	[109]
$Na_{3.232}Co_{0.016}Zr_{1.984}(SiO_4)_{2.2}(PO_4)_{0.8}$	2.36 x 10^{-3} *	2.40 x 10^{-1}	0.31 (LT) 0.19(HT)	1.22 x 10^{5} (LT) 6.44 x 10^{3} (HT) *	[108]
$Na_{3.52}Co_{0.16}Zr_{1.84}(SiO_4)_{2.2}(PO_4)_{0.8}$	8.65 x 10^{-4} *	1.00 x 10^{-1}	0.31 (LT) 0.22(HT)	4.48 x 10^{4} (LT) 4.93 x 10^{3} (HT) *	[108]

Annex 3: Conductivity at room temperature and 300 ℃, activation energy and pre-exponential factor of compositions with the formula $Na_{1+x+z}M^{(III)}_{x}M'^{(IV)}_{2-x}(SiO_4)_z(PO_4)_{3-z}$. The values with an asterix were calculated using the Arrhenius law (Equation 9).

NASICON material	σ_{RT} [S/cm]	$\sigma_{300℃}$ [S/cm]	E_a [eV]	A [S K/cm]	Ref.
$Na_{1.2}In_{0.2}Zr_{1.8}(PO_4)_3$	2.08×10^{-7} *	1.02×10^{-3} *	0.49	1.19×10^{4} *	[100]
$Na_{1.4}In_{0.4}Zr_{1.6}(PO_4)_3$	9.76×10^{-7} *	2.27×10^{-3} *	0.45	1.18×10^{4} *	[100]
$Na_{1.5}Al_{0.5}Zr_{1.5}(PO_4)_3$	5.70×10^{-6}	6.70×10^{-4}	0.54	2.28×10^{6} (LT) 2.15×10^{4} (HT) *	[98]
$Na_{1.5}Cr_{0.5}Zr_{1.5}(PO_4)_3$	1.00×10^{-5}	5.50×10^{-4}	0.425	4.55×10^{4} (LT) 1.72×10^{3} (HT) *	[98, 102]
$Na_{1.5}Ga_{0.5}Zr_{1.5}(PO_4)_3$	3.40×10^{-6}	3.40×10^{-4}	0.518	5.78×10^{5} (LT) 6.99×10^{3} (HT) *	[98]
$Na_{1.5}In_{0.5}Zr_{1.5}(PO_4)_3$	2.90×10^{-5}	1.90×10^{-3}	0.477	1.00×10^{6} (LT) 1.70×10^{4} (HT) *	[98, 102, 117]
$Na_{1.5}Sc_{0.5}Zr_{1.5}(PO_4)_3$	5.80×10^{-5}	2.30×10^{-3}	0.425	2.64×10^{5} (LT) 7.20×10^{3} (HT) *	[98]
$Na_{1.5}Y_{0.5}Zr_{1.5}(PO_4)_3$	5.60×10^{-5}	1.40×10^{-3}	0.378	4.09×10^{4} (LT) 1.69×10^{3} (HT) *	[98, 105]
$Na_{1.5}Yb_{0.5}Zr_{1.5}(PO_4)_3$	3.00×10^{-5}	1.20×10^{-3}	0.425	1.37×10^{5} (LT) 3.75×10^{3} (HT) *	[98, 102, 104]
$Na_2AlZr(PO_4)_3$	1.20×10^{-6}	2.30×10^{-4}	0.586	2.88×10^{6} (LT) 1.87×10^{4} (HT) *	[98]
$Na_2CrZr(PO_4)_3$	2.50×10^{-5}	8.50×10^{-4}	0.409	6.11×10^{4} (LT) 1.92×10^{3} (HT) *	[98]
$Na_{2.2}In_{1.2}Zr_{0.8}(PO_4)_3$	2.63×10^{-6} *	3.49×10^{-3} *	0.42	9.86×10^{3} *	[100]
$Na_{2.3}Yb_{1.3}Zr_{0.7}(PO_4)_3$	6.03×10^{-6} *	5.50×10^{-3}	0.4	1.04×10^{4} *	[98, 102]
$Na_{2.5}Cr_{1.5}Zr_{0.5}(PO_4)_3$	1.80×10^{-4}	7.20×10^{-3}	0.425	8.20×10^{5} (LT) 2.25×10^{4} (HT) *	[98]
$Na_{2.5}In_{1.5}Zr_{0.5}(PO_4)_3$	1.00×10^{-4}	6.40×10^{-3}	0.472	2.84×10^{6} (LT) 5.19×10^{4} (HT) *	[98, 100]
$Na_{2.5}Sc_{1.5}Zr_{0.5}(PO_4)_3$	5.60×10^{-4}	1.20×10^{-2}	0.357	1.81×10^{5} (LT) 9.48×10^{3} (HT) *	[98]
$Na_{2.5}Y_{1.5}Zr_{0.5}(PO_4)_3$	4.60×10^{-5}	2.50×10^{-3}	0.456	7.00×10^{5} (LT) 1.47×10^{4} (HT) *	[98, 105]
$Na_{2.5}Yb_{1.5}Zr_{0.5}(PO_4)_3$	1.90×10^{-4}	2.40×10^{-2}	0.544	8.89×10^{7} (LT) 8.35×10^{5} (HT) *	[98, 102, 104]
$Na_{2.5}Er_{1.5}Zr_{0.5}(PO_4)_3$	1.24×10^{-9} *	1.00×10^{-4}	0.64	2.43×10^{4} *	[103, 104]
$Na_{2.5}Dy_{1.5}Zr_{0.5}(PO_4)_3$	1.65×10^{-8} *	6.30×10^{-4}	0.6	6.82×10^{4} *	[103]
$Na_{2.6}In_{1.6}Zr_{0.4}(PO_4)_3$	2.81×10^{-6} *	7.87×10^{-2} *	0.46	5.00×10^{4} *	[100]
$Na_{2.8}In_{1.8}Zr_{0.2}(PO_4)_3$	2.38×10^{-6} *	3.81×10^{-3} *	0.43	1.32×10^{4} *	[100]
$Na_{2.85}In_{1.85}Zr_{0.15}(PO_4)_3$	5.25×10^{-7} *	3.10×10^{-3}	0.5	4.43×10^{4} *	[102]
$Na_{2.95}Cr_{1.95}Zr_{0.05}(PO_4)_3$	4.22×10^{-6} *	9.80×10^{-3}	0.45	5.09×10^{4} *	[102]
$Na_3Cr_2(PO_4)_3$	1.70×10^{-7}	7.00×10^{-3}	0.68 (LT) 0.38 (HT)	1.58×10^{7} (LT) 8.81×10^{3} (HT) *	[98, 101, 102]
$Na_3Fe_2(PO_4)_3$	1.20×10^{-7}	9.00×10^{-3}	0.82 (LT) 0.41 (HT)	2.60×10^{9} (LT) 2.08×10^{4} (HT) *	[98, 101]

$Na_3In_2(PO_4)_3$	1.76×10^{-7} *	9.00×10^{-4}	0.4923	1.10×10^{4} *	[98, 100]
$Na_3Sc_2(PO_4)_3$					[98, 99]
$Na_{1.4}Al_{0.4}Ge_{1.6}(PO_4)_3$	7.28×10^{-10} *	4.89×10^{-5} *	0.63	9.68×10^{3} *	[106, 107]
$Na_{1.4}Al_{0.4}Sn_{1.6}(PO_4)_3$	1.4×10^{-8} *	3.09×10^{-4} *	0.57	1.81×10^{4} *	[106, 107]
$Na_{1.4}Al_{0.4}Ti_{1.6}(PO_4)_3$	5.60×10^{-8}	4.81×10^{-4} *	0.52	1.03×10^{4} *	[106, 107]
$Na_{1.6}Al_{0.6}Ti_{1.4}(PO_4)_3$	1.10×10^{-7}	1.99×10^{-3} *	0.56	9.59×10^{4} *	[106, 107]
$Na_{1.8}Al_{0.8}Ti_{1.2}(PO_4)_3$	1.20×10^{-7}	1.80×10^{-3} *	0.55	7.09×10^{4} *	[106, 107]
$Na_{1.9}Al_{0.9}Ti_{1.1}(PO_4)_3$	1.30×10^{-7}	9.26×10^{-4} *	0.51	1.62×10^{4} *	[106, 107]
$Na_{1.4}In_{0.4}Ti_{1.6}(PO_4)_3$	1.86×10^{-8} *	2.12×10^{-4} *	0.535	6.13×10^{3} *	[97]
$Na_{1.4}In_{0.4}Sn_{1.6}(PO_4)_3$	2.72×10^{-8} *	2.83×10^{-4} *	0.53	7.38×10^{3} *	[97]
$Na_{1.4}In_{0.4}Hf_{1.6}(PO_4)_3$	1.86×10^{-7} *	1.87×10^{-4} *	0.405	3.89×10^{2} *	[97]
$Na_{2.04}Y_{0.04}Zr_{1.96}(SiO4)_2(PO_4)$	3.48×10^{-4} *	6.20×10^{-2}	0.34 (LT) 0.22 (HT)	5.80×10^{4} (LT) 3.06×10^{3} (HT) *	[95]
$Na_{2.1}Y_{0.1}Zr_{1.9}(SiO4)_2(PO_4)$	2.92×10^{-3} *	1.10×10^{-1}	0.25 (LT) 0.16 (HT)	1.46×10^{4} (LT) 1.61×10^{3} (HT) *	[95]
$Na_{2.3}Y_{0.3}Zr_{1.7}(SiO4)_2(PO_4)$	1.06×10^{-4} *	2.00×10^{-2}	0.32 (LT) 0.30 (HT)	8.13×10^{3} (LT) 4.98×10^{3} (HT) *	[95]
$Na_{2.5}Sc_{0.2}Zr_{1.8}(SiO_4)_{1.3}(PO_4)_{1.7}$	3.19×10^{-4} *	4.50×10^{-2}	0.3	1.12×10^{4} *	[96]
$Na_3Sc_{1.5}Zr_{0.5}(SiO_4)_{0.5}(PO_4)_{2.5}$	1.17×10^{-4} *	2.90×10^{-2}	0.33	1.32×10^{4} *	[96]
$Na_3ScZr(SiO_4)_2(PO_4)$	1.82×10^{-4} *	3.10×10^{-2}	0.31	9.43×10^{3} *	[96]
$Na_{3.2}Sc_{0.8}Zr_{1.2}(SiO_4)_{1.2}(PO_4)_{1.8}$	1.42×10^{-4} *	2.90×10^{-2}	0.32	1.09×10^{4} *	[96]
$Na_{3.5}Sc_{0.5}Zr_{1.5}(SiO_4)_{1.5}(PO_4)_{1.5}$	1.41×10^{-4} *	1.07×10^{-1}	0.30 (LT) 0.23 (HT)	3.59×10^{4} (LT) 6.45×10^{3} (HT) *	[96]
$Na_{3.8}Sc_{0.2}Zr_{1.8}(SiO_4)_{1.8}(PO_4)_{1.2}$	1.90×10^{-4} *	1.20×10^{-1}	0.37 (LT) 0.21 (HT)	2.44×10^{5} (LT) 4.83×10^{3} (HT) *	[96]
$Na_{3.3}Sc_{0.3}Zr_{1.7}(SiO_4)_2(PO_4)$	4.14×10^{-4} *	1.79×10^{-1}	0.37 (LT) 0.20 (HT)	3.81×10^{5} (LT) 5.89×10^{3} (HT) *	[96]
$Na_{3.5}Sc_{0.5}Zr_{1.5}(SiO_4)_2(PO_4)$	4.88×10^{-4} *	1.00×10^{-1}	0.32	3.73×10^{4} *	[96]
$Na_{2.7}Sc_{0.2}Zr_{1.8}(SiO_4)_{1.5}(PO_4)_{1.5}$	8.87×10^{-5} *	8.10×10^{-2}	0.4	1.53×10^{5} *	[96]

Annex 4: Conductivity at room temperature and 300 ℃, activa tion energy and pre-exponential factor of compositions with the formula $Na_{1-y+z}M^{(V)}_{y}M'^{(IV)}_{2-y}(SiO_4)_z(PO_4)_{3-z.}$ The values with an asterix were calculated using the Arrhenius law (Equation 9).

NASICON material	**σ_{RT} [S/cm]**	**$\sigma_{300℃}$ [S/cm]**	**E_a [eV]**	**A [S K/cm]**	**Ref.**
$Na_{2.96}Nb_{0.04}Zr_{1.96}(SiO_4)_2(PO_4)$	4.95×10^{-3} *	1.30×10^{-1}	0.21	5.23×10^{3} *	[95]
$Na_{2.9}Nb_{0.1}Zr_{1.9}(SiO_4)_2(PO_4)$	1.87×10^{-3} *	4.90×10^{-2}	0.21	1.97×10^{3} *	[95]
$Na_{2.96}Ta_{0.04}Zr_{1.96}(SiO_4)_2(PO_4)$	2.17×10^{-3} *	1.10×10^{-1}	0.27 (LT) 0.17 (HT)	1.97×10^{3} *	[95]
$Na_{2.9}Ta_{0.1}Zr_{1.9}(SiO_4)_2(PO_4)$	1.22×10^{-3} *	6.20×10^{-2}	0.27 (LT) 0.17 (HT)	1.11×10^{3} *	[95]
$Na_{2.96}V_{0.04}Zr_{1.96}(SiO_4)_2(PO_4)$	5.33×10^{-3} *	1.40×10^{-1}	0.21 (HT)	5.64×10^{3} *	[95]
$Na_{2.9}V_{0.1}Zr_{1.9}(SiO_4)_2(PO_4)$	4.78×10^{-4} *	9.80×10^{-2}	0.32	3.66×10^{4} *	[95]

Acknowledgments

The compilation of this thesis would not have been possible without the help and support of many people that have crossed my way during the last three years.

I firstly want to thank Herr Buchkremer and Robert Vaßen for trusting me in taking over this research project even if I had close to no experience in that field, thank you for giving me the opportunity to start working at IEK-1.

Shortly after starting his new position as the head of this institute, Prof Olivier Guillon agreed to become my supervisor and I am very thankful for his guidance, his constructive feedback and remarks in spite of a very busy schedule.

My biggest acknowledgment goes to Frank Tietz, who I admire for his brilliant scientific mind. He completely trusted me in developing this PhD in the direction I wanted to and didn’t stop helping and advising me along the way. His passion for his work and our research gave me more motivation that I ever knew I had, so thank you Frank for trusting me and guiding me through these three years.

I also want to thank all my colleagues from our group: Michaela Andreas and Jochen Ripphahn, Volker Bader, especially for all the thermal treatments and the reparation of all electronic compounds that I may have broken along the way, Marie-Theres Gerhards and Sylke Pristat for the thermal analysis but also their friendship and support. A special thank I address to Qianli Ma and Enkh Dashjav, with whom I shared an office for half of the PhD time. Ma was always ready to help me and gave me so much valuable advice especially about synthesis of materials. I also really enjoyed the presents I always got every time he went back from a trip to China. Enkh taught me almost everything I know about Rietveld refinement and also helped me refine the neutron diffraction data. During the last three years she became a dear friend and I want to thank her for all the good times spent at her place. I take this opportunity to thank her husband Daniel Grüner, who did not hesitate to stop his schedule to make some SEM pictures for me when time was running out.

I want to thank also Sahir Naqash, with whom I have been sharing an office for a year: thank you for the fun talks about cars, Pakistan, travels and everything including work. The coming year sharing the office with you will be just as fun as the last one, I’m sure.

I worked in close collaboration with colleagues from the battery group at IEK-1: Thorsten Albrecht, Frank Vondalen, Sven Uhlenbruck, Martin Finsterbusch, Sandra Lobe, Chi-Long Tsai, Anna Windmüller, Thorsten Reppert, Georg Teucher and Christian Dellen. I learnt so much from each of them and close friendships have developed from these collaborations. A special thank I give to Christian and Georg; we started our PhD contract on the same day and have been supporting each other ever since, thank you guys for all the great times.

So many other people have contributed to this work, thank you to Mark Kappertz for helping on the preparation of SEM specimen, and Doris Sebold for making the SEM pictures. Thank you to Egbert Wessel for doing EDX and WDX analysis on my single crystals. Thank you also to the colleagues from ZEA-3, and especially Volker Nischwitz for the ICP-OES.

From other research institution I have to thank the colleagues from IAM-ESS, KIT, Maximilian Kaus, Sylvio Indris, Murat Yavuz, Michael Knapp and Helmut Ehrenberg. Their interest in my materials and their NMR and high temperature XRD results added real value to this work.

For the Raman investigation of my samples I want to thank M Giarola, G Mariotto and Günther Redhammer who is still working on the XRD analysis of the single crystals.

My complete gratitude goes to Gabriel Veith who invited me to work in his group at ORNL for two weeks. Thank you to Katie Browling who spent these weeks preparing all our samples with me. It was a great experience to work in another institution, especially abroad. Everybody at ORNL welcomed me

and gave me the impression I belonged to their research group. Not only on a professional level but also personally these 2 weeks have brought me a lot and I am thankful that I could seize this opportunity.

I want to thank my parents and my family, who supported me even though I was quitting a permanent position to make this PhD; they have been there all the way via Skype or visiting.

Thank you to Feh, my flatmate during these 3 years, who coped with me through the ups and downs and was always there whatever my mood was. Thank you so much to make Aachen feel like home so fast.

Finally I want to thank Jean, my fiancé. Thank you for renovating our new flat almost on your own when I was writing the thesis, and also for being so positive all the time, that was the perfect attitude.

Schriften des Forschungszentrums Jülich
Reihe Energie & Umwelt / Energy & Environment

Band / Volume 360
Interface and Topography Optimization for Thin-Film Silicon Solar Cells with Doped Microcrystalline Silicon Oxide Layers
C. Zhang (2017), VII, 156 pp
ISBN: 978-3-95806-209-2

Band / Volume 361
Calibration and large-scale inversion of multi-configuration electromagnetic induction data for vadose zone characterization
C. von Hebel (2017), ix, 123 pp
ISBN: 978-3-95806-210-8

Band / Volume 362
Process-based modelling of regional water and energy fluxes taking into account measured neutron intensities by cosmic-ray probes
R. Baatz (2017), xvi, 135 pp
ISBN: 978-3-95806-211-5

Band / Volume 363
Quantitative Analyse der Lithiumverteilung in Kathoden- und Elektrolyt-Dünnschichten für Festkörperbatterien
C. Dellen (2017), vi, 161 pp
ISBN: 978-3-95806-214-6

Band / Volume 364
Intragruppentrennung Seltener Erden mittels neuer phosphororganischer Liganden
S. Hadić (2017), VIII, 164 pp
ISBN: 978-3-95806-215-3

Band / Volume 365
Automated Magnetic Divertor Design for Optimal Power Exhaust
M. Blommaert (2017), xxiv, 220 pp
ISBN: 978-3-95806-216-0

Band / Volume 366
PEM-Elektrolyse-Systeme zur Anwendung in Power-to-Gas Anlagen
G. Tjarks (2017), IV, 135 pp
ISBN: 978-3-95806-217-7

Band / Volume 367
Fundamental Insights into the Radium Uptake into Barite by Atom Probe Tomography and Electron Microscopy
J. Weber (2017), IX, 160 pp
ISBN: 978-3-95806-220-7

Band / Volume 368
Entwicklung von elektronenleitenden Schutzschichten gegen die anodische Auflösung von Stromsammlern in neuartigen „Dual-Ionen"-Energiespeichern
G. Teucher (2017), VIII, 120 pp
ISBN: 978-3-95806-222-1

Band / Volume 369
Herstellung und Charakterisierung oxiddispersionsverstärkter Haftvermittlerschichten
J. Bergholz (2017), V, 133, II pp
ISBN: 978-3-95806-223-8

Band / Volume 370
Performance of Plasma Facing Materials under Thermal and Plasma Exposure
I. Steudel (2017), XVI, 150 pp
ISBN: 978-3-95806-226-9

Band / Volume 371
The Impact of Transient Thermal Loads on Beryllium as Plasma Facing Material
B. Spilker (2017), XII, 134 pp
ISBN: 978-3-95806-227-6

Band / Volume 372
Analysis and Simulation of Macroscopic Defects in $Cu(In,Ga)Se_2$ Photovoltaic Thin Film Modules
B. Misic (2017), iv, 147 pp
ISBN: 978-3-95806-228-3

Band / Volume 373
Chemical and physical properties of sodium ionic conductors for solid-state batteries
M. Guin (2017), ix, 126 pp
ISBN: 978-3-95806-229-0

Weitere ***Schriften des Verlags im Forschungszentrum Jülich*** unter
http://wwwzb1.fz-juelich.de/verlagextern1/index.asp

Energie & Umwelt /
Energy & Environment
Band / Volume 373
ISBN 978-3-95806-229-0

JÜLICH
FORSCHUNGSZENTRUM

Energie & Umwelt
Energy & Environment

373

Chemical and physical properties of sodium ionic conductors for solid-state batteries

Marie Guin

Mitglied der Helmholtz-Gemeinschaft

JÜLICH
FORSCHUNGSZENTRUM

Chemical and physical properties of sodium ionic conductors for solid-state batteries

Marie Guin

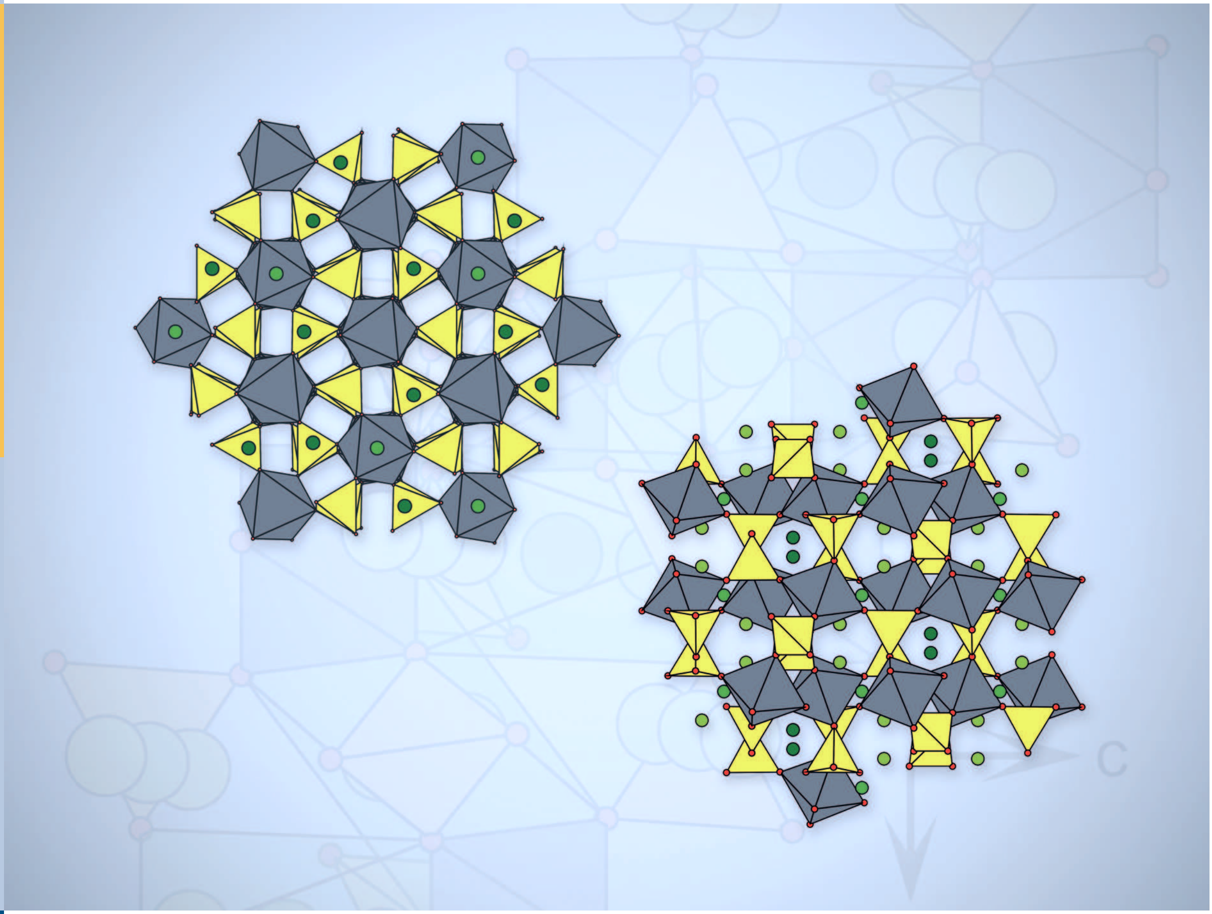

Energie & Umwelt /
Energy & Environment
Band / Volume 373
ISBN 978-3-95806-229-0

JÜLICH
FORSCHUNGSZENTRUM